

Technische Universität München
Fakultät für Physik
Walther-Meißner-Institut für Tieftemperaturforschung

Master's Thesis in Physics

Spin Transport in Magnetic Nanostructures

Tobias Wimmer

Garching, November 2016

Supervisor: Prof. Dr. Sebastian T. B. Goennenwein
Advisor: Kathrin Ganzhorn

First reviewer (Supervisor): Prof. Dr. Sebastian T. B. Goennenwein

Second reviewer: N. N.

Contents

1	Introduction	1
2	Theoretical Concepts	5
2.1	Spin Currents	5
2.2	Spin Hall Magnetoresistance	7
2.3	Spin Seebeck Effect	8
2.4	Non-local Spin Transport	10
3	Experimental Details	13
3.1	Material Systems	13
3.2	Fabrication	15
3.3	Measurement Techniques	16
4	Non-local Spin Transport in YIG Pt Nanostructures	19
4.1	Resistive Contribution	19
4.1.1	Temperature Dependence	21
4.1.2	Magnetic Field Dependence	25
4.1.3	Distance Dependence	34
4.2	Thermal Contribution	42
4.2.1	General Concepts	42
4.2.2	Experimental Results	45
4.3	Summary	60
5	Magnon Logic in a Multiterminal YIG Pt Nanostructure	63
5.1	Characterization of a three Strip Device	63
5.1.1	One Injector, two Detectors	63
5.1.2	Two Injectors, one Detector	65
5.2	Magnon-based Majority Gate	66
6	Non-local Spin Transport in GIG Pt Nanostructures	71
6.1	Resistive Contribution	72
6.1.1	Temperature Dependence	73
6.1.2	Magnetic Field Dependence	76
6.2	Thermal Contribution	82
6.2.1	Temperature Dependence	82
6.2.2	Magnetic Field Dependence	85
6.3	Summary	86
7	Summary and Outlook	89
7.1	Summary	89

7.2 Outlook	91
7.2.1 Influence of Optical Magnons on the MMR Effect	91
7.2.2 Influence of Magnetic Damping/Structure on Magnon Diffusion	92
7.2.3 Phonon Heat Transport in the Non-local Spin Seebeck Effect	93
7.2.4 Non-local Spin Transport in YIG FM Nanostructures	93
A Theoretical Model for the Temperature and Field Dependence of the Magnon Diffusion Length	97
B Crosstalk between Electrically Isolated Pt Strips on YIG	101
Bibliography	108
Acknowledgements	109

Chapter 1

Introduction

"Insanity is doing the same thing over and over again and expecting different results." [1,2]

This quote accurately describes the thrill in physics. If the primevally living homo erectus had always insisted on stones to be the material of choice, mankind wouldn't be where it is today. In other words, it is of great importance to think out of the box trying yet unknown materials and exploring new strategies and fundamental concepts. In physics and material science, a key topic is the development of ever smaller, faster and "better" electronic devices. One interesting concept hereby is to use the spin of the electrons in these devices. The corresponding research field is called spintronics, bringing together the two basic terms electronics and spin. In simple terms, the spin brings along a finite magnetic moment. However, it in fact is a highly complex quantum mechanical property of e.g. electrons, protons etc., representing the essential ingredient of magnetism. Up to now, the spin degree of freedom is commercially mainly used in a static fashion, e.g. in magnetic storage devices [3]. One important goal of spintronics is, however, to drive spin at will, in the form of spin currents. This requires sources [4], detectors [5] as well as manipulation units for spin currents.

In this thesis, we focus more on spin currents carried by magnons, i.e. on the transport of the fundamental magnetic excitations in magnetically ordered materials. These magnons (or spin waves) are analogous to photons, the fundamental excitations of the electromagnetic field, in many ways. In contrast to electric charge currents, magnons can be transported even in insulating materials, given that the material is in a magnetically ordered phase. This allows for information processing in an insulating material without charge currents, potentially reducing (Joule) dissipation [6]. A widely used technique for the generation of spin currents is the direct excitation of magnetization precession via microwave radiation. In magnet|metal heterostructures, the excited magnetization then emits a spin current into the metal in a process called spin pumping [7–10]. In this work, however, non-equilibrium magnons are excited via a pure DC spin current induced by the spin Hall effect (SHE) in a Pt contact [4, 6, 11], which generates a magnon accumulation in an adjacent ferrimagnetic insulator [12, 13]. This non-equilibrium magnon accumulation diffuses through the insulator and can be detected non-locally in a second electrically isolated Pt contact via the inverse spin Hall effect (ISHE) [5]. This so called magnon mediated magnetoresistance (MMR) [13] enables the DC electrical generation and detection of a pure magnon based spin current. In addition to this, magnons can be excited thermally as well, as enshrined in the spin Seebeck effect (SSE) [14–16]. Similar to the MMR, thermally excited non-equilibrium magnons are also transported diffusively and can be detected non-locally. We refer to this process as the non-local spin Seebeck

effect here [12,17]. In order to make use of the transport of either electrically or thermally injected magnons in the future, it is inevitable to understand the non-local magnon diffusion process in detail. To this end, we performed non-local MMR and SSE measurements as a function of temperature and magnetic field in ferrimagnetic garnet|platinum heterostructures. Additionally, we measured the non-local magnon transport for a large variety of devices with different Pt contact separations, in order to investigate the distance dependence of the diffusive magnon transport. Our investigation of the non-local magnon transport as a function of different external parameters (temperature, field and contact separation) allows for the distinction between different contributions, such as effects originating from the magnon spectrum, the diffusive spin transport process or interface related effects, in particular magnon excitation and detection. This distinction is very important for the investigation of new materials, since a profound understanding of the microscopic origin of the non-local spin transport enables a targeted search for materials which offer the desired properties for future spintronic applications. On a more applied perspective, we furthermore here demonstrate the implementation of a proof-of-principle logic device based on the non-local spin transport. In particular, we introduce a magnon-based majority gate, which enables logic operations such as "AND" and "OR". Devices based on this kind of magnon transport are fully functional at room temperature, making this effect very suitable for application. Within the frame of the implementation of a magnon-based majority gate, we demonstrate that magnons generated by different Pt contacts superimpose incoherently and show that an additional Pt contact within the magnon diffusion path has no detectable effect on the non-local signal.

One key insight obtained from this work, is that the thermally populated magnon spectrum has a profound impact on the MMR and non-local SSE. It therefore is of key importance to take magnon population statistics into account when modelling their transport. Furthermore, by rigorously investigating our temperature, magnetic field and contact separation dependent data, we find convincing evidence for the impact of optical magnon modes. The latter have a different polarity (or helicity) as compared to their low-energy acoustic counterparts, and thus induce a different sign of the non-local voltage signal. The qualitatively different field-induced shifts of acoustic and optical exchange magnon modes allow us to describe the characteristic field behaviour of the non-local spin transport in the ferrimagnetic insulator Yttrium-Iron-Garnet (YIG).

To our knowledge, this work also presents the first non-local magnon transport measurements in the canted ferrimagnet Gadolinium-Iron-Garnet (GIG). We thereby show that the model for the field dependence of the magnon transport we applied to YIG, which takes into account the specific magnon spectrum of the ferrimagnet, also works in a canted spin system such as GIG and yields a qualitative explanation for the observed features.

This thesis is organized as follows: Chapter 2 gives an overview of theoretical concepts required for this work. Experimental details regarding materials, fabrication and measurements techniques are presented in Chap. 3. The main focus of this thesis lies in Chap. 4, where we intensively discuss the electrical and thermal injection of magnons in non-local Yttrium-Iron-Garnet (YIG)|Platinum (Pt) bilayer structures. Based on the electrical MMR effect we demonstrate the implementation of a fully-functional magnon-based logic device in YIG|Pt bilayers in Chap. 5. In the subsequent Chap. 6, a first glance at the electrical and thermal injection of magnons into a canted spin system, namely the compensated ferrimagnet Gadolinium-Iron-Garnet (GIG), is given. Finally, Chapter 7 points out the main achievements of this work and gives an outlook for future experiments

in continuation of this work, as well as a first glance at non-local spin transport with ferromagnetic metal contacts on YIG.

Chapter 2

Theoretical Concepts

For the realization of functional spintronic devices, the generation and detection of spin currents is of key importance. Therefore, this Chapter gives an introduction to the principles of spin currents in Sect. 2.1, in particular also regarding their generation and detection via the spin Hall effect (SHE) [4,6,11] and the inverse spin Hall effect (ISHE) [5]. Furthermore, the spin Hall magnetoresistance (SMR), a magnetoresistive effect observed in bilayers consisting of a ferromagnetic insulator (FMI) and normal metal (NM) [18–20] is presented in Sect. 2.2. The spin-current based analogue to the ordinary Seebeck effect in metals, the spin Seebeck effect (SSE) [14–16,21], will be discussed thereafter in Sect. 2.3. Last but not least, the recently discovered non-local magnon mediated magnetoresistance (MMR) [12,13,22,23] effect, as well as a non-local counterpart of the spin Seebeck effect [17,33], is illustrated in Sect. 2.4.

2.1 Spin Currents

In a two current model (sorting the mobile electrons in an electric conductor into "spin up" and "spin down" according to their intrinsic spin angular momentum), the ordinary electric charge current density \mathbf{J}_c can be written as [24]

$$\mathbf{J}_c = \mathbf{J}_\uparrow + \mathbf{J}_\downarrow. \quad (2.1)$$

The subscripts here denote the electron spin polarization \mathbf{s} pointing up (\uparrow) or down (\downarrow) (c.f. Fig. 2.1 (a)). When an imbalance in the number density of up and down spin electrons occurs, the charge current is accompanied by a spin current (density)¹ [24]

$$\mathbf{J}_s = -\frac{\hbar}{2e}(\mathbf{J}_\uparrow - \mathbf{J}_\downarrow), \quad (2.2)$$

where $q = -e < 0$ is the charge of the electron and \hbar the reduced Planck constant. In conducting ferromagnets, a charge current with the spin current given by Eq. 2.2 is typically finite, since ferromagnets feature a difference in the number of up and down spin electrons. The two phenomena are often described together in terms of a spin polarized current, as shown in Fig. 2.1 (b). A pure spin current, however, will arise in the particular situation $\mathbf{J}_\uparrow = -\mathbf{J}_\downarrow$ (see Fig. 2.1 (c)).

In this work, the generation and detection of pure spin currents in metals is based on the spin Hall effect and the inverse spin Hall effect, respectively, as depicted in Fig. 2.2 (a)

¹In the following we use current and current density as synonyms to simplify wording.

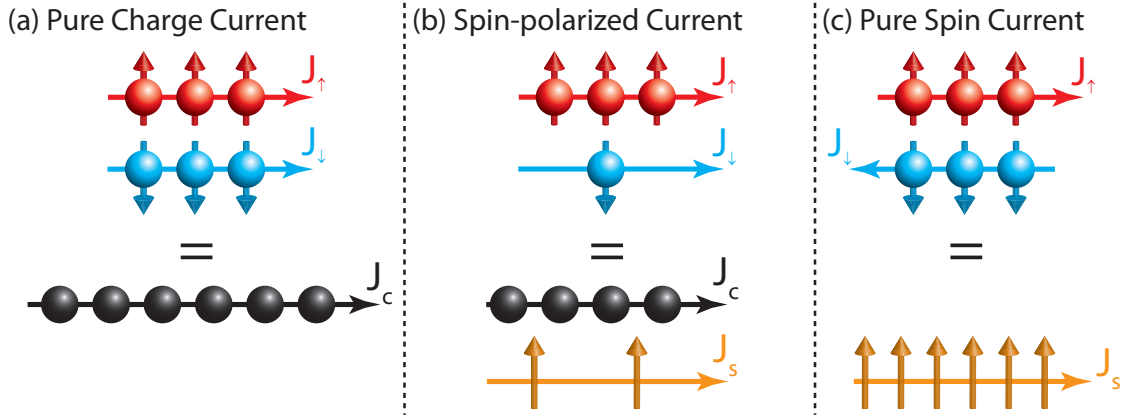


Figure 2.1: (a) An ordinary charge current \mathbf{J}_c in a normal metal can be divided into the flow of equal numbers of up and down spin electrons. (b) If the spin polarization of the electron system is finite, the charge current is accompanied by a flow of spin angular momentum. (c) For equal numbers of up and down spin electrons flowing in opposing directions, a pure spin current \mathbf{J}_s arises. Figure adapted from [24].

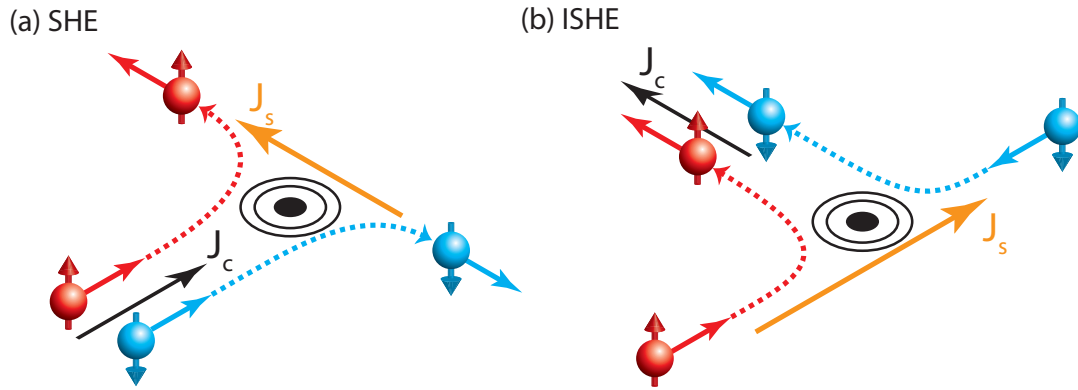


Figure 2.2: In paramagnetic materials the spin-orbit coupling leads to a spin dependent scattering of conduction electrons. (a) An applied charge current \mathbf{J}_c gives rise to a transverse pure spin current in the spin Hall effect (SHE). (b) The inverse spin Hall effect (ISHE) describes the transverse charge current \mathbf{J}_c caused by an incoming spin current \mathbf{J}_s .

and (b). For conductors with strong spin-orbit coupling the injection of a charge current leads to a transverse spin current, due to the spin Hall effect (SHE): [4]

$$\mathbf{J}_s^{\text{SHE}} = \Theta_{\text{SH}} \frac{\hbar}{2e} \mathbf{J}_c \times \mathbf{s}. \quad (2.3)$$

Θ_{SH} is the spin Hall angle, which parameterizes the conversion efficiency from charge to spin currents. For the detection of spin currents, one can take advantage of the inverse spin Hall effect (ISHE) [4, 5], which converts spin to charge currents according to

$$\mathbf{J}_c^{\text{ISHE}} = \Theta_{\text{SH}} \frac{2e}{\hbar} \mathbf{J}_s \times \mathbf{s}. \quad (2.4)$$

The efficiency of the spin-to-charge viz. charge-to-spin conversion Θ_{SH} is determined intrinsically by the bandstructure [25], as well as extrinsically by scattering from defects of

the material [26,27]. Microscopically, strongly spin orbit coupled metals are necessary for large spin Hall angles. Since the spin orbit coupling strength is proportional to the atomic number as Z^4 [28], heavy metals such as platinum (Pt) or tantalum (Ta) are materials of choice.

Note that the SHE and ISHE will arise only in metals, where the current is carried by electrons. However, spin currents also exist in ferrimagnetic insulators, where the angular momentum is carried by spin waves (magnons) [12, 13, 22, 23]. While the spin current generation via the SHE is well established, the excitation of magnon currents and their transport properties in ferrimagnetic insulators will be discussed in detail in this work (see Chap. 4).

2.2 Spin Hall Magnetoresistance

In bilayer structures consisting of a ferromagnetic insulator (FMI) and a normal metal (NM), a magnetization orientation dependent magnetoresistance can be observed, which is illustrated in Fig. 2.3.

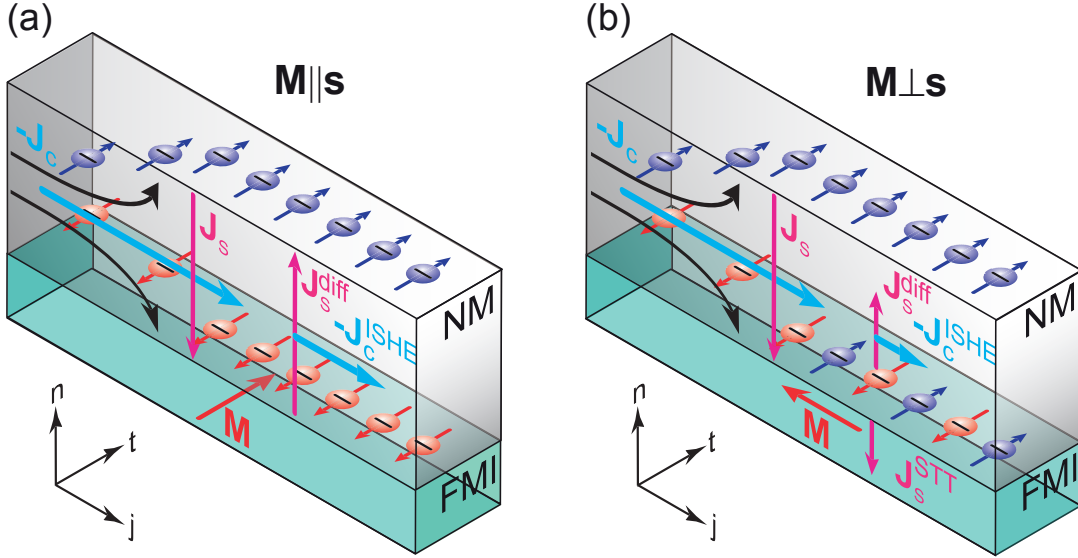


Figure 2.3: An incident charge current $-\mathbf{J}_c$ in the NM is partially converted to a transverse spin current \mathbf{J}_s , which generates a spin accumulation at the NM|FMI interface. (a) For $\mathbf{M} \parallel \mathbf{s}$, the spin accumulation cannot enter the FMI and remains at the interface, giving rise to a spin diffusion current flowing opposite to the SHE spin current \mathbf{J}_s . This spin backflow is converted back into a charge current $\mathbf{J}_c^{\text{ISHE}}$ via the inverse spin Hall effect. (b) For $\mathbf{M} \perp \mathbf{s}$, the spin accumulation exerts a spin transfer torque on the magnetization, such that a spin current $\mathbf{J}_s^{\text{STT}}$ is absorbed by the FMI. Thus the spin diffusion backflow is smaller than in the previous case, resulting in a lower ISHE current and eventually in a higher resistance. Figure taken from [29].

When a charge current $-\mathbf{J}_c$ is applied to the normal metal in the \mathbf{j} -direction, the spin Hall effect leads to a transverse spin current \mathbf{J}_s along $-\mathbf{n}$, i.e. perpendicular to the NM|FMI interface, with a spin polarization \mathbf{s} along $-\mathbf{t}$. Consequently, a spin accumulation μ_s arises at the interface, which interacts with the magnetization \mathbf{M} in the FMI. When the magnetization is pointing perpendicular to the electron spin polarization \mathbf{s} at the interface

(Fig. 2.3 (b)), a torque can be exerted on \mathbf{M} , such that the spin current is partially absorbed in the FMI. In the case where \mathbf{s} points along \mathbf{M} (Fig. 2.3 (a)), no torque can be transferred, which corresponds to a reflection of the spin current. Since the absorption (reflection) of the interface spin current constitutes more (less) dissipation for the initial charge current, a higher (lower) resistance is observed for $\mathbf{M} \perp \mathbf{s}$ ($\mathbf{M} \parallel \mathbf{s}$) [20].

In more detail, the spin accumulation at both interfaces of the NM leads to a gradient $\nabla \mu_{\mathbf{s}}$ in the spin chemical potential $\mu_{\mathbf{s}} = \mu_{\uparrow} - \mu_{\downarrow}$, which gives rise to a spin diffusion current following [20]

$$\mathbf{J}_{\mathbf{s}}^{\text{diff}} = \frac{\hbar \sigma}{2e^2} \nabla \mu_{\mathbf{s}}, \quad (2.5)$$

where σ is the electrical conductivity. The spin diffusion current points along $-\mathbf{J}_{\mathbf{s}}$ and is converted to a charge current $\mathbf{J}_{\mathbf{c}}^{\text{ISHE}}$ via the ISHE, which flows in the direction of the initial charge current $\mathbf{J}_{\mathbf{c}}$ (c.f. Fig. 2.3). For $\mathbf{M} \parallel \mathbf{s}$, the spin accumulation remains at the interface (as in a single NM layer) and the spin diffusion current $\mathbf{J}_{\mathbf{s}}^{\text{diff}}$ is high (due to a high $\nabla \mu_{\mathbf{s}}$). If $\mathbf{M} \perp \mathbf{s}$, a spin current according to $\mathbf{J}_{\mathbf{s}}^{\text{STT}} \propto g^{\uparrow\downarrow} \mathbf{m} \times (\mathbf{m} \times \mu_{\mathbf{s}})$ flows across the interface. The so called spin-mixing-conductance $g^{\uparrow\downarrow}$ reflects the number of open channels for spin transport across interfaces with non-collinear spins [30]. This reduces the spin accumulation at the NM|FMI interface such that also the spin diffusion current $\mathbf{J}_{\mathbf{s}}^{\text{diff}}$ is lowered. The reduction of the spin diffusion current in turn decreases the transverse charge current via the ISHE, giving rise to a higher resistance in the NM layer when $\mathbf{M} \perp \mathbf{s}$. Since the spin current across the NM|FMI interface depends on the relative orientation of magnetization and electron spin polarization, an magnetization orientation dependent resistance modulation of the NM layer arises. According to Ref. [20] this leads to the longitudinal spin Hall magnetoresistance (SMR) of the form

$$R_{\text{long}} = R_0 + R_1 m_t^2, \quad (2.6)$$

where m_t is the projection of \mathbf{M} onto the \mathbf{t} axis in Fig. 2.3, $R_0 = R_{\mathbf{M} \perp \mathbf{s}}$ the resistance maximum and $R_1 = R_{\mathbf{M} \parallel \mathbf{s}} - R_{\mathbf{M} \perp \mathbf{s}} < 0$. By applying an external magnetic field \mathbf{H} , the magnetization of the FMI can be rotated, giving rise to an a dependence of the resistance on the magnetization orientation α following

$$R_{\text{long}} = R_0 + R_1 \cos^2(\alpha). \quad (2.7)$$

The SMR ratio can then be written as

$$\text{SMR} = -\frac{R_1}{R_0} > 0. \quad (2.8)$$

2.3 Spin Seebeck Effect

In general, temperature gradients in material systems always lead to transport of mass, energy, quasiparticles etc. This is also true for spin angular momentum, leading to the so called spin Seebeck effect (SSE) [14, 15]. If one applies a temperature gradient $\nabla \mathbf{T}$ perpendicular to the interface of the previously discussed FMI|NM heterostructure, a magnon spin current $\mathbf{J}_{\mathbf{s}}$ arises in the bulk of the FMI, which is continuously pumped into the adjacent NM layer. This phenomenon is illustrated in Fig. 2.4. Via the inverse spin

Hall effect, this thermally driven spin current can be detected electrically in the NM as a voltage $V_{\text{SSE}}^{\text{ISHE}}$ in open circuit conditions. According to a widely accepted theory [14,15], the thermal spin current is driven by a temperature difference $\Delta T_{\text{em}} = T_{\text{m}} - T_{\text{e}}$ of the temperature T_{m} of the magnonic subsystem in the FMI and the temperature T_{e} of the electronic subsystem in the NM. The detected voltage $V_{\text{SSE}}^{\text{ISHE}}$ is therefore proportional to the electron-magnon temperature difference ΔT_{em} [14]. Since the direction of the charge current generated via the ISHE is dependent on the orientation of the spin polarization \mathbf{s} of the spin current, which in turn is determined by magnetization orientation \mathbf{M} , the spin Seebeck effect shows a characteristic magnetization orientation dependent modulation of $V_{\text{SSE}}^{\text{ISHE}}$. In the device geometry shown in Fig. 2.4, the SSE voltage follows a $\cos(\alpha)$ dependence (with α the angle enclosed by the magnetization with respect to the \mathbf{t} -axis). Since a 180° rotation of the magnetization in Fig. 2.4 (then pointing in negative \mathbf{t} direction) leads to an inversion of the ISHE current $\mathbf{J}_{\text{c}}^{\text{ISHE}} \propto \mathbf{J}_{\text{s}} \times \mathbf{s}$, the SSE voltage $V_{\text{SSE}}^{\text{ISHE}}$ changes sign. For $\alpha = 90^\circ$ turn, however, no voltage can be measured in the measurement geometry of Fig. 2.4, since the arising ISHE charge current flows perpendicular to the \mathbf{j} -direction, and no voltage probes are attached in this direction.

In this thesis, the heating of the metal layer for the spin Seebeck effect is solely achieved by applying an ordinary charge current I_{c} which dissipates energy by Ohmic losses [16]. The temperature difference ΔT_{em} is proportional to the temperature increase due to Joule heating in the NM and therefore also proportional to the electric heating power P_{JH}

$$P_{\text{JH}} = RI_{\text{c}}^2 \quad (2.9)$$

with R the electrical resistance of the NM. As a consequence, a quadratic dependence of the SSE current-voltage characteristic is expected ($V_{\text{SSE}} \propto I_{\text{c}}^2$).

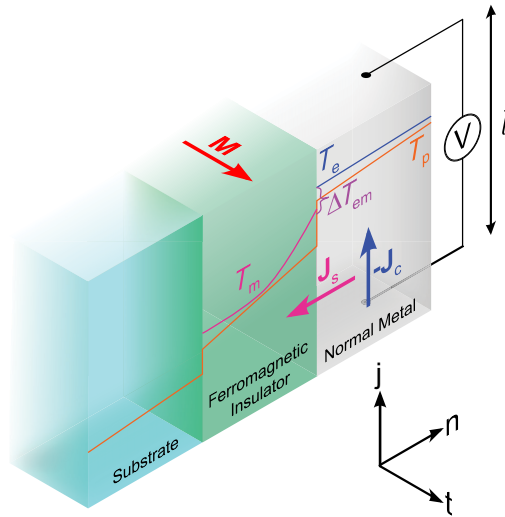


Figure 2.4: A temperature difference ΔT_{em} between the electron and magnon temperature at the FMI|NM interface gives rise to an interface spin current \mathbf{J}_{s} which can be detected via the ISHE in the NM. Since the polarization of the spin current is given by the magnetization direction of the FMI, the direction of the inverse spin Hall charge current \mathbf{J}_{c} is dependent on the magnetization orientation. Thus the SSE signal shows a characteristic modulation with the orientation α of the magnetization \mathbf{M} . Figure taken from [15].

2.4 Non-local Spin Transport

In FMI|NM bilayers it is possible to perform non-local magnon transport measurements with structures as depicted in Fig. 2.5. Here, two metal strips with a separation d are deposited on a FMI layer. Applying a charge current to the left strip (the "injector") leads to a spin accumulation at the interface due to the SHE (see Sect. 2.2), which in turn generates magnons (spin waves) in the FMI. The generated non-equilibrium magnon density gives rise to a diffusion of magnons in the FMI [12,13,31]. In the second, electrically isolated metal strip (the "detector") the magnon spin diffusion current can be detected via the ISHE.

The creation of magnons is only possible for a collinear configuration of spin polarization \mathbf{s} and magnetization \mathbf{M} . Microscopically, this can be explained by a scattering process of electronic spins at the interface [12, 22]. Due to conservation of angular momentum, a spin flip scattering process at the NM|FMI interface leads to the creation (when \mathbf{M} antiparallel to $-\mathbf{s}$) or annihilation (when \mathbf{M} parallel to $-\mathbf{s}$) of thermal magnons². Here the spin to magnon and magnon to spin conversion efficiencies at the interface can be parameterized by the spin conversion efficiency g_s as described in Ref. [31]. Assuming that these non-equilibrium magnons are predominantly affected by magnon number-conserving processes (until they are detected in the second strip), a magnon spin chemical potential μ_m can be defined [31]. A simple Boltzmann transport

theory treatment with a bosonic distribution function $f(\mathbf{r}, \epsilon) = \left(\exp\left(\frac{\epsilon - \mu_m(\mathbf{r})}{k_B T_m(\mathbf{r})}\right) - 1 \right)^{-1}$ then leads to the diffusion equation of magnons

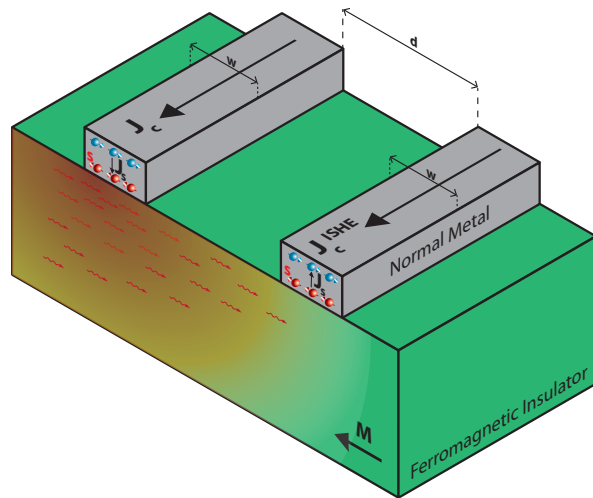


Figure 2.5: Sketch of a FMI|NM bilayer structure with two electrically isolated metal strips. A charge current \mathbf{J}_c is applied to the left strip (the "injector"), giving rise to a transverse spin current \mathbf{J}_s via the spin hall effect. The emerging spin accumulation at the interface either excites or annihilates non-equilibrium magnons in the FMI, depending on the direction of the interface electron spins. The non-equilibrium magnon accumulation μ_m gives rise to a diffusion throughout the FMI, which can be detected non-locally as a voltage V_{nl}^{res} in the right metal strip via the inverse spin hall effect.

$$\frac{\partial^2 \mu_m}{\partial x^2} = \frac{\mu_m}{\lambda_m^2} \quad (2.10)$$

²Note, that the spin angular momentum \mathbf{s} is defined to point antiparallely to the magnetic moment, which corresponds to the magnetization direction \mathbf{M} . In order to create (annihilate) a magnon in the FMI according to angular momentum conservation, the spin polarization \mathbf{s} at the interface must therefore be aligned parallel (antiparallel) to \mathbf{M} .

with λ_m the magnon diffusion length. If the non-equilibrium magnons reach the detector strip, an electronic spin accumulation is induced in the NM layer. The emerging spin current in the detector strip can then be detected as a voltage $V_{\text{nl}}^{\text{res}}$ via the ISHE. We will call this effect the (non-local) magnon mediated magnetoresistance (MMR) [13]. Note, that a spatially dependent magnon temperature profile $T_m(\mathbf{r})$ also leads to a transport of magnons due to a gradient in $T_m(\mathbf{r})$ within the Boltzmann transport theory. However, it was calculated that the magnon temperature T_m reaches the equilibrium at much shorter length scales than the magnon chemical potential μ_m [15,31]. Therefore the contribution of $T_m(\mathbf{r})$ is only present on length scales of a few 10 nm, whereas the contribution of μ_m is dominant at length scales of a few μm [12]. The magnon injection as well as the magnon detection are dependent on the relative angle α between the magnetization of the FMI and the spin polarization at the interface. As a result, a $V_{\text{nl}}^{\text{res}} \propto \cos^2(\alpha)$ dependence is expected. While the MMR signal evolution with α thus is qualitatively similar to the previously discussed SMR, the physical origin of the effects is qualitatively different.

Due to heating effects induced by the applied charge current \mathbf{J}_c in the injector strip, magnons are excited thermally as well, which we already discussed by means of the spin Seebeck effect in Sect. 2.3. Thereby, the thermal excitation always generates magnons with magnetic moment \mathbf{m} pointing antiparallely to the magnetization \mathbf{M} , since the thermal energy always acts as a disturbance of the magnetic order (parameterized by the magnetization \mathbf{M}). Similar to the electric excitation, the thermal excitation of non-equilibrium magnons also gives rise to a diffusion of these, such that a non-local thermal voltage $V_{\text{nl}}^{\text{therm}}$ can be measured at the detector strip [12,32,33]. The thermal excitation of magnons is independent of the magnetization orientation, such that the resulting angular dependence of the measured voltage follows $V_{\text{nl}}^{\text{therm}} \propto \cos(\alpha)$, since only the detection exhibits a magnetization orientation dependence (similar to the local SSE). Note, that similar to the electrical MMR effect, also the thermally injected magnons are very likely to originate mainly from a gradient in the magnon chemical potential μ_m , and not in a gradient from the magnon temperature T_m [31]. We will call this phenomenon the non-local spin Seebeck effect here [17,32].

Chapter 3

Experimental Details

This thesis is focussed on the non-local magnon transport processes introduced in Sect. 2.4. In order to study and understand the non-local magnon transport processes, we have patterned platinum (Pt) strips with separation d and width w onto the magnetic insulators Yttrium-Iron-Garnet ($\text{Y}_3\text{Fe}_5\text{O}_{12}$, YIG) as well as Gadolinium-Iron-Garnet ($\text{Gd}_3\text{Fe}_5\text{O}_{12}$, GIG). We start by reviewing some important properties of these insulating ferrimagnets.

3.1 Material Systems

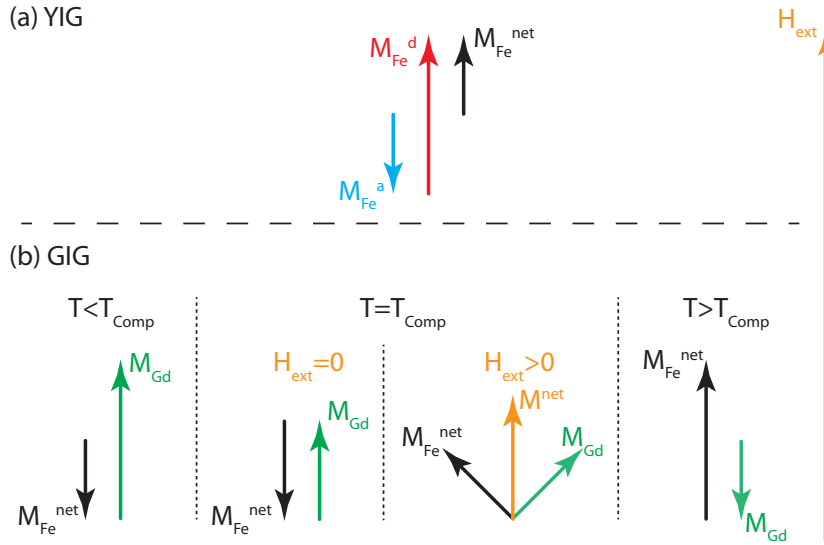


Figure 3.1: (a) Iron sublattice magnetizations \mathbf{M}_{Fe}^d (red) and \mathbf{M}_{Fe}^a (blue) of the Fe^{3+} ions on the tetrahedrally and octahedrally coordinated lattice sites d and a in YIG, respectively. The net magnetization $\mathbf{M}_{\text{Fe}}^{\text{net}}$ (the YIG net magnetization) always points along the external field \mathbf{H}_{ext} . (b) Sublattice magnetizations of GIG for $T < T_{\text{Comp}}$, where the Gd magnetization \mathbf{M}_{Gd} dominates. At the compensation temperature ($T = T_{\text{Comp}}$), the net iron moment and the Gd moment compensate each other. A finite external magnetic field H_{ext} induces the spin canting phase, where the sublattice magnetizations enclose a finite angle with respect to the external field direction. For $T > T_{\text{Comp}}$ the net iron moment exceeds the Gd moment. Figure adapted from [34].

YIG exhibits two antiferromagnetically coupled Fe^{3+} sublattices with magnetizations $\mathbf{M}_{\text{Fe}}^a < \mathbf{M}_{\text{Fe}}^d$, where \mathbf{M}_{Fe}^d and \mathbf{M}_{Fe}^a correspond to the Fe^{3+} ions on the tetrahedrally and

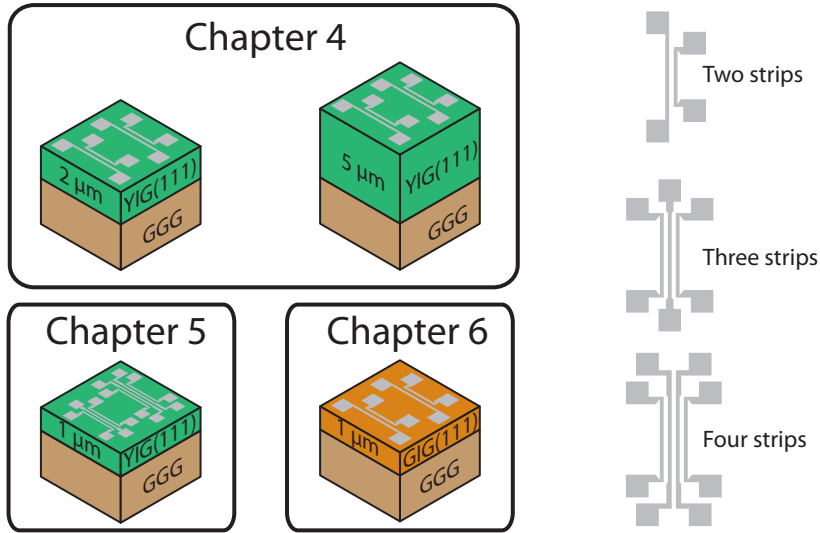


Figure 3.2: Schematics of all samples presented in this work, including the thin film thicknesses of the insulating magnets. The Pt thicknesses are approximately 10 nm for all samples. Several two strip configurations with varying strip-separations d and strip widths w were structured. As discussed in more detail in Chap. 5, we also made three and four strip devices on YIG.

octahedrally coordinated lattice sites d and a, respectively [35,36]. Because of the very strong antiferromagnetic coupling [37], an antiparallel Fe sublattice state persists up to external magnetic fields of $\mu_0 H = 300$ T [35]. Since the iron moments are so strongly locked, YIG can be treated as a one-sublattice ferromagnet in good approximation, with a net Fe sublattice $\mathbf{M}_{\text{Fe}}^{\text{net}}$. The sublattice configuration of YIG is depicted in Fig. 3.1 (a).

GIG has the same crystalline structure as YIG, but the non-magnetic Y^{3+} is substituted with Gd^{3+} , which exhibits a magnetic moment. Therefore, GIG is a complex magnet with three sublattice magnetizations consisting of the net magnetization of the two antiferromagnetically coupled iron sites, $\mathbf{M}_{\text{Fe}}^{\text{net}} = \mathbf{M}_{\text{Fe}}^{\text{d}} + \mathbf{M}_{\text{Fe}}^{\text{a}}$ and a magnetization $\mathbf{M}_{\text{Gd}}^{\text{c}}$ which is antiferromagnetically coupled to the net iron moment. The magnitude of the Gd sublattice magnetization shows a Brillouin-type dependence on temperature and magnetic field, leading to an increase of $\mathbf{M}_{\text{Gd}}^{\text{c}}$ with decreasing temperature. This gives rise to the phenomenon of magnetic compensation: owing to the antiparallely ordered net Fe and Gd magnetization and the strong temperature dependence of the latter, a compensation occurs for $\mathbf{M}_{\text{Fe}}^{\text{net}} = -\mathbf{M}_{\text{Gd}}^{\text{c}}$ at a certain temperature T_{Comp} , where the overall net magnetization $\mathbf{M}^{\text{net}} = \mathbf{M}_{\text{Fe}}^{\text{net}} + \mathbf{M}_{\text{Gd}}^{\text{c}}$ vanishes. An externally applied magnetic field $\mu_0 \mathbf{H}_{\text{ext}}$ gives rise to the so called spin canting phase close to T_{Comp} , where the net iron moment and the Gd moment rotate away from their antiparallel configuration and enclose a finite angle $\gamma \neq 0^\circ, 180^\circ$ [35,37,38]. The overall net magnetization, however, still points along the external field. The sublattice configurations of GIG around the compensation temperature T_{Comp} are shown in Fig. 3.1 (b).

In this work we focus on FMI|Pt bilayers. The magnetic insulator layers (YIG or GIG) were deposited onto Gadolinium-Gallium-Garnet (GGG) substrates. The Pt layers are patterned into pairs of parallel strips mutually isolated from one another, or into sets of three or four parallel strips (again electrically isolated from one another). This is

summarized in Fig. 3.2, where the corresponding samples are listed for each Chapter, including the thin film thicknesses. In the following, Sect. 3.2 gives a detailed description of the sample fabrication, while Sect. 3.3 describes the measurement techniques used in this work.

3.2 Fabrication

The fabrication process is the same for all samples presented in this thesis. All magnetic thin films (YIG and GIG) were grown by liquid phase epitaxy (LPE) on GGG substrates. For the YIG films, the LPE growth was performed by a commercial supplier. The GIG sample was fabricated at Tohoku University by Dr. Qui in the group of Prof. Saitoh. The thicknesses of the garnet layers are summarized in Fig. 3.2. After we received the magnetic thin films, we cleaned them for 2 min to 5 min in Piranha solution¹ and then immersed them shortly in deionized (DI) water. The respective samples are then transferred into the vacuum chamber of the thin film cluster at the Walther-Meißner-Institut and annealed for 40 min at 500 °C in O₂ atmosphere (75 μ bar). Thereafter, 10 nm of Pt is deposited in situ via electron beam evaporation.

Prior to the patterning process, each sample is cleaned in acetone and isopropyl alcohol afterwards in an ultrasonic bath, for 2 min each. To remove any residual water on the surface, the sample is then shortly baked on a hot plate for approximately 2 min at 200 °C. Subsequently, CSAR62 resist is spin coated with 2000 rpm for 60 s and baked afterwards at 150 °C for 1 min. In order to enable focussing of the scanning electron microscope for the electron beam lithography, gold nanoparticles are applied on the edges of the sample. The bi-layer heterostructure is eventually

transferred to a NanoBeam nb5 electron beam lithography (EBL) system and exposed to the negative of the structure with a base dose of 0.7 C/m². After writing, the sample is developed in Allresist AR 500-49 for 60 s and then rinsed twice in isopropyl to stop the reaction. Thereafter, the chip is dry-blown with a nitrogen gun and etched by argon ion beam milling for 1.5 min. After etching, the remaining resist is removed using an Allresist AR 500-79 Remover, and once again cleaned in acetone and isopropyl. The contact pads are bonded with aluminium wires to a chip carrier with 20 copper contacts, which is plugged to a cryostat dipstick thereafter.

Figure 3.3 shows a schematic illustration of a YIG|Pt two strip structure (panel a) and

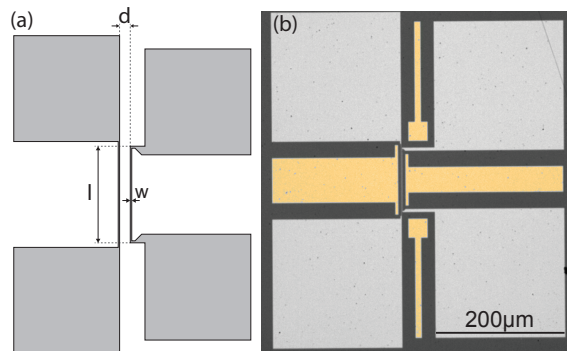


Figure 3.3: (a) Schematic illustration of the two strip structure. The left strip is denoted as the injector, whereas the right strip is the detector. (b) Optical micrograph of a YIG(dark)|Pt(bright) two strip structure. The yellow coloured Pt pads are structured to minimize the integral exposure dose for the nano-strips. Figure taken from [34].

¹Piranha solution is conc. H₂SO₄ mixed with 30% H₂O₂ 3:1 by volume. The sample is immersed into the Piranha solution directly after mixing while the solution is still hot.

an optical micrograph of a patterned device in panel (b). The yellow colored pads represent proximity Pt patches used to minimize the integral exposure dose for the nano-strips. The dimensions of the strips have to be chosen such that the aspect ratio length/width and consequently the resistance of the strip is large compared to contact pads. This ensures that the detected non-local voltage is dominated by the thin strip with defined geometry, and additional contributions from the leads can be neglected. Therefore, the strip widths were chosen to $w = 500 \text{ nm}$ or $w = 1 \mu\text{m}$, while the strip length $l = 100 \mu\text{m}$ for all samples, except for the three and four strip structures in Chap. 5, which have a length of approximately $l = 150 \mu\text{m}$. In order to characterize the magnon transport over a wide distance range, edge-to-edge strip separation distances from $d = 20 \text{ nm}$ to $10 \mu\text{m}$ were fabricated.

3.3 Measurement Techniques

After the sample is attached to a cryostat dipstick and inserted into a superconducting magnet cryostat, different types of measurements can be conducted. We in particular performed magnetotransport experiments, rotating the externally applied magnetic field orientation with respect to the sample in three different rotation planes, as illustrated in Fig. 3.4 (a) to (c). Throughout this thesis, these measurements are mostly denoted as angle dependent magnetoresistance (ADMR) measurements².

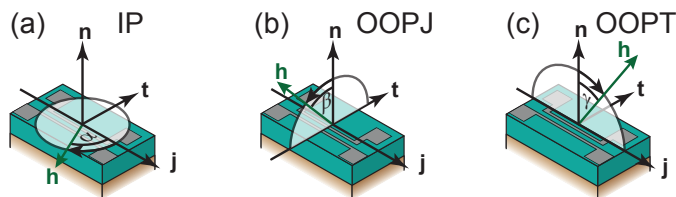


Figure 3.4: Schematic illustration for the three orthogonal magnetic field rotation planes. (a) The external magnetic field is rotated in the thin film plane (IP). (b) The field is rotated out of plane around the \mathbf{j} -axis (OOPJ). (c) Out of plane rotation around the \mathbf{t} -axis (OOPT). Figure taken from [34].

Moreover, three different magnet cryostat systems are used within this work. For all of the measurements in Chap. 4 and 6, we used a liquid helium-cooled cryostat with a 1D split coil superconducting magnet with a maximum field strength of $\mu_0 H = 7 \text{ T}$. Upon appropriate mounting on the dipstick, the sample can be rotated in all three rotation planes as defined in Fig. 3.4. Note that the sample needs to be dismounted and remounted between measurements in different planes. The cryostat furthermore covers a temperature range of $3 \text{ K} < T_{\text{cryo}} < 300 \text{ K}$ with a precision of $\pm 10 \text{ mK}$.

For the in plane magnetic field sweeps presented in Chap. 4, additionally a superconducting solenoid magnet cryostat with a maximum field strength of $\mu_0 H = 15 \text{ T}$ and a temperature range of $1.5 \text{ K} < T_{\text{cryo}} < 300 \text{ K}$ was used.

For the measurements in Chap. 5, we used a superconducting magnet cryostat with a 3D vector magnet enabling a maximum field of $\mu_0 H = 2 \text{ T}$ in all directions, as well as a

²The term "angle dependent" is actually not an ideal terminology for this kind of measurements, since we measure as a function of the magnetic field orientation and not as a function of "angle". However, we will use the term "angle dependent" mostly in this thesis to simplify wording.

field strength of $\mu_0 H = 6 \text{ T}$ in the vertical axis.

In this work, thermal and resistive effects are both examined upon applying charge currents. Thermal signals are generated by the Joule heating effect accompanying the applied charge current (thermal signals thus scale as the square of the applied current), while the resistive contribution is measured as the voltage across the metal strip linear in current. To distinguish between these contributions, the so-called current reversal technique is used. We iteratively apply positive and negative currents to the injector strip and measure the respective voltages arising across the detector strip V_+ and V_- with a nanovoltmeter. The resistive contribution is linear in current and can thus be calculated as

$$V_{\text{res}} = \frac{V_+ - V_-}{2}. \quad (3.1)$$

All thermal voltages that are independent of the current direction are eliminated this way. Thermal contributions, however, are calculated as the symmetric part

$$V_{\text{therm}} = \frac{V_+ + V_-}{2}, \quad (3.2)$$

which gives zero for purely resistive contributions. When heating effects play a role, the positive and negative voltages do not have the same magnitude anymore and the thermal contribution becomes finite. Throughout this work, the current reversal method is implemented in the measurement software.

Figure 3.5 depicts the two strip structure including the wiring scheme. We apply a current I with a Keithley 2400 Sourcemeter to the left (injector) strip and measure the local voltage V_{loc} with a Keithley 2182 nanovoltmeter at the same strip, resulting in a 4-point-measurement geometry that suppresses all contact resistances. The non-local voltage V_{nl} is measured simultaneously at the right (detector) strip with an additional Keithley 2182 nanovoltmeter. All measured voltages are recorded with the help of a Labview program that triggers the measurement units prior to each readout. The current reversal is applied five times in a row in order to be able to average for each data point. For the non-local current-voltage characteristics in Chap. 5 up to 100 current switches are applied to further increase the signal to noise ratio. In all of our local and non-local measurements we use a repeating filter setting, which averages 30 times intrinsically for each readout. With these settings it is possible to reach a non-local noise floor of approximately 5 nV for the resistive part, while the thermal response exhibits 25 nV noise (see Ref. [34]) for details).

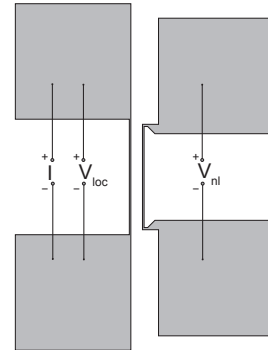


Figure 3.5: A current source is attached to the injector (left), while the local voltage V_{loc} is measured across that same strip. The non-local voltage V_{nl} is simultaneously measured across the detector strip (right). Figure taken from [34].

Chapter 4

Non-local Spin Transport in YIG|Pt Nanostructures

This Chapter focusses on non-local magneto-transport measurements on a YIG|Pt heterostructure with two parallel, electrically isolated platinum strips. The device structure was introduced in Chap. 3. By applying an injector current $I = 100 \mu\text{A}$ with a Keithley 2400 Sourcemeter to one Pt strip, non-equilibrium magnons are generated electrically and/or thermally in the YIG [12, 13] (see Sect. 2.4). The electrically- (or thermally-) induced magnon accumulation diffuses through the YIG and is detected in the second Pt strip as a non-local resistive (thermal) voltage signal $V_{\text{nl}}^{\text{res}}$ ($V_{\text{nl}}^{\text{therm}}$) with a Keithley 2182 Nanovoltmeter. Additionally, the *local* resistive and thermal signals $V_{\text{loc}}^{\text{res}}$ and $V_{\text{loc}}^{\text{therm}}$ at the injector strip are measured with a second Nanovoltmeter in a 4-point-measurement geometry (c.f. Sect. 3.3 Fig. 3.5) in order to compare the local and the non-local response. Thermal and resistive contributions are separated by exploiting their different dependence on the applied current I (odd and even powers of I , respectively), as described in Sect. 3.3. In order to gain a profound understanding of the diffusive magnon transport in YIG, in plane field rotations up to $\mu_0 H = 7 \text{ T}$ and fieldsweeps up to $\mu_0 H = 15 \text{ T}$ in a temperature range of $5 \text{ K} < T < 300 \text{ K}$ are discussed in the following. Rotations in the OOPJ and OOPT configurations were conducted solely at $T = 300 \text{ K}$ (see Fig. 3.4). To characterize the magnon transport, which is parameterized by the magnon diffusion length λ_m (c.f. Sect. 2.4), several pairs of Pt strips with edge-to-edge separations (gaps) varying from $d = 20 \text{ nm}$ to $d = 10 \mu\text{m}$ with a constant strip width of $w = 500 \text{ nm}$ are investigated. In the following, Sect. 4.1 focusses on the resistive response, while Sect. 4.2 is devoted to the thermal response of the local and non-local signals.

4.1 Resistive Contribution

For the discussion of the resistive response (i.e. purely "Ohmic" voltage contributions), a $2 \mu\text{m}$ thick YIG film with a pair of 10 nm thick platinum strips (c.f. Fig. 3.3 in Sect. 3.2) is investigated. Firstly, the SMR (c.f. Sect. 2.2), which can be measured as the local resistive signal at the injector strip, is shown in Fig. 4.1 (a)-(c) at $T = 300 \text{ K}$ and a field strength $\mu_0 H = 1 \text{ T}$ for all three rotation planes ¹. Note that the local signals $V_{\text{loc}}^{\text{res}}$ are normalized to the the maximum voltage level V_0 , at which the field points along the Pt strips. The SMR modulates like $\cos^2(\alpha)$ when the external field is rotated in the IP or OOPJ configurations. As described in Sect. 2.2, the magnetic field orientation dependent modulation arises from the varying boundary conditions for the SHE-induced spin current

¹The asymmetry of the local SMR signal is due to a slight thermal drift during the measurement, that changes the resistance of the Pt strip and consequently the measured voltage.

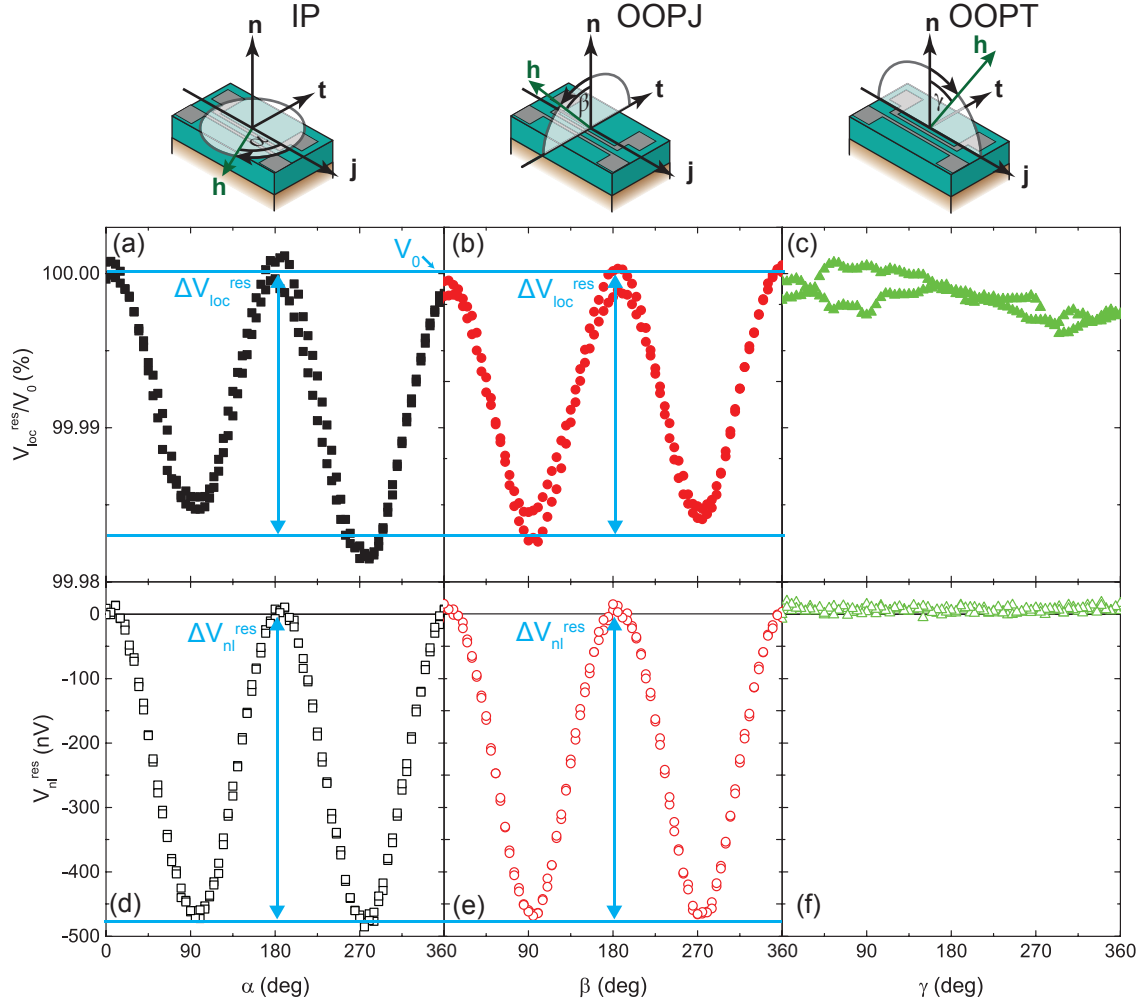


Figure 4.1: Local resistive part $V_{\text{loc}}^{\text{res}}$ of the SMR normalized to the maximum voltage level V_0 when rotating the magnetic field $\mu_0 H = 1$ T at $T = 300$ K for a strip width of $w = 500$ nm in (a) the in plane configuration (IP), (b) the out of plane around the current direction (OOPJ) and (c) for a rotation of the magnetic field in the \mathbf{n} - \mathbf{j} -plane (OOPT). The non-local MMR signal $V_{\text{nl}}^{\text{res}}$ for a structure with strip distance $d = 20$ nm is shown for the same experimental parameters as the local ones in (d) for the in plane rotation (IP), (e) in out of plane around current direction (OOPJ) and (f) in out of plane around the transverse \mathbf{t} direction (OOPT). The non-local signal goes to zero for field directions which are perpendicular to the SHE-induced interface spin accumulation.

impinging on the YIG/Pt interface when the orientation of the magnetization \mathbf{M} changes its direction with respect to the electron spin chemical potential $\boldsymbol{\mu}_s$. This changes the ability of the SHE-spin current to enter the YIG, since spin transfer torque is only finite when $\mathbf{M} \perp \boldsymbol{\mu}_s$, while zero for $\mathbf{M} \parallel \boldsymbol{\mu}_s$ (c.f. Sect. 2.2). Since for an OOPT-rotation (panel (c)) the external field and therefore the magnetization of YIG always points perpendicular to the interface electron spin accumulation $\boldsymbol{\mu}_s$, no modulation of the ISHE voltage signal should appear in this rotation plane. This is consistent with our experimental observations (see Fig. 4.1 (c)). By fitting the signals with $\Delta V_{\text{loc}}^{\text{res}} \cos^2(\alpha)$, the voltage amplitudes $\Delta V_{\text{loc}}^{\text{res}}$

can be extracted. Thereafter, the SMR ratio $\frac{\Delta V_{\text{loc}}^{\text{res}}}{V_0}$ is calculated and investigated as a function of temperature and magnetic field in the following sections.

The resistive voltage modulations for the non-local signals, which we denote as the MMR [13], are shown in panels (d)-(f) of Fig. 4.1 for all three rotation planes and a strip separation $d = 20$ nm. Similar to the SMR, the MMR modulates like $\cos^2(\alpha)$ when the external field is rotated IP or OOPJ (c.f. Sect. 2.4), while it becomes zero for all angles when \mathbf{H} is rotated OOPT. This is expected, since the MMR goes to zero for magnetization directions which are perpendicular to the SHE-induced interface spin accumulation ($\mathbf{M} \perp \boldsymbol{\mu}_s$), while it becomes finite for a collinear configuration $\mathbf{M} \parallel \boldsymbol{\mu}_s$. Magnons always carry spin angular momentum which is collinear to the magnetization \mathbf{M} , such that the interchange of spin angular momentum between the electron spin accumulation $\boldsymbol{\mu}_s$ and the YIG magnon system for $\mathbf{M} \perp \boldsymbol{\mu}_s$ vanishes. As proposed in Ref. [31], transverse components of the angular momentum can be neglected due to the small magnetic exchange length of a few 10 nm in YIG, which is much smaller than our typical system size [39]. When $\boldsymbol{\mu}_s$ is collinear to \mathbf{M} , however, spin moment can be interchanged between $\boldsymbol{\mu}_s$ and the magnon system, which leads to the generation of diffusing non-equilibrium magnons (with angular momentum along \mathbf{M}) which can be detected non-locally as a voltage signal (c.f. Sect. 2.4). The amplitude $\Delta V_{\text{nl}}^{\text{res}}$ of the MMR modulations is extracted by fitting $\Delta V_{\text{loc}}^{\text{res}} \cos^2(\alpha)$ to the data. Since $\Delta V_{\text{loc}}^{\text{res}}$ is a direct measure for the diffusive magnon transport properties in YIG, it is investigated in-depth by systematically varying the external parameters temperature, magnetic field and strip separation distance in the following sections. To keep the experimental effort reasonable, this is done solely for in plane field rotations and field sweeps.

4.1.1 Temperature Dependence

4.1.1.1 Spin Hall Magnetoresistance

At first, the temperature evolution of the local SMR modulations are investigated. The angle dependent magnetoresistance (ADMR) (c.f. Sect. 3.3) measurements of the SMR voltage signal $V_{\text{loc}}^{\text{res}}$ are depicted in Fig. 4.2 (a) at $\mu_0 H = 1$ T exemplarily for three different temperatures. Panel (b) shows the corresponding SMR ratio $\Delta V_{\text{loc}}^{\text{res}}/V_0$ as a function of temperature for two different devices. We find a SMR ratio $\frac{\Delta V_{\text{loc}}^{\text{res}}}{V_0} \approx 1.7 \times 10^{-4}$ at $T = 300$ K, which is considerably lower than typical values of $\frac{\Delta V_{\text{loc}}^{\text{res}}}{V_0} \approx 5 \times 10^{-4}$ [19]. However, this discrepancy is likely to be ascribed to the ex situ platinum deposition process and thus attributed to a reduced interface quality in comparison to the in situ Pt deposition process used to obtain maximum SMR modulation at WMI. The temperature evolution of the SMR shows an increase with decreasing temperature from 300 K down to ~ 150 K [40]. A decreasing trend is observed for lower temperatures down to ~ 15 K [41]. For very low temperatures between 15 K and 5 K a further enhancement is observed. This temperature dependence does not match with the monotonously decreasing behaviour with decreasing temperature reported in Ref. [41] for temperatures below 300 K. However, the behaviour shown in Fig. 4.2 (b) was previously observed on samples with ex situ applied platinum films. Thus, the temperature dependent SMR properties of the sample considered here must be attributed to the interface quality. However, this work focusses on the non-local magnon transport and we therefore do not study the SMR temperature behaviour in further detail.

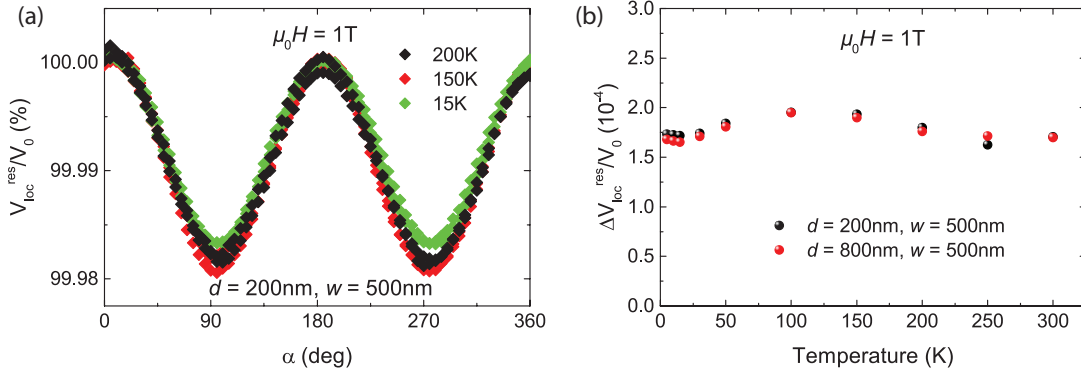


Figure 4.2: (a) Angle dependent SMR response (local signal $\frac{V_{\text{loc}}^{\text{res}}}{V_0}$) for three different temperatures at $\mu_0 H = 1$ T on a YIG|Pt device with $d = 200$ nm and $w = 500$ nm. (b) SMR ratio $\frac{\Delta V_{\text{loc}}^{\text{res}}}{V_0}$ plotted versus temperature for two different devices fabricated in the same run.

4.1.1.2 Magnon Mediated Magnetoresistance

As a next step, we investigate the temperature dependence of the non-local MMR for different strip separations d . In Figure 4.3 (a) the angle dependent MMR modulation is shown for temperatures $T = 10$ K, $T = 150$ K and $T = 300$ K for an applied field of $\mu_0 H = 1$ T on a device with $d = 200$ nm. The signal vanishes for temperatures below $T = 10$ K within the experimental resolution. The MMR amplitude $\Delta V_{\text{nl}}^{\text{res}}$, extracted from $\cos^2(\alpha)$ -fits to the angle dependent magnetoresistance (ADMR) measurements (c.f. Sect. 3.3) shown in panel (a), is plotted versus temperature in Fig. 4.3 (b) for all studied devices with injector-detector distances ranging from $d = 20$ nm to $10 \mu\text{m}$ with an applied external field of $\mu_0 H = 1$ T. Figure 4.3 (c) depicts the absolute value of $\Delta V_{\text{nl}}^{\text{res}}$ on a double-logarithmic scale, where the shaded region represents the noise floor of 5 nV (c.f. Sect. 3.3).

The solid lines in Fig. 4.3 (c) correspond to power law fits following $\Delta V_{\text{nl}}^{\text{res}} = A \cdot T^{\alpha_{\text{low}}}$ and $\Delta V_{\text{nl}}^{\text{res}} = B \cdot T^{\alpha_{\text{high}}}$ with fit parameters A , B , α_{low} and α_{high} . Thereby we separately fit the low temperature regime $5 \text{ K} < T < 100 \text{ K}$ (with exponent α_{low}) and the high temperature regime $100 \text{ K} < T < 300 \text{ K}$ (with α_{high}), since different exponents α are clearly evident in Fig. 4.3 (c). While for the low temperature regime we find $\alpha_{\text{low}} \approx 1.6 \cdots 0.5$ (from short to large distances d), the exponents for the high temperature regime suggest $\alpha_{\text{high}} \approx 1 \cdots 0.2$. In Ref. [23] a power law-temperature dependence following T^α emerging from the interface spin to magnon and magnon to spin conversion efficiencies ($G_{\text{em}} \propto T^{\frac{3}{2}}$ and $G_{\text{me}} \propto T$ in Ref. [23]) is predicted. Moreover, recent publications on the theory of the MMR claim that an effective spin mixing conductance $g_s = \gamma g^{\uparrow\downarrow}$ with $\gamma \propto \left(\frac{T}{T_C}\right)^{\frac{3}{2}}$ is the relevant conversion parameter at the interface [31]. Qualitatively, both predictions reproduce our data well, indicating that the interface conversion of the electron spin current to a magnonic current is the dominant process for the temperature dependence. However, the authors of Ref. [23] calculate that α changes from $\frac{5}{2}$ to $\frac{3}{2}$ from large to small distances. This cannot be verified by our data, since the fits suggest decreasing exponents α from the shortest to the largest distance, for both α_{low} and α_{high} . However, the low temperature behaviour for short distances ($\alpha_{\text{low}} \approx \frac{3}{2}$) reproduces the temperature dependence

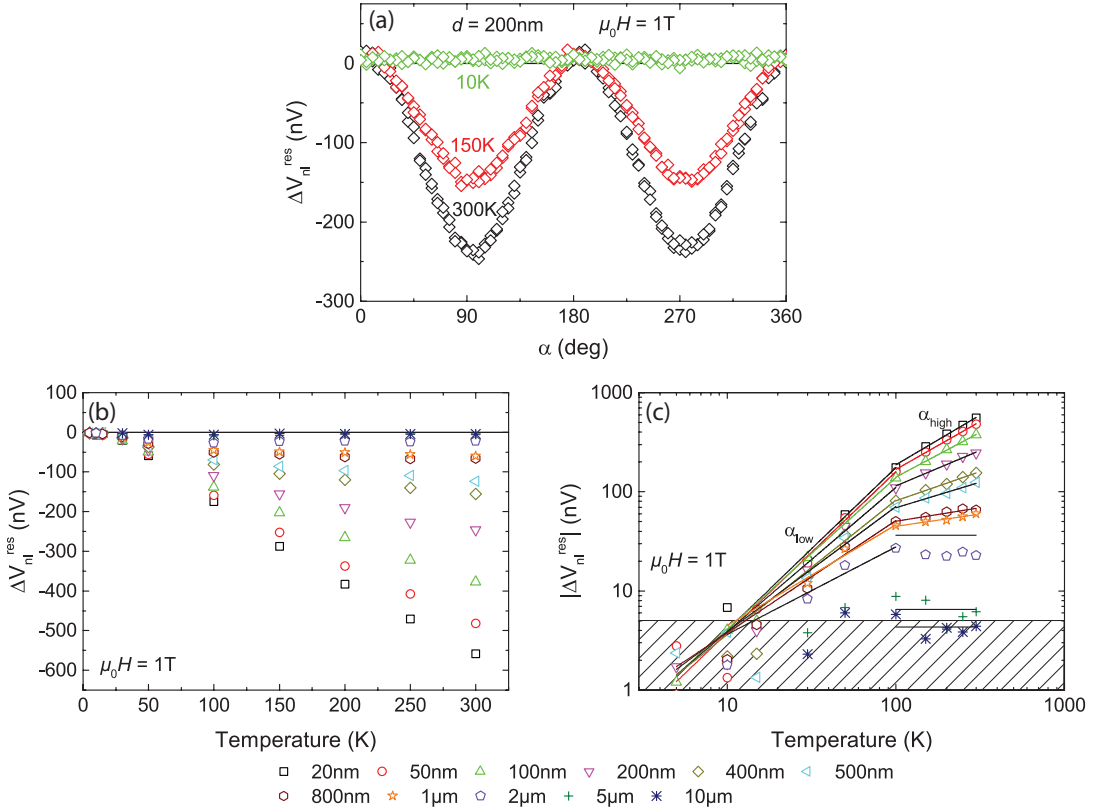


Figure 4.3: (a) Evolution of the non-local angle dependent MMR signal $\Delta V_{nl}^{\text{res}}$ for $T = 10 \text{ K}$, $T = 150 \text{ K}$ and $T = 300 \text{ K}$ on a device with $d = 200 \text{ nm}$ at a field strength of $\mu_0 H = 1 \text{ T}$. (b) Temperature dependence of $\Delta V_{nl}^{\text{res}}$ for different separation distances extracted from the ADMR measurements at $\mu_0 H = 1 \text{ T}$ on a linear scale. (d) Double logarithmic plot of the MMR temperature dependence. The solid lines correspond to power law fits and the shaded region represents the noise floor of our measurement setup.

of $g_s \propto \left(\frac{T}{T_C}\right)^{\frac{3}{2}}$. The quantitative disagreement for larger distances between theory and experiment is thereby not surprising, since the conversion efficiency g_s only takes into account temperature dependencies from the physics at the interface, which are governed by the Bose-Einstein-distribution function of magnons [23, 31]. As we will see in Sect. 4.1.3, the diffusion of magnons in the bulk of the YIG also exhibits a temperature dependence, which is parameterized by the magnon diffusion length λ_m , whose temperature dependence is attributed to the temperature dependent magnon relaxation times $\tau \propto \lambda_m$ [31, 42] and also to the bosonic distribution function (c.f. Appendix A). As a consequence, the increase of λ_m with decreasing temperature (see Sect. 4.1.3) counteracts the temperature dependence of the interface conversion efficiencies. The different contributions from the interface and the diffusion to the temperature evolution of the MMR will be discussed in detail in Sect. 4.1.3. Contrary to the low temperature regime below 100 K, for the high temperature regime $T \geq 100 \text{ K}$ we find a linear dependence ($\alpha_{\text{high}} \approx 1$) for short distances, which does not reproduce the temperature dependence of g_s . Instead, we can motivate a

linear dependence of the MMR at high temperatures by elaborating the relevant energy scales of the magnons responsible for the MMR signal as follows:

In the MMR picture [12], the SHE-induced electron spin accumulation μ_s is taken as the origin of the magnon excitation in YIG (c.f. Sect. 2.4). Consequently, due to energy conservation, this subtly suggests that the relevant energies of the diffusing magnons is in the order of the energy provided by μ_s , which is in the order of a few μeV or lower [31,43]. If this were true, however, magnons giving rise to the MMR should be excited even at very low temperatures, since the spin accumulation is still present there and the thermal smearing at 1 K still is in the order of $100 \mu\text{eV}$. This is not consistent with the vanishing MMR signal at low temperatures (below ~ 10 K, c.f. Fig. 4.3 (b)). Moreover, if the magnons responsible for the MMR signal dominantly had energies in the μeV -range, the signal should be already completely suppressed at a magnetic field $\mu_0 H = 1$ T, since this corresponds to a Zeeman energy $g\mu_B\mu_0 H \approx 0.1 \text{ meV} \gg \mu_s \approx 1 \mu\text{eV}$. This is again not consistent with the MMR signals shown in Fig. 4.3, since all of this data is obtained from measurements at $\mu_0 H = 1$ T. Furthermore, as we will see in the following sections, the strong impact of the thermal energy $k_B T$ on the MMR is a further indicator for the dominance of thermal magnons with energies close to $k_B T$. Therefore we here bluntly assume that the relevant magnon energies are those of thermally excited magnons, and not only magnon energies in the order of $\mu_s \sim \mu\text{eV}$. The thermal magnon energies can be represented by the mean energy $\bar{\epsilon}_{\text{mag}}$ of all thermally excited magnons, which we calculate as

$$\bar{\epsilon}_{\text{mag}} = \frac{1}{N_{\text{mag}}} \int_0^{\infty} d\epsilon \epsilon \mathcal{D}(\epsilon) f_{\text{BE}}(\epsilon, T) = \frac{3}{2} \frac{\zeta(\frac{5}{2})}{\zeta(\frac{3}{2})} k_B T \approx \frac{3}{4} k_B T, \quad (4.1)$$

where $N_{\text{mag}} = \int_0^{\infty} d\epsilon \mathcal{D}(\epsilon) f_{\text{BE}}(\epsilon, T)$ is the total number of excited magnons, $\mathcal{D}(\epsilon)$ the density of states for magnons with quadratic dispersion $\epsilon \propto k^2$ and $f_{\text{BE}}(\epsilon, T)$ the Bose-Einstein distribution function. In this picture, the energies of the non-equilibrium magnons themselves are governed by the thermal energy $k_B T$, whereas the energy difference between the thermal equilibrium (which corresponds to a magnon chemical potential $\mu_m = 0$) and the non-equilibrium state of magnons is parameterized by a finite μ_m , which must be in the order of the energy of the spin chemical potential μ_s (which is responsible for the non-equilibrium state of the magnon system [31]). However, independent of the exact microscopic excitation/annihilation process of magnons in the MMR, the dominance of magnons with energies up to $k_B T$ is considered throughout this thesis. With this assumption, the temperature dependence of the MMR at low temperatures ($T \leq 100$ K) is clear, since the number $N_{\text{mag}} \propto T^{\frac{3}{2}}$ of all thermally populated magnons (assuming a quadratic dispersion). Regarding the linear dependence observed above 100 K, we assume the dominance of the mean thermal magnon energy $\bar{\epsilon}_{\text{mag}} \propto T$ (c.f. Eq. 4.1). Although the magnitude of the energy of the participating magnons naively should not affect the MMR signal amplitude, it does affect the magnon to spin conversion efficiency $G_{\text{me}} \propto \bar{\epsilon}_{\text{mag}}$ (i.e. the magnon detection efficiency) calculated in Equation (12) of Ref. [23]. Assuming that at elevated temperatures $T > 100$ K the T dependence of the magnon detection efficiency $G_{\text{me}} \propto \bar{\epsilon}_{\text{mag}} \propto T$ dominates over the spin to magnon injection efficiency $G_{\text{em}} \propto T^{\frac{3}{2}}$ [23], the linear dependence above 100 K observed in Fig. 4.3 (c) for short distances (where the interface properties dominate) can be made at least plausible. The dominance of thermal

magnons in the MMR also provides an intuitive explanation for the vanishing MMR signal at low temperatures: at finite temperature, the YIG magnetization fluctuates due to thermally excited magnons. These fluctuations serve the energy for the electron spins at the interface to flip, and consequently excite (or annihilate) magnons. In the limiting case of $T \rightarrow 0$ the magnetization is stiff with practically no thermal magnons excited, leading to vanishing electron spin flip processes at low temperatures. Eventually we can motivate the linear temperature dependence observed for $T \geq 100$ K, if we assume that the relevant magnon energies responsible for the MMR are governed by the mean thermal magnon energy $\bar{\epsilon}_{\text{mag}} \propto T$ (Eq. 4.1). Note that in this picture one has to assume that the magnon to spin conversion efficiency G_{me} is suppressed below 100 K, since otherwise (due to $G_{\text{em}} \cdot G_{\text{me}}$) a $T^{\frac{5}{2}}$ dependence would be expected.

By comparing the local SMR and its non-local analogue, the MMR, we find a qualitatively different temperature dependence. We therefore conclude, that the physical origin of the non-local MMR is qualitatively different from its local analogue, the SMR.

4.1.2 Magnetic Field Dependence

The investigation of the magnetic field dependence of the SMR and MMR in YIG|Pt heterostructures opens the access to the understanding of the microscopic origins of these effects. Before we study the magnon transport properties under the influence of different magnetic fields and their interrelation with the MMR in Sect. 4.1.2.2, we start with the field dependence of the (local) SMR in Sect. 4.1.2.1.

4.1.2.1 Spin Hall Magnetoresistance

Figure 4.4 (a) shows the SMR modulations $\frac{V_{\text{loc}}^{\text{res}}}{V_0}$ for fields $\mu_0 H = 1$ T, 4 T and 7 T at $T = 300$ K. In panel (b) the SMR ratio $\frac{\Delta V_{\text{loc}}^{\text{res}}}{V_0}$ is plotted as a function of magnetic field. We find that the SMR is almost independent of magnetic field strength, which is corroborated by the theory of the SMR based on a macrospin model [20]. However, a slight SMR increase with increasing field is observable. This can be also seen in panel (c) of Fig. 4.4, where the SMR is plotted versus temperature for three different fields. The field-induced enhancement could be an indication that excitations of the magnetic system have an impact on the SMR, which requires a description of the SMR in terms of single spin dynamics, which is not covered by the present macrospin-based description [20]. The temperature-induced enhancement of the SMR at very low temperatures $T \lesssim 15$ K, which was already reported in Sect. 4.1.1, is more pronounced for high magnetic fields and also sets in at slightly higher temperatures. This feature could be explained if we assume the SMR to be enhanced when magnonic excitations are suppressed. In this case, at very low temperatures, where the magnon system is only sparsely populated, the magnetic field efficiently suppresses a large number of magnons relative to the total population, which results in a higher relative SMR enhancement at low T . Quantitatively, we can calculate the relative field enhancement of the SMR as

$$\frac{\Delta V_{\text{loc}}^{\text{res}}(B = 7 \text{ T}) - \Delta V_{\text{loc}}^{\text{res}}(B = 1 \text{ T})}{\Delta V_{\text{loc}}^{\text{res}}(B = 7 \text{ T})}. \quad (4.2)$$

Corresponding data are shown in Fig. 4.4 (d) for two different devices. Regarding the device with $d = 200$ nm and $w = 500$ nm (black dots in Fig. 4.4 (d)), the enhancement

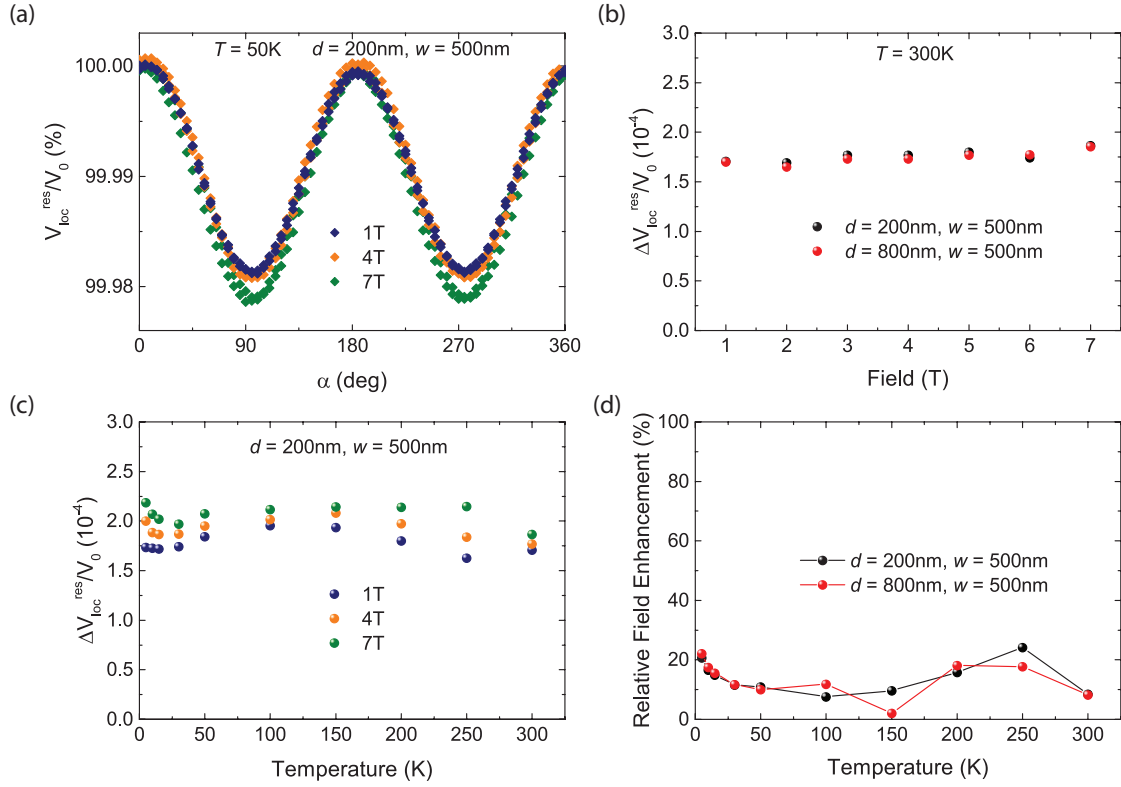


Figure 4.4: (a) ADMR measurements of the SMR at $\mu_0 H = 1\text{ T}$, 4 T and 7 T for a device with $d = 200\text{ nm}$ and $w = 500\text{ nm}$. (b) SMR ratio versus field at $T = 300\text{ K}$ for two different devices. (c) SMR signal extracted from fits to ADMR measurements plotted versus temperature for fields $\mu_0 H = 1\text{ T}$, 4 T and 7 T . (d) Relative field enhancement for two devices with $d = 200\text{ nm}$, $w = 500\text{ nm}$ and $d = 800\text{ nm}$, $w = 500\text{ nm}$ versus temperature calculated via Eq. 4.2.

is large (20%) for low temperatures, becomes lower at $T \sim 100\text{ K}$ ($\sim 8\%$) and seems to increase again up to $\sim 25\%$ at $T = 250\text{ K}$. For $T = 300\text{ K}$, however, the enhancement decreases again down to $\sim 8\%$. The device with $d = 800\text{ nm}$ and $w = 500\text{ nm}$ (red dots in Fig. 4.4 (d)) shows the same behaviour below $T = 50\text{ K}$, but fluctuates up and down by roughly 10% above 50 K ². Besides the decrease at 300 K , the black data points in Fig. 4.4 (d) ($d = 200\text{ nm}$, $w = 500\text{ nm}$) exhibit a qualitatively similar trend compared to the field suppression of the non-local MMR shown later in Fig. 4.5 (d). Since we will attribute the temperature dependent field suppression of the MMR to the mode spectrum of the magnons in YIG, the qualitative similar temperature dependent field enhancement of the SMR could be a further indicator for the influence of the magnon system in YIG on the SMR. Note, however, that the relative field enhancement shown in Fig. 4.4 (d), in particular the disagreement of the two measured devices above $T = 50\text{ K}$ (black and red dots) may also indicate that the experimental uncertainty increases above this temperature, such that the temperature behaviour of the relative field enhancement of the

²The almost vanishing enhancement at $T = 150\text{ K}$ for the device with $d = 800\text{ nm}$ and $w = 500\text{ nm}$ (red dots in Fig. 4.4 (d)) is likely to be an outlier and is therefore disregarded in the discussion.

SMR could be roughly assumed to be constant for $T > 50$ K. However, to be sure about this, more samples will have to be investigated. Ideally, an intentional modification of the magnon mode spectrum in situ and a measurement of the corresponding changes in SMR and MMR would be required to resolve this question.

4.1.2.2 Magnon Mediated Magnetoresistance

To gain insight into the transport properties of electrically injected magnons, we now turn to the field dependence of the MMR. To this end, angle dependent magnetoresistance (ADMR, *c.f.* Sect. 3.3) measurements at different magnetic fields up to 7 T were conducted. Figure 4.5 (a) shows a non-local ADMR signal with $d = 100$ nm for three different fields $\mu_0 H = 1$ T, 4 T and 7 T at $T = 300$ K. Qualitatively, the MMR signal is suppressed by an increase of the external field [44]. This can be understood intuitively, since a higher external field leads to a stiffer magnetization in the YIG, which in turn hinders spin waves to propagate. More rigorously, the external field creates an energy gap in the magnon dispersion relation, shifting the magnon dispersion relation to higher energies, such that magnons with high \mathbf{k} -vectors are no longer thermally occupied. Additionally, due to the shift of the dispersion relation, magnons with energy $g\mu_B B$ are suppressed, making low energy magnons inaccessible for the excitation [44]. Note, that this corresponds not only to a suppression of magnons with low energy (frequency), but to a pronounced suppression of magnons with small \mathbf{k} -vectors as well, since the Bose-Einstein distribution function of magnons is cut off at a lower limit by the spin wave gap (Zeeman energy) $g\mu_B B$. Therefore, small wavevectors \mathbf{k} in the magnon dispersion are less occupied due to the shift to higher energies when $\mu_0 H > 0$.

In order to obtain a direct measure of the MMR signal evolution with magnetic field strength, field sweeps up to 15 T for temperatures from 10 K to 300 K were conducted on the non-local structures for strip separations $d = 20$ nm to $d = 2$ μ m. To ensure a maximum magnon generation, the magnetic field is applied perpendicular to the Pt strips. Figure 4.5 (b) shows field sweeps from -15 T to 15 T for temperatures 10 K $< T < 300$ K for a device with $d = 100$ nm. In Figure 4.5 (c), the MMR amplitude extracted from Fig. 4.5 (b) is plotted as a function of temperature for different fields. For a quantitative analysis of the suppression we determine the relative field suppression of the MMR as

$$\frac{\Delta V_{\text{nl}}^{\text{res}}(B = 0 \text{ T}) - \Delta V_{\text{nl}}^{\text{res}}(B = 15 \text{ T})}{\Delta V_{\text{nl}}^{\text{res}}(B = 0 \text{ T})}, \quad (4.3)$$

where 100 % corresponds to complete suppression. The result is depicted in Fig. 4.5 (d) as a function of temperature for different strip separations d . Note that only pairs of strips yielding a reasonable signal to noise ratio could be analyzed and are shown here, such that only a subset of all samples made can be compared.

Nonetheless the qualitative trend of the field suppression is clear: it reaches a maximum for room temperature, is also large for low temperatures $T = 50$ K³, and goes through a minimum in between. For the largest shown distance of $d = 1$ μ m, however, a monotonous increase of the field suppression with increasing temperature is observed, reaching values above 100 % at $T = 250$ K and $T = 300$ K. This particular behaviour for $d = 1$ μ m will

³The suppression could not be calculated reliably for temperatures below 50 K, since the signal becomes very low at these temperatures

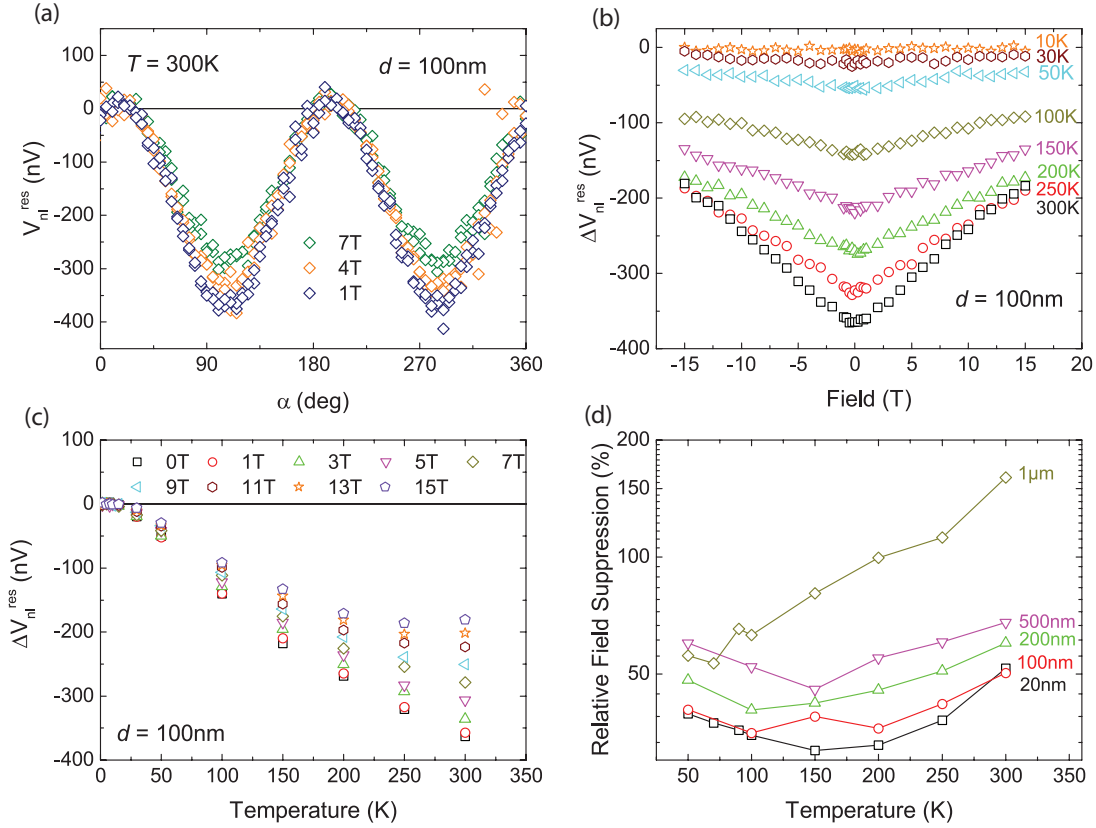


Figure 4.5: (a) ADMR measurements at $\mu_0 H = 1\text{ T}$, 4 T and 7 T for a device with $d = 100\text{ nm}$. (b) Magnetic field sweeps for the same device as in (a) for $10\text{ K} < T < 300\text{ K}$. (c) MMR signal extracted from field sweeps plotted versus temperature for fields up to 15 T . (d) Relative MMR field suppression for several strip separations versus temperature calculated via Eq. 4.3.

be analyzed in more detail at the end of Sect. 4.1.3. For the following discussion, only distances up to $d = 500\text{ nm}$ are considered, where the temperature evolution of the relative MMR field suppression is similar.

The high field suppression of the MMR at low temperatures can be attributed to the effect of the field-induced spin wave gap of the magnon dispersion on the interface spin current j_s^{int} , as described in Ref. [45] for the Spin Seebeck Effect (SSE). Although the SSE is a thermally driven effect, both the SSE and MMR are based on magnon spin currents j_s^{int} across the YIG/Pt interface, making the comparison reasonable [14, 31]. In Equation (8) of Ref. [31] the interface spin current j_s^{int} of the MMR, which is proportional to V_{nl}^{res} , reads

$$V_{nl}^{\text{res}} \propto \int_{g\mu_B B}^{\infty} d\epsilon (\epsilon - \mu_s) \mathcal{D}(\epsilon, B) \left(f_{\text{BE}} \left(\frac{\epsilon - \mu_m}{k_B T_m} \right) - f_{\text{BE}} \left(\frac{\epsilon - \mu_s}{k_B T_e} \right) \right) \quad (4.4)$$

where μ_B is the Bohr magneton, g the g-factor ($= 2.00$ for YIG [45]), B the external field and $\mathcal{D}(\epsilon, B)$ the density of states of magnons in YIG. Furthermore there are the Bose-

Einstein distribution functions $f_{\text{BE}}\left(\frac{\epsilon - \mu_{\text{m}}}{k_{\text{B}}T_{\text{m}}}\right)$ and $f_{\text{BE}}\left(\frac{\epsilon - \mu_{\text{s}}}{k_{\text{B}}T_{\text{e}}}\right)$ with the magnon temperature T_{m} in YIG and the electron temperature T_{e} in Pt. The magnon chemical potential μ_{m} and the electron spin chemical potential $\mu_{\text{s}} = \mu_{\uparrow} - \mu_{\downarrow}$ parameterize the non-equilibrium spin and magnon accumulations in the YIG and the Pt, respectively [31, 46, 47]. Since magnons are bosonic quasiparticles which are not particle number conserving, the chemical potential should be zero⁴. However, the non-equilibrium magnons which are excited in the context of the MMR can be treated as number conserving particles, if one assumes that non-number conserving scattering times (like magnon-annihilating magnon-phonon interactions with characteristic time constant τ_{mr} [31]) are much larger than magnon-conserving scattering times (like magnon-magnon and magnon-conserving magnon-phonon interactions with τ_{mm} and τ_{mp} , respectively [31, 47]), which leads to the definition of a magnon chemical potential μ_{m} [31, 47]. At this point it is important to emphasize that the assumption of solely magnon conserving scattering events is not sufficient for a steady state diffusion process, as described in Eq. 2.10 in Sect. 2.4. This is because the injector current is continuously generating non-equilibrium magnons, which cannot be dissipated when no magnon-annihilating scattering events are considered. This is covered by the theory of Ref. [31], where the time scale τ_{mr} parameterizes the magnon dissipation into the phonon bath, which is roughly given by $\tau_{\text{mr}} \sim \frac{\hbar}{\alpha_{\text{G}}k_{\text{B}}T}$ with α_{G} the Gilbert damping parameter. The strong field-induced MMR suppression at low temperatures can be understood in the context of a simple quadratic magnon dispersion $\epsilon \propto k^2 + \Delta$, where $\Delta \propto B$ is the spin wave gap induced by the external magnetic field B . At low temperatures around $T = 50$ K, the thermal energy $k_{\text{B}} \cdot 50 \text{ K} \approx 4 \text{ meV}$. This corresponds to thermally populated magnons up to small wavevectors \mathbf{k} , which can be partly suppressed by the Zeeman gap $g\mu_{\text{B}} \cdot 15 \text{ T} \approx 1.7 \text{ meV}$ (c.f. Fig. 4.7 (c)). The field suppression calculated with Eq. 4.3 for the device with $d = 20 \text{ nm}$ at $T = 50 \text{ K}$ yields a suppression of $\sim 39\%$, which agrees approximately with $\frac{g\mu_{\text{B}} \cdot 15 \text{ T}}{k_{\text{B}} \cdot 50 \text{ K}} \approx 40\%$. Note, that this estimation only takes into account effects from the magnon population, which are related to the generation/annihilation of magnons at the interface. The magnon diffusion process is not covered by this estimate, which is why the calculated and measured field suppression values only agree for a very short strip distance of 20 nm , since here the diffusion process is not dominant (c.f. Sect. 4.1.3).

The increase of field suppression observed at high temperatures, however, is not covered by this approach. Therefore, we extend the qualitative model for high temperatures by taking into account the population of a higher magnon mode near room temperature. The lowest magnon mode in YIG, as well as the next higher optical mode can be quite well identified by simple parabolic band dispersions, at least for small values of the wave vector \mathbf{k} [48–50]. The magnon dispersion in YIG, calculated by Joseph Barker and Gerrit E.W. Bauer in Ref. [48], are shown for different temperatures from 1 K to 300 K in Fig. 4.6.

The blue and red color denotes the positive/negative (+/−) chirality of the modes, of which the corresponding magnon excitations carry an angular momentum $\pm\hbar$, respectively⁵. For high temperatures (at 300 K) only the fundamental acoustic mode and the first optical mode are relevant, since all other branches become highly incoherent and ex-

⁴In thermodynamics, the chemical potential can be written as the derivative of the free energy with respect to the particle number N : $\mu = \frac{\partial \mathcal{F}}{\partial N}$. For systems with non-conserved particle number the derivative will be always zero, since the system will always assume the state of minimal energy.

⁵ $+\hbar$ corresponds to a magnon with polarization pointing against the net magnetization, while $-\hbar$ corresponds to a moment parallel to the net magnetization.

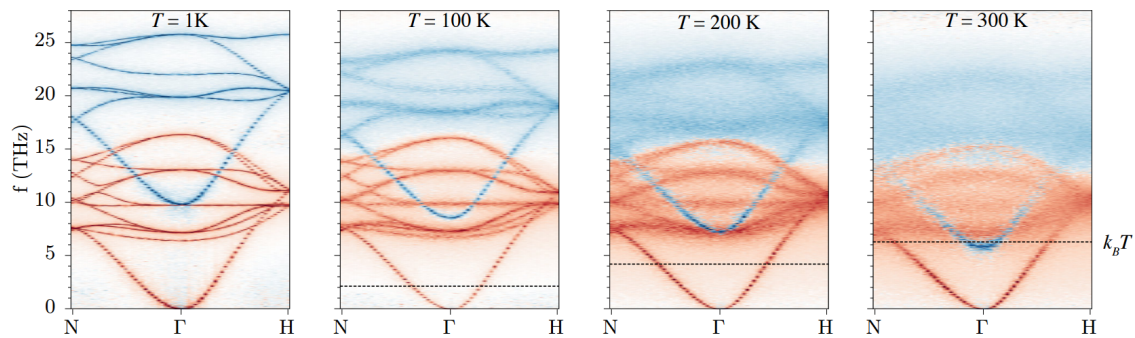


Figure 4.6: YIG magnon dispersion calculated for different temperatures by J. Barker and G.E.W. Bauer in Ref. [48]. The red and blue coloring denotes the $+/-$ chirality of the modes, corresponding to different polarizations of the magnons in our notation. The dashed lines mark the position of the thermal energy $k_B T$ in the frequency spectrum. Note that the parabolic blue optical mode shifts down in frequency when the temperature increases. Figure taken from [48].

hibit large linewidths [48]. With decreasing temperature the optical mode (blue) shifts to higher frequencies because the gap Δ between the modes depends on the exchange coupling between the iron sublattices in YIG, which is increasing due to decreasing thermal fluctuations [48]. It is also evident from Fig. 4.6, that the optical mode becomes thermally populated at high temperatures. Moreover, by applying an external field B , the acoustic fundamental mode shifts upwards in energy linearly with field (provided that we simply add a Zeeman energy $g\mu_B B$ to the dispersions). The optical mode, however, shifts downwards by $g\mu_B B$ in the frequency spectrum [51]. This can be made clear easily if we recall the ferrimagnetic properties of YIG. In a simple picture, the optical mode can be attributed to the antiferromagnetically coupled iron sublattice magnetization \mathbf{M}_{Fe}^a (c.f. Chap. 3) which is oriented antiparallel to the external field. As a consequence, the Zeeman energy $g\mu_B B$ has to be subtracted from the optical magnon dispersion, since the increasing magnetic field decreases the \mathbf{M}_{Fe}^a magnetization.

With the help of these features of the YIG-dispersion, we can give a qualitative explanation of the MMR field suppression at high T observed in Fig. 4.5 (d), as illustrated in Fig. 4.7 (a) to (c). On the left hand side of Fig. 4.7 (a) the two magnon modes are depicted schematically as quadratic dispersions $E(k)$ on different energy levels, with no external field B applied. The thermal energy $k_B T$ at room temperature is sufficient to populate the high energy optical mode only up to small wave vectors \mathbf{k} (according to Refs. [48, 50, 52], for $T \lesssim 260$ K only the lower branch is occupied). On the right hand side, an externally applied field B leads to an upwards shifting of the fundamental acoustic mode by the Zeeman energy $g\mu_B B$, while the optical mode is downshifted by the Zeeman energy. This results in an enhanced population of magnons of the optical mode (blue color), while additionally low frequency magnons of the acoustic mode are suppressed (red color). This eventually gives rise to a strong field suppression, since the field-induced population of the optical mode leads to a lowering of the MMR signal because of the opposing chirality of the optical mode with respect to the acoustic mode (the acoustic and optical magnons "cancel" one another in terms of the ISHE detection). As a consequence, the counter-acting generation of MMR signal by optical magnons at high field lowers the measured

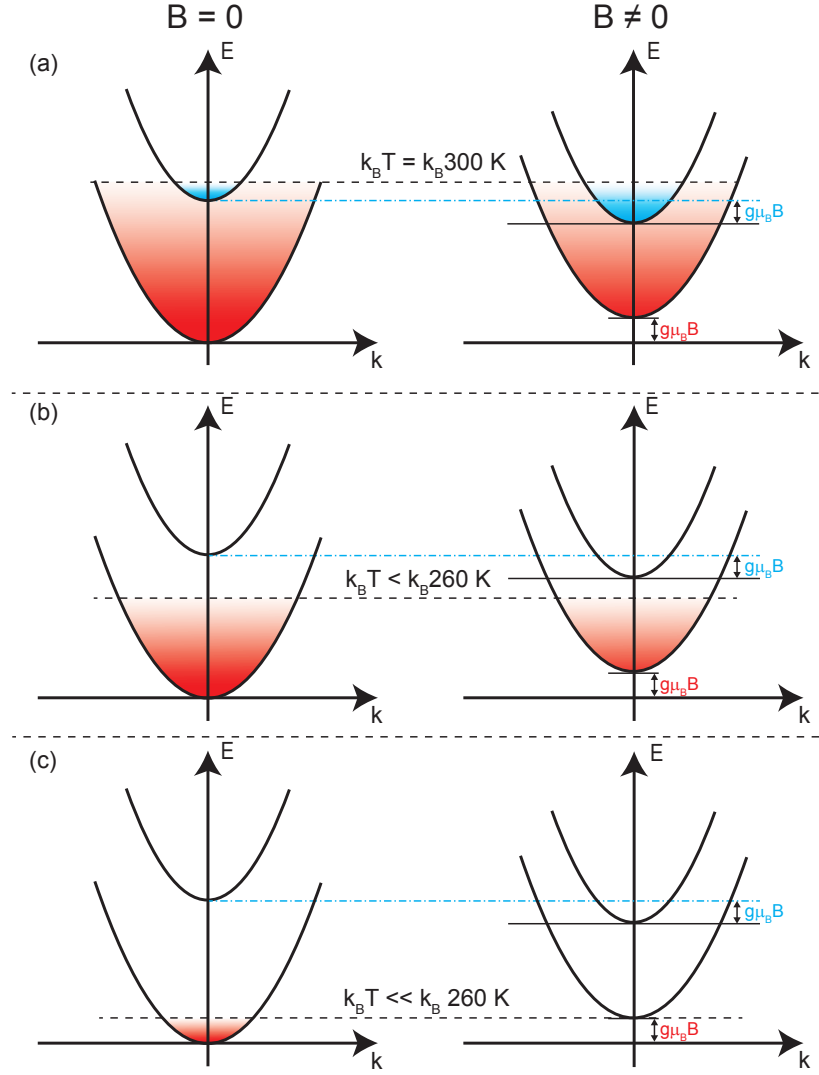


Figure 4.7: Schematics of the parabolic acoustic fundamental mode and the high energy optical mode. Red and blue coloring represents positive and negative (+/-) chirality of the magnon modes, respectively. The left column shows the case for a vanishing external magnetic field of $B = 0$, whereas the right one depicts the case for a finite magnetic field $B > 0$. (a) The magnon spectrum is populated up to a thermal energy of $k_B \cdot 300 \text{ K}$, where even the optical mode is partially populated [48, 50]. When the external field is switched on, the optical mode shifts down by the Zeeman energy $g\mu_B B$. This leads to a larger thermal population of the oppositely polarized optical magnons with respect to the acoustic polarization, giving rise to a large suppression at high temperatures due to the counteracting ISHE signal generation of the optical mode. Additionally, low frequency magnons of the fundamental mode are suppressed, further increasing the MMR suppression. (b) Below 260 K for $B = 0$ the optical mode is depopulated, but the fundamental acoustic mode is still populated up to large values of k . By switching on the magnetic field, only magnons of large k are suppressed around $k_B T$, which has a less pronounced influence on the MMR signal. (c) At temperatures below $T \approx 50 \text{ K}$, only a small amount of low frequency magnons is populated in the fundamental mode. An additional field induced Zeeman energy efficiently suppresses these states.

MMR signal. Note, that in Refs. [45, 53] the dominance of low frequency magnons for the SSE is proposed (see Sect. 4.2.2.3), which further corroborates the enhanced field suppression at high temperatures, since we additionally suppress low-frequency magnons by shifting up the fundamental mode with field. As discussed beforehand, this is reasonable, since the suppression of low frequency magnons corresponds also to a depopulation of wavevectors with small \mathbf{k} , since the Zeeman energy cuts off the Bose-Einstein distribution at small energies. The left hand side of Fig. 4.7 (b) illustrates the picture for intermediate temperatures $k_B T < 260$ K at $B = 0$. Here, the acoustic mode is populated up to high wavevectors, while the optical mode is not thermally populated at all. An applied magnetic field B (right hand side of Fig. 4.7 (b)) shifts the acoustic mode upwards. The field-induced downshift of the optical mode however is not sufficient to induce its population. As observed in experiment, the field suppression is lower in this temperature regime, which is explained by the fact that only magnons with large values of \mathbf{k} can be suppressed around $k_B T$. This is reasonable, since the thermal population at these energies (wavevectors) is low due to the Bose-Einstein distribution. Note further that the magnon scattering rates $\tau \propto \frac{1}{k^\alpha}$ (α depends on the interaction with phonons, magnons etc. [31, 54]), such that only magnons with small values of \mathbf{k} or large wavelengths λ should be dominantly responsible for the non-local signal. The finite suppression in this regime is still above 30% for $d = 20$ nm, indicating the dominance of low frequency magnons, that are always suppressed in the fundamental mode [42, 45, 53]⁶. For very low temperatures only a small amount of magnons with low \mathbf{k} in the energy momentum space is populated, as depicted in Fig. 4.7 (c). The dispersion up-shifting by the external field then efficiently depopulates these magnons, giving rise to the previously observed strong field suppression at low temperatures (c.f. Fig. 4.5 (d)). Eventually, by taking into account the optical magnon branch with different chirality, one can understand the strong field suppression at high and low temperatures, as well as the less pronounced suppression at intermediate temperatures.

⁶In Ref. [42] the dominance of low frequency magnons is theoretically calculated and attributed to the phonon-mediated magnon-magnon scattering, which is found to be very small for low energy (subthermal) magnons, while larger for higher magnon energies.

In the "one acoustic, one optical" model, the optical mode generates an ISHE signal that is opposite in sign compared to the one generated by the acoustic mode, due to the different chirality (and thus "spin orientation") of the modes. Therefore the model predicts that the signal should be inverted at high temperatures and high magnetic fields, where the optical mode is shifted to low frequencies and starts to dominate the MMR. A temperature increase strongly affects the magnon population, since the optical mode is shifting down in frequency with increasing temperature (see Fig. 4.6 [48]), while the thermal energy $k_B T$ is increasing, giving rise to a strong population of the optical mode. Furthermore, this effect should be more pronounced at large distances d . This is explained by the suppression of magnons with small wavevectors \mathbf{k} of the fundamental mode, which exhibit large lifetimes $\tau \propto \frac{1}{k^\alpha}$ [54]. This suppression is present for all temperatures, since the Bose-Einstein distribution is always cut off by the Zeeman energy, reducing the populated states at low \mathbf{k} . The reduction of magnons with small wavevectors in the fundamental mode leads to a decrease in the overall magnon diffusion length $\lambda_m \propto \tau$. For the optical mode, however, a high magnetic field shifts the mode to lower energies, such that even more magnons with small \mathbf{k} are thermally occupied, which increases the diffusion length of this mode due to $\tau \propto \frac{1}{k^\alpha}$ [31, 54]. Consequently, at large distances, high temperatures as well as large magnetic fields the conditions are such that the optical magnons are dominant due to their increasing population (induced by high temperatures and high magnetic fields) and enhanced diffusion length (induced by the population of small \mathbf{k} -vectors) combined with the lowered population and lowered diffusion length of the fundamental mode (induced by high magnetic fields and the accompanying suppression of small \mathbf{k} -vectors). Eventually at large distances and high temperatures the conditions are such, that high magnetic fields are sufficient to invert the MMR signal by the influence of the optical mode. This effect can indeed be observed in the field sweep data for a device with $d = 1 \mu\text{m}$ in Fig. 4.8, where the MMR is inverted at $B = 13 \text{ T}$ and $B = 6 \text{ T}$ for $T = 250 \text{ K}$ and 300 K , respectively. Note that the signals for this device exhibit a positive offset of approximately 15 nV , which remains at low temperatures of 5 K in Fig. 4.8, where the MMR signal is expected to vanish (see Sect. 4.1.1). We attribute this offset to a finite crosstalk between the strips caused by surface contaminations or moisture between strips (see Appendix B). Assuming that this offset is temperature independent, the MMR indeed inverts its sign at high fields. To make sure that the MMR sign inversion is not due to a temperature dependent offset, ADMR measurements for a device with $d = 1 \mu\text{m}$ up to an external field $\mu_0 H = 15 \text{ T}$ need to be carried out in the near future. A further strong support for our model is the temperature behaviour of the signal at low magnetic fields. Here,

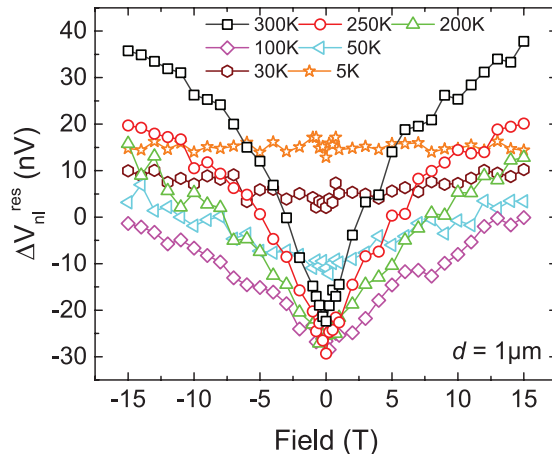


Figure 4.8: MMR signal $\Delta V_{ni}^{\text{res}}$ measured as a function of magnetic field for a device with $d = 1 \mu\text{m}$. For high temperatures at $T = 250 \text{ K}$ and $T = 300 \text{ K}$ the signal is inverted at high magnetic fields.

For high temperatures at $T = 250 \text{ K}$ and $T = 300 \text{ K}$ the signal is inverted at high magnetic fields.

the signal is lower for 300 K than for 250 K, which indicates the downshift of the optical mode with increasing temperature [48], still assuming a temperature independent offset. As a consequence thereof, the astonishing suppression above 100 % for $d = 1 \mu\text{m}$ at high temperatures shown in Fig. 4.5 (d) is due to a sign change of the signal and can be explained by the large population of the optical magnon mode at high temperatures and high magnetic fields.

Up to here, we only discussed the field suppression and temperature dependence (see Sect. 4.1.1) of the MMR in terms of the YIG|Pt interface, i.e. the generation of a non-equilibrium magnon population in the YIG, which is directly related to the excitation spectrum of magnons. However, the field suppression must also be partly attributed to the transport mechanism of magnons across the strip separation, since we find that the (relative) suppression is stronger for larger distances (see Fig. 4.5 (d)). This indicates that the suppression has to be linked to the magnon transport as well, since a field suppression for the injection or detection process would not lead to a distance dependent suppression [44]. The magnetic field as well as temperature dependence of the diffusive transport will be discussed in detail in Sect. 4.1.3.

4.1.3 Distance Dependence

Last but not least the strip separation dependence (distance dependence) of the MMR signal is examined in the following. As discussed in Sect. 2.4, the MMR is described as a diffusion of non-equilibrium magnons [12, 23, 31]. Since the magnon population decays with propagation distance, the MMR signal is distance dependent. Hence, for an in-depth understanding of the diffusive transport it is inevitable to investigate the MMR signal as a function of distance. Figure 4.9 (a) depicts ADMR measurements of the MMR for three different distances $d = 50 \text{ nm}$, 500 nm and $1 \mu\text{m}$ at $T = 300 \text{ K}$ for an external field $\mu_0 H = 1 \text{ T}$. As expected for a diffusive process, the signal decreases with increasing injector-detector distances. Figure 4.9 (b) depicts the signal amplitude versus the strip separations for temperatures ranging from $T = 10 \text{ K}$ to $T = 300 \text{ K}$ on a linear scale, where the data is only shown for distances up to $d = 2 \mu\text{m}$, for reasons of clarity.

The authors of Ref. [12] put forward a simple classical 1D diffusion model for the magnon transport, resulting in a fit function $\Delta V_{\text{nl}}^{\text{res}} = \frac{C}{\lambda_m} \frac{\exp\left(\frac{d}{\lambda_m}\right)}{1 - \exp\left(\frac{2d}{\lambda_m}\right)}$ with λ_m the magnon diffusion length in YIG and C a distance independent prefactor [12]. However, this function does not fit our data well⁷. Instead, we use a simple exponential decay of the form

$$\Delta V_{\text{nl}}^{\text{res}} = V_{\text{nl}}^0 \exp\left(-\frac{d}{\lambda_m}\right) \quad (4.5)$$

with the prefactor V_{nl}^0 and magnon diffusion length λ_m , which matches the data well in the short distance regime up to $\sim 500 \text{ nm}$. In the following, we separately investigate the temperature dependencies of the fit parameters V_{nl}^0 and λ_m of Eq. 4.5. With this, we are able to distinguish between interface-related effects of the temperature dependence

⁷It is very likely that the authors of Ref. [12] focus on a different distance/transport regime, since their 1D diffusion model is applied for distances $d \approx 40 \mu\text{m} > 1 \mu\text{m}$. However, in our measurements the signal drops below our noise floor of 5 nV around $5 \mu\text{m} < d < 10 \mu\text{m}$, such that the data analysis above this lengthscale is no longer reliable.

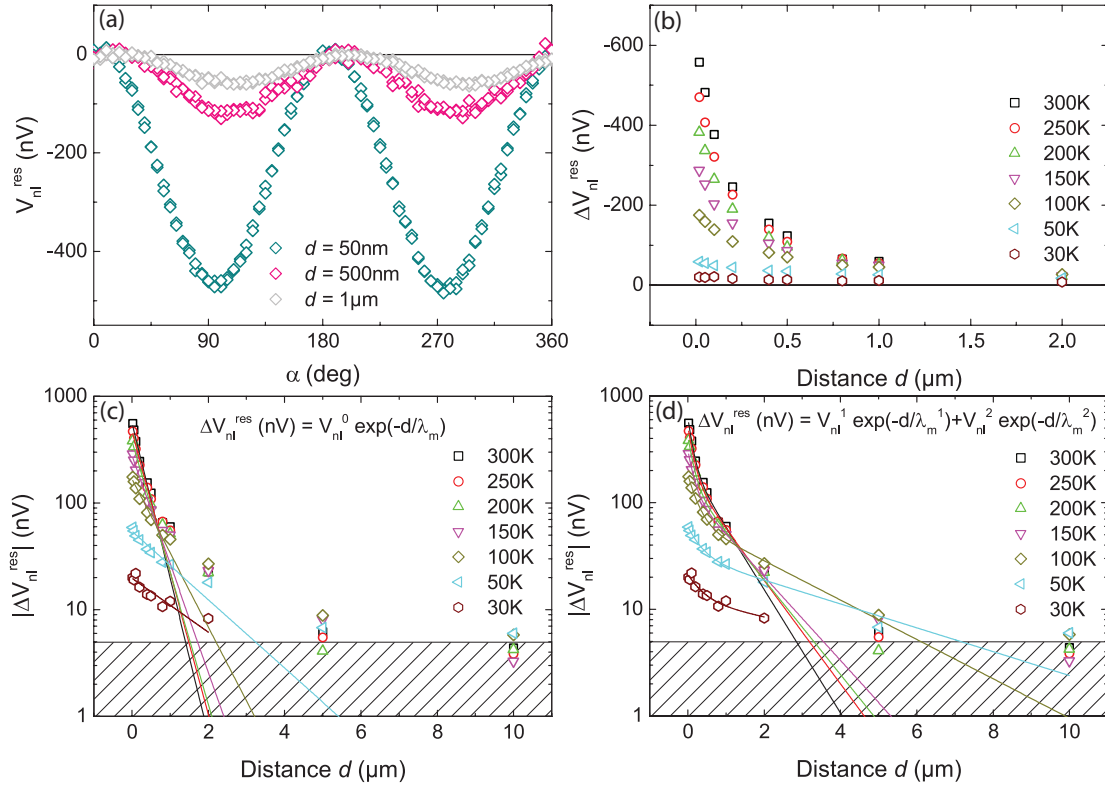


Figure 4.9: (a) MMR signal as a function of the in plane magnetic field orientation α for distances $d = 50\text{ nm}$, 500 nm and $1\text{ }\mu\text{m}$ at $T = 300\text{ K}$ for an external field $\mu_0 H = 1\text{ T}$. (b) Distance dependence of $\Delta V_{nl}^{\text{res}}$ for different temperatures on a linear scale. (c) Logarithmic plot of $\Delta V_{nl}^{\text{res}}$ versus distance with exponential decay fits using Eq. 4.5. (d) Same as (c) with fits using Eq. 4.7 with decay lengths λ_m^1 and λ_m^2 .

(as for instance the spin to magnon and magnon to spin conversion efficiencies discussed in Sect. 4.1.1 [23]), which we attribute to the prefactor V_{nl}^0 , as well as the temperature dependencies arising from magnon diffusion, parameterized by λ_m .

At first, we focus on the temperature dependence of V_{nl}^0 . In Fig. 4.10 (a) the prefactor V_{nl}^0 extracted from Fig. 4.9 (c) for temperatures ranging from $10\text{ K} < T < 300\text{ K}$ is shown in a double logarithmic plot. In contrast to the MMR temperature dependence shown in Fig. 4.3 (b) of Sect. 4.1.1, the temperature behaviour of the prefactor V_{nl}^0 is completely independent of the distance between strips. The solid lines correspond to power law fits $A \cdot T^\alpha$ with fit parameters A and α . This fit function is then separately applied to Fig. 4.10 (a) for the low temperature regime up to 100 K with exponent $\alpha_{0,\text{low}}$, and to the high temperature regime above 100 K with exponent $\alpha_{0,\text{high}}$. For the low temperature regime below 100 K , $\alpha_{0,\text{low}} = 1.7$, which approximately coincides with the predicted $\alpha = \frac{3}{2}$ of the MMR spin conductance $g_s \propto T^{\frac{3}{2}}$ from Ref. [31]. For higher temperatures above 100 K , however, $\alpha_{0,\text{high}} = 1.1$, which suggests a linear behaviour. As discussed in Sect. 4.1.1, a linear MMR temperature dependence could be motivated by the linear T -dependence of the average magnon energy $\bar{\epsilon}_{\text{mag}} \approx \frac{3}{4}k_B T$ (c.f. Eq. 4.1), which is the origin of the T -dependence of the magnon to spin conversion efficiency $G_{\text{me}} \propto \bar{\epsilon}_{\text{mag}}$ calculated in Eq. (12)

of Ref. [23]. In order to obtain a consistent picture in line with our observations, however, one must assume that the injection efficiency of magnons (parameterized by $G_{\text{em}} \propto T^{\frac{3}{2}}$ in Ref. [23]) is dominant for low temperatures below 100 K, while above 100 K the detection efficiency $G_{\text{me}} \propto T$ prevails. Still, it should be kept in mind that the calculations in Ref. [23] are based on a purely quadratic magnon dispersion. However, this is only true for low temperatures up to ~ 50 K (c.f. Fig. 4.6) [48]. At higher temperatures up to ~ 300 K, the fundamental acoustic dispersion is more accurately described by a linear evolution [48]. Therefore, the theory should be modified with a more accurate functional dependence of the YIG dispersion.

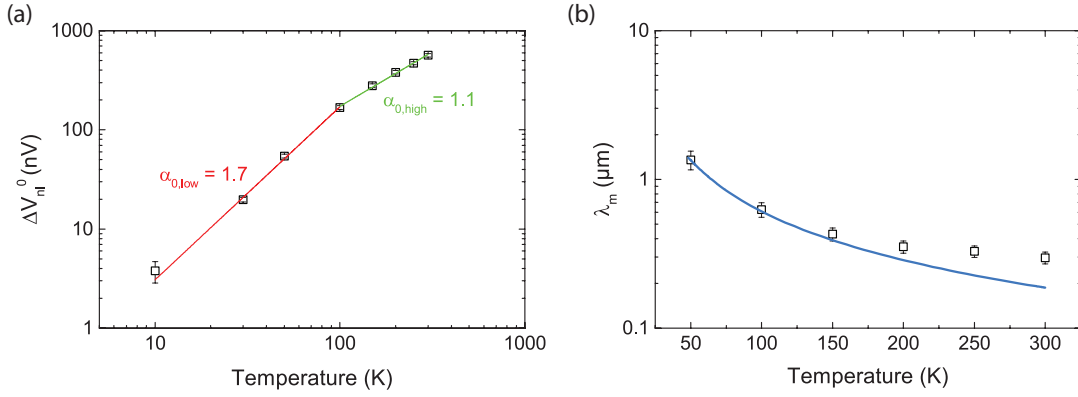


Figure 4.10: Fit parameters of Eq. 4.5 fitted to the data in Fig. 4.9 (c). (a) Prefactor V_{nl}^0 versus temperature, where the solid lines correspond to power law fits $A \cdot T^\alpha$. (b) Magnon diffusion length λ_m versus temperature. The solid blue line corresponds to a theoretical calculation based on Eq. 4.6 (see Appendix A for details).

To account for the temperature dependent diffusion process of magnons, the magnon diffusion length λ_m , extracted from fitting Eq. 4.5 to Fig. 4.9 (c), is now investigated as a function of temperature. This is shown in Fig. 4.10 (b). The solid blue line corresponds to a theoretical calculation based on Eq. 4.6, which reproduces the data well for low temperatures (see Appendix A for details). Qualitatively, we observe an increase in the magnon diffusion length λ_m with decreasing temperature. In order to understand this behaviour, it is important to point out the microscopic origin of λ_m . Since we assume a diffusive transport of thermal magnons with all populated wavevectors \mathbf{k} , λ_m is represented by a statistical average

$$\lambda_m = \frac{1}{N_{\text{mag}}} \int_0^\infty d\mathbf{k} \lambda_{\mathbf{k}} \mathcal{Z}(\mathbf{k}) f_{\text{BE}}(\mathbf{k}, T), \quad (4.6)$$

where $N_{\text{mag}} = \int_0^\infty d\mathbf{k} \mathcal{Z}(\mathbf{k}) f_{\text{BE}}(\mathbf{k}, T)$ is the total number of excited magnons at temperature T , $\mathcal{Z}(\mathbf{k}) = \frac{V}{(2\pi)^3}$ the density of states in \mathbf{k} -space and $f_{\text{BE}}(\mathbf{k}, T)$ the Bose-Einstein distribution function. The integration takes place over all microscopic magnon scattering lengths $\lambda_{\mathbf{k}} = v_{\mathbf{k}} \tau_{\mathbf{k}}$ with the magnon group velocity $v_{\mathbf{k}} = \frac{1}{\hbar} \frac{\partial \epsilon}{\partial \mathbf{k}} \propto \mathbf{k}$ for a quadratic magnon dispersion $\epsilon \propto \mathbf{k}^2$. At first glance, $\lambda_{\mathbf{k}}$ is expected to increase with increasing \mathbf{k} -values, since the magnon group velocity $v_{\mathbf{k}} \propto \mathbf{k}$. However, the wavevector-dependent scattering times $\tau \propto \frac{1}{k^\alpha}$ with $\alpha \approx 2$ [50] for magnon-phonon scattering or even $\alpha \approx 6$ for

magnon-magnon scattering at room temperature [31]. Therefore the magnon scattering times $\lambda_{\mathbf{k}}$ can be assumed to be small at large \mathbf{k} . With these conditions in mind, the qualitative temperature dependence of $\lambda_{\mathbf{m}}$ can be explained intuitively as follows: at high temperature, magnons are thermally populated up to large wavevectors \mathbf{k} . The statistical average based on Eq. 4.6 for $\lambda_{\mathbf{m}}$ therefore has to be taken over all populated states, including the states at high \mathbf{k} with small scattering lengths $\lambda_{\mathbf{k}}$, making the average value $\lambda_{\mathbf{m}}$ small. At low temperatures, however, many states with large \mathbf{k} are unoccupied. Therefore the resulting $\lambda_{\mathbf{m}}$ (Eq. 4.6) is on average larger than for the high temperature case. Note that this explanation is purely based on occupation statistics and \mathbf{k} -dependent scattering times. However, the magnon-magnon as well as magnon-phonon scattering times τ_{mm} and τ_{mp} are additionally inversely proportional to different powers of temperature T [31,50], which further corroborates the increase of $\lambda_{\mathbf{m}}$ with decreasing temperature.

While this simple diffusive model describes the experimental data well in the short distance regime, it does not match the behaviour for $d > 500$ nm (see Fig. 4.9 (c)). We therefore use a superposition of exponential decay functions with two different diffusion lengths λ_{m}^1 and λ_{m}^2 and prefactors V_{nl}^1 and V_{nl}^2

$$\Delta V_{\text{nl}}^{\text{res}} = V_{\text{nl}}^1 \exp\left(-\frac{d}{\lambda_{\text{m}}^1}\right) + V_{\text{nl}}^2 \exp\left(-\frac{d}{\lambda_{\text{m}}^2}\right) \quad (4.7)$$

for the short and large distance regime, respectively. Equation 4.7 is fitted to the distance dependent data in Fig. 4.9 (d), which yields a slightly better agreement with the experimental data at large distances. As done before we separately extract the prefactors and the diffusion lengths of Eq. 4.7, in order to distinguish between interface- and transport-related temperature dependencies, respectively. The temperature dependence of the prefactors V_{nl}^1 and V_{nl}^2 is shown in Fig. 4.11 (a), where the solid lines correspond to power law fits $A \cdot T^\alpha$, which are separately applied to the low ($T \leq 100$ K) and high temperature ($T \geq 100$ K) regime.

For low temperatures $T \leq 100$ K, the fit function applied to the short distance-related prefactor V_{nl}^1 exhibits an exponent $\alpha_{1,\text{low}} = 2.1$, while the fit function applied to the large distance-related prefactor V_{nl}^2 yields $\alpha_{2,\text{low}} = 1.4 < \alpha_{1,\text{low}}$. Quantitatively, both values $\alpha_{1,\text{low}}$ and $\alpha_{2,\text{low}}$ are consistent with the T^α dependence with $\alpha = \frac{3}{2} \cdot \dots \cdot \frac{5}{2}$ originating from the spin to magnon and magnon to spin conversion efficiencies $G_{\text{em}} \propto T^{\frac{3}{2}}$ and $G_{\text{me}} \propto T$ predicted in Ref. [23]. However, since the authors of Ref. [23] also propose that for small distances $d < \lambda_{\text{m}}$ the signal becomes independent of G_{me} (resulting in $\alpha = \frac{3}{2}$), one would expect that the short distance-related exponent $\alpha_{1,\text{low}}$ should be smaller compared to the large distance-related exponent $\alpha_{2,\text{low}}$. In contrast, we find $\alpha_{2,\text{low}} = 1.4 < \alpha_{1,\text{low}} = 2.1$. However, as we will discuss later in this section, the short and long distance regime are likely to originate from different driving forces of the magnon diffusion (in particular the gradient in the magnon temperature T_{m} and magnon chemical potential μ_{m} , respectively), such that the comparison to the interface conversion efficiencies of Ref. [23] (G_{em} and G_{me}), which are purely based on a gradient in the magnon particle number density, might be inappropriate.

At higher temperatures $T \gtrsim 100$ K, the exponents $\alpha_{1,\text{high}} = 1.2$ and $\alpha_{2,\text{high}} = 1.1$ for both the short and large distance regime roughly reproduce the linear behaviour observed previously for the simple exponential fits (Eq. 4.5). As discussed before, this dependence

might be attributed to the dominance of thermal magnons with average energy $\bar{\epsilon}_{\text{mag}} \approx \frac{3}{4}k_{\text{B}}T$ (or in other words the dominance of the detection efficiency $G_{\text{me}} \propto \bar{\epsilon}_{\text{mag}}$ of Ref. [23]).

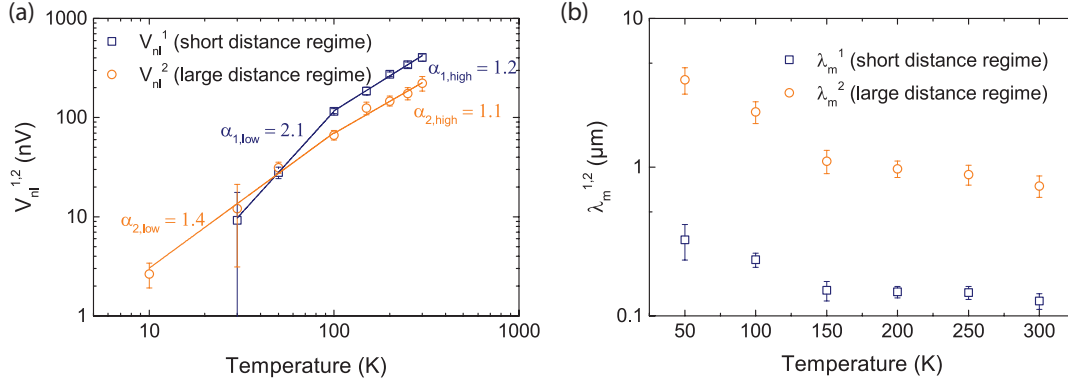


Figure 4.11: Fit parameters of Eq. 4.7 of Fig. 4.9(d). (a) Prefactors V_{nl}^1 and V_{nl}^2 plotted against temperature. The solid lines correspond to power law fits $A \cdot T^\alpha$. (b) λ_{m}^1 and λ_{m}^2 versus temperature.

The diffusion lengths for the short and large distance regime, λ_{m}^1 and λ_{m}^2 , are shown in Fig. 4.11 (b) for different temperatures. An increase of λ_{m}^1 and λ_{m}^2 with decreasing temperature is observed with a similar behaviour as λ_{m} (c.f. Fig. 4.10 (b)). Since the two decay lengths differ from each other in magnitude, it is reasonable to attribute them to different distance regimes. Since we described λ_{m} as a statistical average over all \mathbf{k} -dependent scattering times $\lambda_{\mathbf{k}}$ in Eq. 4.6, it is not possible to attribute the two diffusion lengths of Eq. 4.7 to different modes in the YIG spectrum (c.f. Fig. 4.6). However, it is reasonable to refer the short and long distance regime (represented by λ_{m}^1 and λ_{m}^2 , respectively) to different origins of the magnon diffusion. In our case, the diffusion is assumed to originate from the magnon temperature T_{m} and the magnon chemical potential μ_{m} for the short and large distance regime, respectively. While the magnon temperature T_{m} equilibrates to the phonon temperature T_{p} , such that $T_{\text{m}} = T_{\text{p}}$, the magnon chemical potential μ_{m} equilibrates to $\mu_{\text{m}} = 0$. Thus, due to the different microscopic processes regarding the equilibration of the driving forces for the diffusion, different characteristic time constants and hence length scales arise. This approach is pursued in the theory of Ref. [31], which proposes that the relaxation length λ_{m}^2 originating from the magnon chemical potential μ_{m} is much larger than the thermal relaxation length λ_{m}^1 arising from the magnon temperature T_{m} ⁸. These lengths are theoretically calculated and estimated in Ref. [31] by taking into account the thermal magnon velocity v_{th} together with different relaxation times arising from different scattering events. Since for the thermal magnon velocity v_{th} in Ref. [31] only the final result is given, we calculate it as

$$v_{\text{th}} = \frac{1}{N_{\text{mag}}} \int_0^\infty d\epsilon v(\epsilon) \mathcal{D}(\epsilon) f_{\text{BE}}(\epsilon, T) = \frac{\pi^{3/2}}{3\zeta(\frac{3}{2})} \frac{2\sqrt{J_s k_{\text{B}} T}}{\hbar} \approx 0.71 \frac{2\sqrt{J_s k_{\text{B}} T}}{\hbar} \quad (4.8)$$

⁸In Ref. [31] the length scales for magnon temperature- and chemical potential-related relaxations are denoted as l_{mp} and l_{m} , respectively.

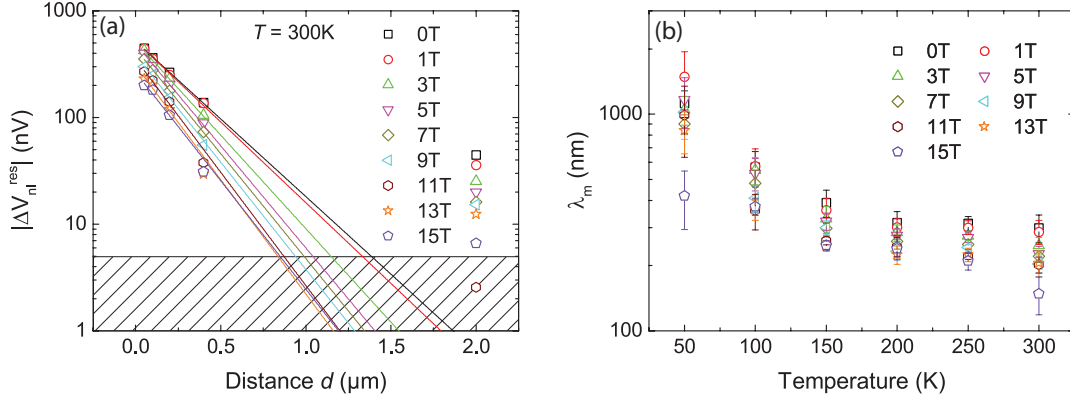


Figure 4.12: (a) Non-local voltage as a function of strip separation d , recorded for several magnetic fields up to 15 T at $T = 300$ K. The shaded region represents the noise floor of the measurement. (b) Magnon diffusion length λ_m extracted from the distance dependent data for various fields plotted versus temperature.

where we assumed a quadratic dispersion $\epsilon = J_s k^2$ and therefore $v(\epsilon) = \frac{1}{\hbar} \frac{\partial \epsilon}{\partial k} = \frac{2}{\hbar} \sqrt{J_s \epsilon}$ with $J_s = 8.458 \times 10^{-40} \text{J m}^2$ the spin wave stiffness constant in YIG [31]. When setting $0.71 \approx 1$, the result of Eq. 4.8 agrees with the expression given in Ref. [31]. At $T = 300$ K, Equation 4.8 gives $v_{\text{th}} = 25 \times 10^3 \text{m s}^{-1}$. The magnon temperature and chemical potential related length scales, that we associate with λ_m^1 and λ_m^2 , respectively, are theoretically calculated in Ref. [31]. After some approximations for room temperature they read as

$$\lambda_m^1 = v_{\text{th}} \sqrt{\frac{2}{3} \tau_{\text{mp}} \left(\frac{1}{\tau_{\text{mr}}} + \frac{1}{\tau_{\text{mp}}} \right)^{-1}} \quad \lambda_m^2 = v_{\text{th}} \sqrt{\frac{2}{3} \tau_{\text{mp}} \tau_{\text{mr}}} \quad (4.9)$$

where τ_{mr} is the magnon non-conserving scattering time related to the Gilbert damping α_G and τ_{mp} is the magnon-conserving magnon-phonon scattering time, which is assumed to be dominant at room temperature. With values $\tau_{\text{mr}} \sim 1$ ns and $\tau_{\text{mp}} \sim 1$ ps estimated in Ref. [31], $\lambda_m^1 \approx 20$ nm and $\lambda_m^2 \approx 650$ nm. Both values differ only by ~ 100 nm from the values extracted from our experiments in Fig. 4.11 (b) at 300 K. While this is no sufficient proof, the identification of λ_m^1 and λ_m^2 with magnon diffusion driven by temperature T_m and chemical potential μ_m is corroborated.

In the following, we focus on the magnon diffusion in the short distance regime, which is well described by Eq. 4.5 with a decay length λ_m as shown in Fig. 4.9 (c). Moreover we investigate the distance dependence of the MMR at different magnetic fields. Therefore the MMR voltage amplitudes $\Delta V_{nl}^{\text{res}}$ were extracted from field sweeps up to 15 T for $50 \text{ K} < T < 300 \text{ K}$ and the following Pt strip separations: $d = 50$ nm, 100 nm, 200 nm, 400 nm and $2 \mu\text{m}$. The result is plotted in Fig. 4.12 (a) for 300 K.

The solid lines in Fig. 4.12 (a) correspond to the exponential fits of Eq. 4.5 to the distance dependent MMR signal for different magnetic fields up to 15 T. The corresponding field dependent λ_m was extracted for temperatures between 50 K and 300 K and is shown in Fig. 4.12 (b). The qualitative dependence of λ_m on T is independent of magnetic field. However, for given, fixed temperature, the diffusion length decreases with increasing magnetic field strength, which is explained by the field induced suppression of low-energy

(subthermal) magnons [42]. As proposed in Ref. [42], the phonon-mediated magnon-magnon scattering is highly enhanced for high energy magnons, while it is suppressed for low magnon energies. As a consequence, a finite external magnetic field leads to a decreasing magnon lifetime τ due to the suppression of the weakly interacting low energy magnons (with larger lifetimes τ). In addition to this, there is also the effect of a reduction of magnons which occupy states with small wavevectors \mathbf{k} , since the magnon occupation number (given by the Bose-Einstein distribution function) is cut off at low energies by the external field. Small wavevectors exhibit larger lifetimes, leading to a further suppression of the magnon diffusion length λ_m .

In Sect. 4.1.2 we discussed the temperature dependent magnetic field suppression of the MMR caused by thermal occupation of the YIG magnon spectrum. However, we were not able to separate diffusive contributions to the MMR from interface contributions (separate the impact of magnon generation/detection from magnon transport). Therefore, we now separately investigate the field dependence of the prefactor V_{nl}^0 (attributed to the number of excited non-equilibrium magnons across the interface) and the magnon diffusion length λ_m (attributed to the diffusion of magnons in the bulk of YIG), as we did before in this section regarding the temperature dependence. The parameters are extracted by fitting Eq. 4.5 to Fig. 4.12 (a) for temperatures between 50 K and 300 K. The result is plotted in Fig. 4.13 (a) and (b) for V_{nl}^0 and λ_m , respectively.

The prefactor V_{nl}^0 decreases with increasing magnetic field strength for all temperatures. The corresponding relative suppression of the prefactor V_{nl}^0 , calculated as

$$\frac{V_{\text{nl}}^0(B = 0 \text{ T}) - V_{\text{nl}}^0(B = 15 \text{ T})}{V_{\text{nl}}^0(B = 0 \text{ T})} \quad (4.10)$$

is plotted versus temperature in Fig. 4.13 (c) (dark blue full squares). Interestingly, the temperature dependence of the suppression of V_{nl}^0 exhibits the same qualitative behaviour as the MMR signal suppression shown previously in Fig. 4.5 (d), at least for distances up to 500 nm. Therefore, we can state that the field suppression for short distances $d \lesssim 500$ nm is governed by interface related effects. To check the validity of this approach further, we compare the relative field suppression of V_{nl}^0 to the field suppression of $\Delta V_{\text{nl}}^{\text{res}}$ in the device with $d = 20$ nm (c.f. Fig. 4.5 (d)), where the diffusive contribution to the suppression should be very small at best. The suppression of $\Delta V_{\text{nl}}^{\text{res}}$ for the device with $d = 20$ nm is again shown in Fig. 4.13 (c) as light gray star symbols. The agreement with the suppression of the prefactor is striking. We find that both the total suppression of the device with $d = 20$ nm and the suppression of the prefactor V_{nl}^0 quantitatively match (grey stars and dark blue full squares). Both are strongly suppressed at high and low temperatures and go through a minimum in between. Since we attributed the prefactor V_{nl}^0 to all interface related effects (i.e. magnon generation/detection), the present analysis in Fig. 4.13 (c) strongly corroborates the impact of the optical high energy magnon mode proposed in Sect. 4.1.2 (c.f. Fig. 4.7). The counteracting ISHE signal generation of the optical magnons (compared to the acoustic magnons) accounts for the large field suppression at high temperatures and is additionally expected to be dominantly present for short distances, where interface related effects dominate.

Regarding the magnon diffusion length λ_m we also observe a decrease with increasing

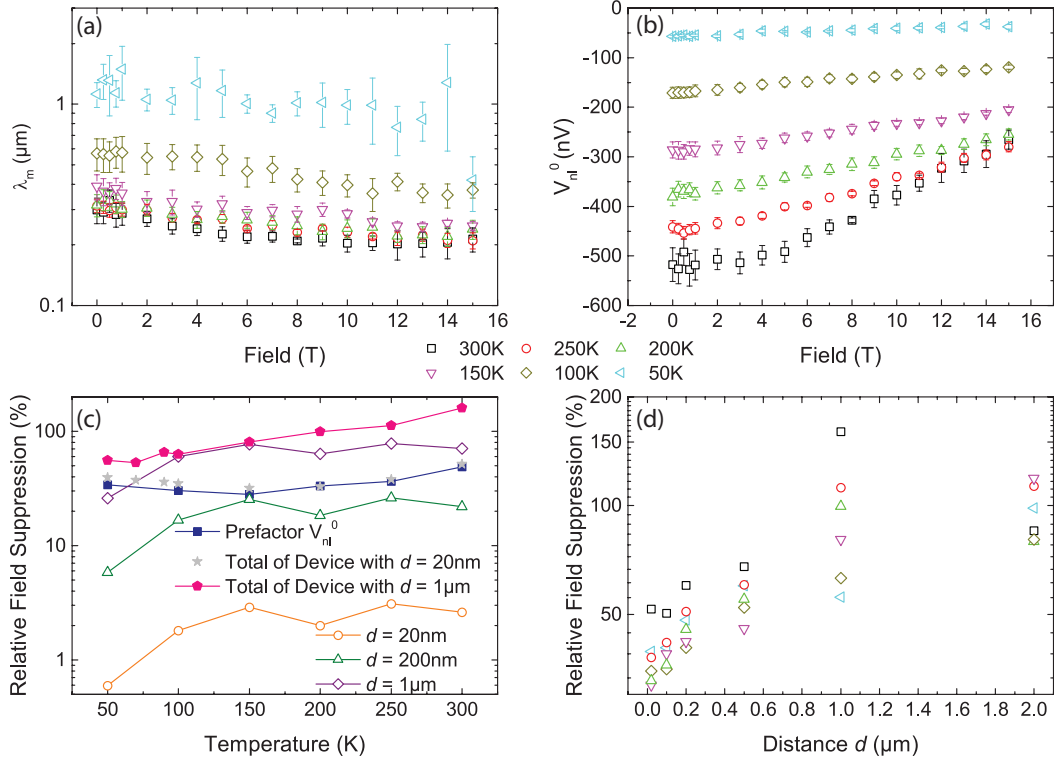


Figure 4.13: (a) Magnon diffusion length λ_m versus external field for several temperatures. (b) Prefactor V_{nl}^0 of the exponential decay fits to the distant dependent data plotted versus field for various temperatures. (c) Relative field suppression of the prefactor V_{nl}^0 (blue closed squares, calculated via Eq. 4.10) and for the exponential part $\exp(-\frac{d}{\lambda_m})$ of Eq. 4.5 calculated exemplarily for three different distances via Eq. 4.11 (open symbols). The full grey stars and pink pentagons show the total suppression of $\Delta V_{nl}^{\text{res}}$ of the devices with $d = 20\text{nm}$ and $d = 1\mu\text{m}$ from Fig. 4.5 (d), respectively. (d) Total relative field suppression of the MMR signal $\Delta V_{nl}^{\text{res}}$ versus the strip separation d for several temperatures calculated using Eq. 4.3.

field strength [44], which we qualitatively already discussed in the context of Fig. 4.12 (b). We now calculate the corresponding relative field suppression for the diffusive part as

$$\frac{\exp\left(-\frac{d}{\lambda_m(B=0\text{ T})}\right) - \exp\left(-\frac{d}{\lambda_m(B=15\text{ T})}\right)}{\exp\left(-\frac{d}{\lambda_m(B=0\text{ T})}\right)} \quad (4.11)$$

which is shown exemplarily for distances $d = 20\text{nm}$ (orange open circles), 200nm (green open triangles) and $d = 1\mu\text{m}$ (purple open diamonds) in Fig. 4.13 (c). The transport-related suppression generated by λ_m increases with increasing temperature. This is surprising since the suppression of magnon states with small wavevectors \mathbf{k} (that exhibit large lifetimes [42, 54]) is usually more efficient at low temperature. However, we have to recall that λ_m is described as a statistical average over all individual magnon scattering lengths $\lambda_{\mathbf{k}}$ (c.f. Eq. 4.6). Therefore it is difficult to give a intuitive explanation for the tempera-

ture behaviour of the field suppression, since there are many parameters affecting the field dependence of λ_m . However, a theoretical approach based on Eq. 4.6 for the temperature- and field-dependence of λ_m is given in Appendix A, which qualitatively reproduces the observed temperature dependent field suppression of λ_m .

From Figure 4.13 (c) we can easily see that the diffusive contribution to the field suppression exceeds the interface-related suppression of the prefactor V_{nl}^0 at approximately $d = 1 \mu\text{m}$ (purple open diamonds in Fig. 4.13 (c)). In other words, for $d \geq 1 \mu\text{m}$, the magnon diffusion and not the magnon generation/detection process governs the MMR response. Thus the qualitative temperature dependence of the transport-related suppression observed in Fig. 4.13 (c) (monotonic increase of the suppression with increasing temperature) should be also dominant for distances $d \gtrsim 1 \mu\text{m}$. This feature is indeed observed for $d = 1 \mu\text{m}$ in Fig. 4.5 (d) and is again shown in Fig. 4.13 (c) (pink open pentagons).

Finally, we complete our discussion of the temperature dependent MMR field suppression by depicting the total relative field suppression of $\Delta V_{nl}^{\text{res}}$ for several temperatures versus the strip separation up to $d = 2 \mu\text{m}$ in Fig. 4.13 (d). As we discussed before, the increase of the suppression with distance results from the impact of the magnetic field on the diffusive magnon transport, which is obvious in Fig. 4.13 (d) [44]. The saturation feature observed for $d = 2 \mu\text{m}$ results from the less pronounced increase of suppression with distance when $d \gg \lambda_m$. We can finally conclude that the magnon population-related (interface) field suppression as well as the diffusive contribution to the field suppression both play an important role for the MMR and dominate in the short and long distance regime, respectively. Hence, for the explanation of the temperature dependent field suppression both the interface- and transport-related field dependencies are necessary. Especially considering the high energy optical magnon branch becomes inevitable for the high temperature field suppression at short distances, since Fig. 4.13 (c) shows that the transport-related suppression (parameterized by λ_m) is low for short distances below $\sim 200 \text{ nm}$.

4.2 Thermal Contribution

In this Section, the thermal signals $V_{\text{loc}}^{\text{therm}}$ and $V_{\text{nl}}^{\text{therm}}$ of the local (c.f. Sect. 2.3) and non-local signals (c.f. Sect. 2.4) are investigated. The experimental parameters are the same as for the MMR, since both the resistive and thermal contributions can be extracted from the same set of data (see Sect. 3.3). Prior to the study of the experimental findings in Sect. 4.2.2, we first compile possible origins of the non-local contribution to the thermal signal in Sect. 4.2.1.

4.2.1 General Concepts

The charge current applied to the local Pt strip generates heat due to Ohmic losses, as shown in Fig. 4.14 (a). This Joule heat sprawls out to the YIG beneath, giving rise to a temperature gradient ∇T across the YIG|Pt interface. As described in Sect. 2.3, this temperature gradient drives a spin current across the interface which can be detected in the Pt as a voltage $V_{\text{loc}}^{\text{therm}}$ via the ISHE. This effect is known as the spin Seebeck effect (SSE) [14–16] (see Sect. 2.3). In the non-local strip, which is not heated, a finite thermal signal $V_{\text{nl}}^{\text{therm}}$ can be measured. In analogy to its local counterpart, we call this phenomenon the non-local spin Seebeck effect [12, 17, 33]. In this work, the origin of the non-local SSE is expected to arise from the following two scenarios:

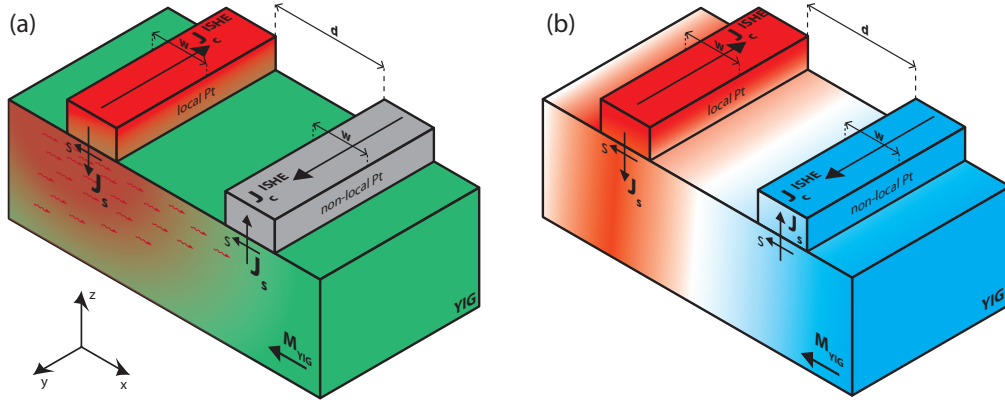


Figure 4.14: In both scenarios of the non-local Spin Seebeck effect, a charge current applied to the local Pt strip gives rise to a temperature difference ΔT_{em} of the magnon and electron system that leads to the (local) SSE. The direction of the emerging ISHE charge current results in a positive sign of the SSE amplitude $\Delta V_{\text{loc}}^{\text{therm}}$. (a) Non-local SSE scenario one: magnons are excited thermally in the YIG with their magnetic moment pointing antiparallel to the magnetization direction \mathbf{M} . The non-equilibrium magnon accumulation diffuses in the YIG and is converted to a spin current in the non-local Pt via the ISHE. Since the magnetic moment carriers (magnons) are antiparallely oriented to the magnetization orientation, the direction of the arising ISHE charge current is opposite to the locally detected ISHE current, resulting in a negative sign of the non-local SSE amplitude. (b) Non-local SSE scenario two: a macroscopic temperature gradient beginning from the current-heated local Pt strip (hot), across the YIG (slightly colder), until the non-local Pt strip (cold) could also explain the observed behaviour of the non-local SSE. The spin currents at the local and non-local strips, respectively, have opposite sign, since the temperature gradients at the interfaces are antiparallel, resulting in a negative sign of the non-local SSE as well. In this second picture, no magnon transport across the Pt strips is required but phononic heat transport is sufficient to observe a non-local SSE. We note that the non-local Pt strip is far away from the heat source, such that Pt and YIG should be in thermal equilibrium (no temperature gradient). However, since the Pt strip is connected to detection electronics, thermal gradients as just proposed could be present.

Firstly, a magnon diffusion process is possible, where magnons are not excited electrically by an electron spin accumulation μ_s at the interface (as for the MMR, see Sect. 2.4), but thermally from the current-induced heating at the injector strip [12], as depicted in Fig. 4.14 (a). The thermally excited non-equilibrium magnons diffuse through the YIG and can be detected non-locally via the ISHE, which is then similar to the MMR. However, in contrast to the MMR, the signal is expected to modulate with magnetization orientation α following a $\cos(\alpha)$ dependence, since only the detection of magnons at the non-local strip is angle dependent, while the excitation of magnons at the local strip is present for all angles α (thermal magnon generation instead of SHE-based generation) [12].

Secondly, a pure local SSE picture could explain the non-local signal, as illustrated in Fig. 4.14 (b). Here, the temperature gradient generated by the current-induced heating at the local strip is assumed to extend up to the non-local detector strip. Then, the origin of the non-local thermal signal reduces to a simple local spin Seebeck picture, where the electron-magnon temperature difference ΔT_{em} at the detector interface is the driving force for the interface spin current (see Sect. 2.3). Note that in this picture

the long-range information transport between the strips is purely described by phononic transport, without considering magnon diffusion from the injector.

For a comparison to experiments, we now examine what we expect from the absolute signs of the signals of the local SSE and the two models for the non-local SSE depicted in Fig. 4.14 (a) and (b).

1. Local SSE For the local SSE, when the top metal layer is heated, a temperature gradient arises across the interface, giving rise to a magnon spin current flowing from the hot (+ \mathbf{z}) to the cold ($-\mathbf{z}$) end, with \mathbf{s} pointing in $-\mathbf{x}$ -direction (in the coordinate system depicted in Fig. 4.14). An equivalent description would be that a magnetization current flows from the cold ($-\mathbf{z}$) to the hot (+ \mathbf{z}) end, since both vectors, spin current direction \mathbf{J}_s and magnetic polarization $\mathbf{m} = -\mathbf{s}$, are inverted. With the positive spin Hall angle Θ_{SH} of Pt, the sign of the technical charge current follows [4]

$$\mathbf{J}_c^{\text{ISHE}} = \Theta_{\text{SH}} \frac{2e}{\hbar} \mathbf{J}_s \times \mathbf{s} = -\Theta_{\text{SH}} \frac{2e}{\hbar} \mathbf{J}_s \times \mathbf{m} \quad (4.12)$$

with $\mathbf{m} = -\mathbf{s}$ the magnetic moment and spin polarization, respectively. These quantities have opposite sign, so one has to carefully distinguish between them. Eventually the spin current flows in $-\mathbf{z}$ -direction while the corresponding spin moment \mathbf{s} (magnetic moment \mathbf{m}) points along the $-\mathbf{x}$ - ($+\mathbf{x}$ -direction), which results in the flow of a technical charge current in the negative \mathbf{y} -direction in the coordinate system of Fig. 4.14, which corresponds to a positive sign of the SSE amplitude $\Delta V_{\text{loc}}^{\text{therm}}$ in our sign convention [55].

2. Non-local thermal magnon diffusion Due to Joule heating in the local Pt strip, magnons are excited thermally in the YIG (c.f. Fig. 4.14 (a)). Consequently, the magnon moment points in positive \mathbf{x} direction (as in 1.)⁹. At the interface of the non-local strip, the magnon current is pumped into the metal layer, such that \mathbf{J}_s flows along the $+\mathbf{z}$ -direction. With Equation 4.12 we find that the technical charge current $\mathbf{J}_c^{\text{ISHE}}$ flows in the positive \mathbf{y} -direction, which is the opposite sign as for the local case and therefore negative values for the non-local voltage amplitude $\Delta V_{\text{nl}}^{\text{therm}}$ are expected.

3. Non-local temperature gradient If the non-local Pt strip is colder than the YIG underneath, this leads to an interface temperature gradient opposite to the one in the local strip. Therefore, similar to the case of magnon diffusion, the sign is reversed with respect to the local SSE, giving a negative absolute sign of $\Delta V_{\text{nl}}^{\text{therm}}$.

Hence, the two models predict the same sign for the non-local thermal amplitudes. The discussion of the expected signs of the non-local SSE amplitudes $\Delta V_{\text{nl}}^{\text{therm}}$ is important, since a distance dependent sign inversion of the non-local $V_{\text{nl}}^{\text{therm}}$ signal is observed, as discussed in Sect. 4.2.2.1 [17, 33].

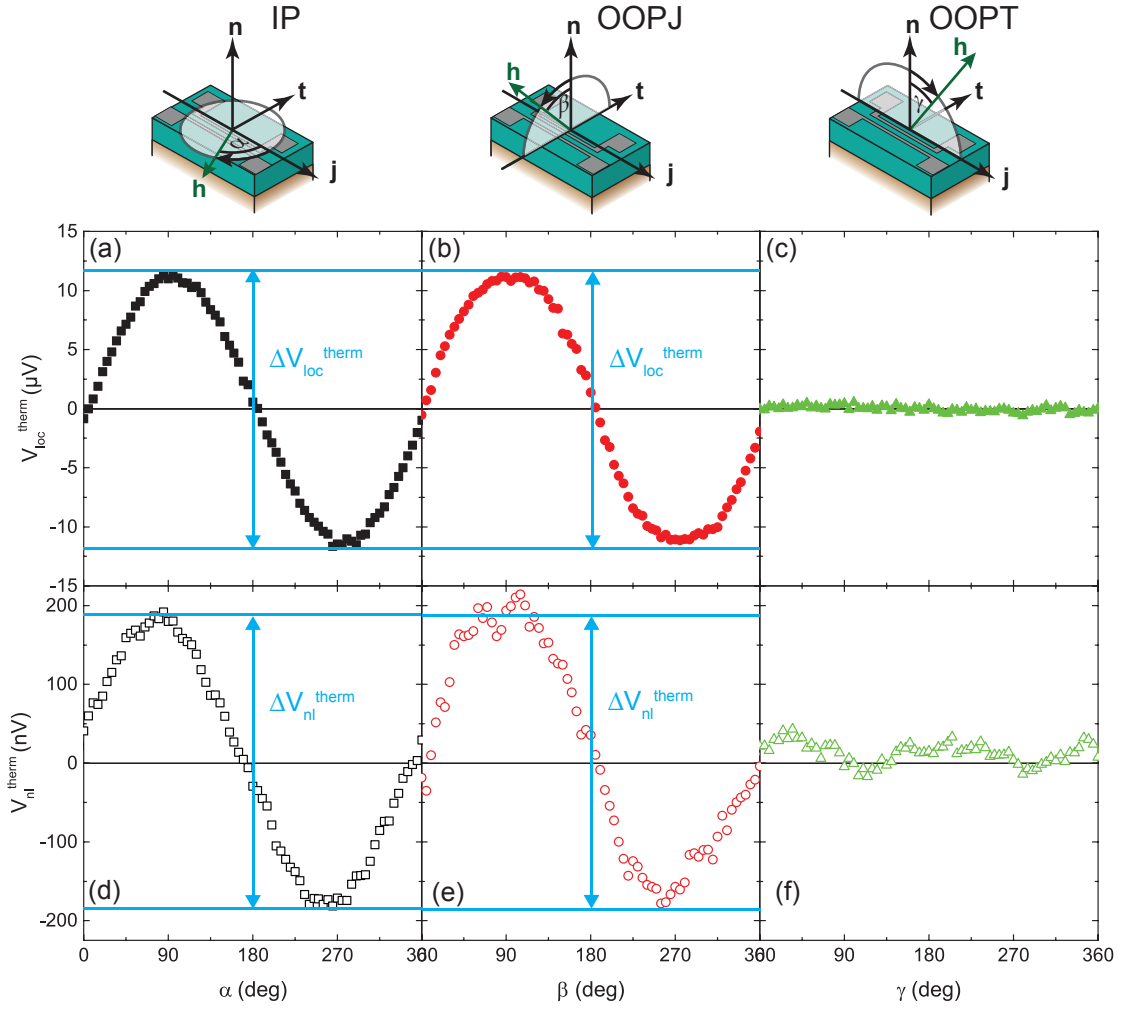


Figure 4.15: Local contribution $V_{\text{loc}}^{\text{therm}}$ of the SSE (antisymmetrized) when rotating the magnetic field $\mu_0 H = 1$ T at $T = 300$ K for a strip width of $w = 500$ nm in (a) the in plane configuration (IP), (b) the out of plane configuration around the current direction \mathbf{j} (OOPJ) and (c) in the out of plane configuration around the transverse direction \mathbf{t} (OOPT). The non-local SSE (antisymmetrized) signal $V_{\text{nl}}^{\text{therm}}$ for a structure with strip distance $d = 800$ nm is shown for the same experimental parameters as the local ones in (d) for the in plane rotation (IP), (e) in out of plane rotation around current direction (OOPJ) and (f) for a rotation of the magnetic field in the \mathbf{n} - \mathbf{j} -plane (OOPT). The local and non-local signal go to zero for field directions which are perpendicular to the SHE-induced interface spin accumulation.

4.2.2 Experimental Results

The local SSE signal $V_{\text{loc}}^{\text{therm}}$ follows a $\cos(\alpha)$ ($\cos(\beta)$) dependence on the orientation of the external magnetic field for IP (OOPJ) rotations (see Sect. 2.3). Typical ADMR measurements for the local SSE at $T = 300$ K in all three rotation planes for a magnetic field of $\mu_0 H = 1$ T are shown in Fig. 4.15 (a)-(c). Note that the signals are antisymmetrized, in

⁹The magnetic moment \mathbf{m} of thermally excited magnons always points opposite to the magnetization direction, since they act as a disturbance of the magnetic order.

order to cancel out additional thermal effects which are independent on the magnetization orientation. We measure finite signals in the IP and OOPJ configurations, and a vanishing signal in OOPT. This is expected, since the temperature driven interface spin current flowing in the \mathbf{n} -direction can be measured only if the spin polarization (which is given by the magnetization direction) is aligned with the \mathbf{t} -direction in the device geometry of Fig. 4.15. This gives rise to an inverse spin Hall current in the Pt flowing along the \mathbf{j} -direction (c.f. Sect. 2.1), along which the voltage is measured. For directions of the magnetization perpendicular to the \mathbf{t} -axis, no signal is measured due to a vanishing inverse spin Hall current in the \mathbf{j} -direction.

In Figure 4.15 (d)-(f) the non-local SSE voltage signal $V_{\text{nl}}^{\text{therm}}$ is shown for a device with strip distance $d = 800 \text{ nm}$ in all three rotation planes. Similar to the local SSE, the angular dependence exhibits a $\cos(\alpha)$ ($\cos(\beta)$) behaviour when the external field is rotated IP (OOPJ), while it vanishes in OOPT. This behaviour is expected for both scenarios of the non-local SSE presented previously (see Fig. 4.14). For the non-local temperature gradient model, the angle dependent behaviour is explained similarly to the local SSE. For the thermal magnon diffusion model, the angular dependence arises from the detection at the non-local Pt strip. While the thermal injection of magnons is active for all magnetization directions, the detection is dependent on the relative angle between the magnon polarization (which is given by the magnetization) and the \mathbf{t} -axis (see Fig. 4.15). In analogy to the MMR, the electron spin accumulation μ_s (generated by the non-equilibrium magnons) at the non-local YIG|Pt interface generates an inverse spin Hall current in the \mathbf{j} -direction (along which the voltage is measured) only if the magnon polarization is collinear to the \mathbf{t} -axis. Note that our sign convention for the thermal signal amplitudes $\Delta V_{\text{loc}}^{\text{therm}}$ ($\Delta V_{\text{nl}}^{\text{therm}}$) attributes a positive sign to modulations with their maximum at 90° , while a negative sign is assigned to modulations with their minimum at 90° . While the local SSE in YIG is always positive, we will show in the next Section that the sign for the non-local SSE depends on the strip separation d (c.f. Sect. 4.2.2.1).

In the following, we start with the distance dependence of the non-local SSE in Sect. 4.2.2.1. Thereafter, we focus on the temperature dependence in Sect. 4.2.2.2. Finally, the magnetic field dependence of the non-local SSE is investigated in Sect. 4.2.2.3.

4.2.2.1 Distance Dependence

The investigation of the distance dependence of the non-local SSE signal $\Delta V_{\text{nl}}^{\text{therm}}$ is a powerful way to get insight into the microscopic origins of the effect. The non-local voltage signals $V_{\text{nl}}^{\text{therm}}$ were measured on devices with separation distances $d = 20 \text{ nm}$ to $d = 10 \mu\text{m}$ and a constant strip width of $w = 500 \text{ nm}$ on a $2 \mu\text{m}$ thick YIG film. Additionally we investigate a $5 \mu\text{m}$ thick YIG film with devices featuring $d = 50 \text{ nm}$ to $d = 5 \mu\text{m}$. Similar to the resistive measurements, in plane rotations with an external field of $\mu_0 H = 1 \text{ T}$ in a temperature range of 5 K to 300 K were carried out for every device¹⁰. In Figure 4.16 (a) typical ADMR modulations at $T = 50 \text{ K}$ for three different distances $d = 50 \text{ nm}$, 500 nm and $2 \mu\text{m}$ are shown for the $2 \mu\text{m}$ thick film. Interestingly, the signal changes its sign from a positive to a negative value with increasing distance [17, 33]. This means that our previously discussed non-local SSE models (which both predict negative sign for $\Delta V_{\text{nl}}^{\text{therm}}$) do only agree with experiment for large distances d , where the sign of

¹⁰Note that the given temperatures of the measurements in Sect. 4.2 always refer to the bath temperature of the cryostat.

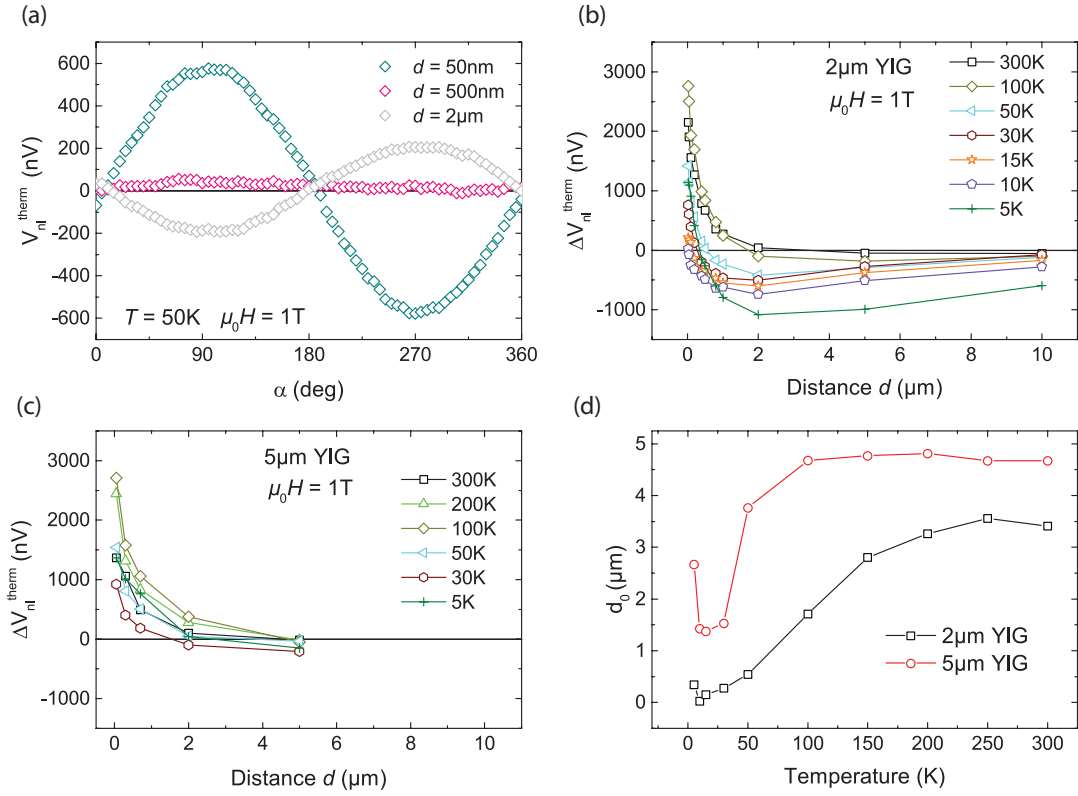


Figure 4.16: (a) Non-local thermal ADMR signals at $T = 50\text{K}$ for three different strip separation distances d , measured on a $2\mu\text{m}$ thick YIG film. (b) ΔV_{nl}^{therm} versus strip separation distance d for different temperatures on a $2\mu\text{m}$ thick film. (c) Distance dependence of the non-local SSE on a $5\mu\text{m}$ thick YIG film. (d) The separation distance d_0 , at which the sign change in the non-local thermal signals occurs, plotted against the corresponding temperature for the $2\mu\text{m}$ and $5\mu\text{m}$ thick YIG film.

the non-local voltage ΔV_{nl}^{therm} is reversed with respect to the sign of the local SSE. The sign change is present for all temperatures, as shown in Fig. 4.18 (b), where the signal amplitude ΔV_{nl}^{therm} is plotted versus distance for temperatures ranging from 300 K to 5 K for the $2\mu\text{m}$ thick YIG film. Dependent on temperature, the signal changes its sign at a certain distance d_0 and gradually decreases towards zero signal for large distances up to $10\mu\text{m}$. The overall distance dependent signal shifts towards more negative values for decreasing temperature.

A theoretical approach for the occurrence of a positive sign in the non-local SSE for small distances is described in Ref. [33]. Here, the charge current heating-induced magnon currents in YIG are divided into a magnon heat flow $J_{m,q}$ and a diffusive magnon flow $J_{m,diff}$ originating from the temperature gradient ∇T and the thermally generated magnon accumulation μ_m , respectively. Close to the locally heated Pt strip, the authors of Ref. [33] calculate that the magnon accumulation μ_m is negative, meaning that the YIG magnon population is depleted spherically around the heated strip. Further away from the strip, the magnon distribution is inverted since excess magnons are present corresponding to an accumulation of magnons. Far away from the heated strip μ_m thus is positive. This implies that μ_m must change sign at some distance from the heating strip. Intuitively,

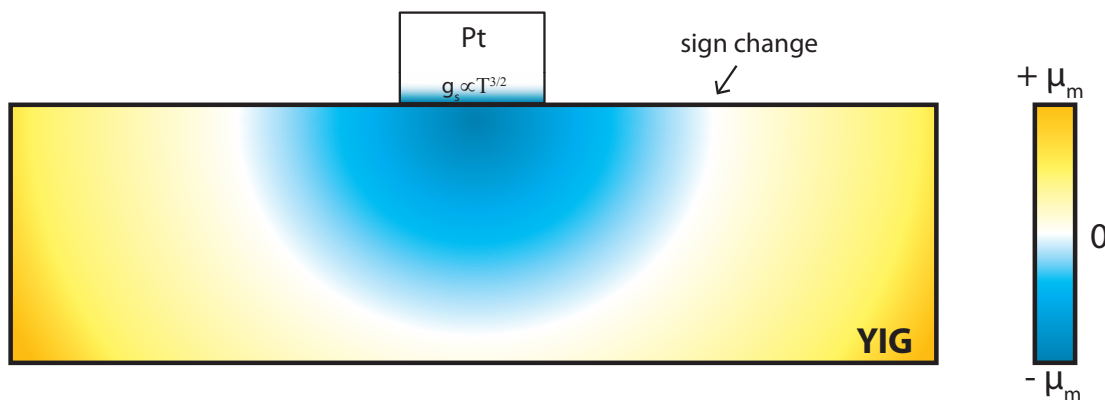


Figure 4.17: The heating in the Pt strip generates a spherical negative magnon accumulation μ_m (magnon depletion, blue color) around the heated Pt. The interface layer between the YIG and Pt includes the finite spin current transparency, which is given by the effective spin mixing conductance g_s [31]. Further away from the strip, the magnon distribution changes its sign to a positive accumulation (yellow color). Note, that in the sign convention chosen for this thesis, a negative (positive) magnon accumulation μ_m corresponds to a positive (negative) SSE signal. Figure adapted from [33].

the temperature-gradient induced positive and negative magnon accumulations build up similarly to the usual Seebeck effect in electrical conductors, where positive and negative charge accumulations build up at the hot and cold end of a temperature gradient. Hence, the thermally generated magnons beneath the heated Pt flow away from the hot region and accumulate at the boundaries far away from the heater. More rigorously, the negative magnon accumulation μ_m around the heated Pt strip arises due to the boundary conditions for the total magnon current $J_m = J_{m,q} + J_{m,diff}$, as described in Ref. [33]. While the magnon current $J_m = 0$ at the YIG boundaries (more precisely: at the YIG boundaries to vacuum), it is finite at the YIG|Pt interface, where $J_m = g_s \mu_m (d = 0)$ with g_s the effective spin mixing conductance at the YIG|Pt interface [31,33]. With these conditions, a magnon distribution μ_m as depicted in Fig. 4.17 arises, which is positive at the YIG boundaries far away from the heated Pt, while negative in vicinity to the heater. Note, that in thermal equilibrium the magnon accumulation μ_m is zero due to the non-conserved particle number of magnons (which corresponds to $\mu_m = 0$).

In our measurement configuration (or sign convention) the negative magnon accumulation generates a positive SSE voltage sign for ΔV_{nl}^{therm} for short distances, while the positive magnon accumulation generates a negative sign at large distances. The depletion region around the local strip is calculated to become larger when the YIG thickness increases, which is because the magnon accumulation is distributed more sparsely over a larger area compared to a thinner film, resulting in a larger negative μ_m [33]. This feature can be corroborated by our data, when we compare panel (b) and (c) of Fig. 4.16 for the 2 μm and 5 μm thick YIG film, respectively. It is obvious that the signal is shifted towards larger positive values for the 5 μm thick film, which corresponds to a sign change at larger distance d_0 (for a fixed temperature) and therefore a broader magnon depletion region.

In Figure 4.16 (d) the critical distance d_0 , at which the sign change occurs, is plotted for the 2 μm and 5 μm thick film versus temperature (black open squares and red open circles,

respectively). The critical distance d_0 is extracted by linearly interpolating between the data points of Fig. 4.16 (b) and (c) and taking the intersect with the zero line. The increase of d_0 with increasing temperature for $T \geq 10$ K is likely to be explained by the freezing out of magnons with decreasing temperature. According to Ref. [31], $\sigma_m \propto \Lambda^{-3}$ with $\Lambda = \sqrt{\frac{4\pi J_s}{k_B T}}$ the magnon thermal de Broglie wavelength. Since the thermal magnon number $N_{\text{mag}} \propto \left(\frac{k_B T}{J_s}\right)^{3/2} \propto \Lambda^{-3}$, such that the magnon spin conductivity $\sigma_m \propto N_{\text{mag}}$, we expect σ_m to decrease with decreasing magnon number [31,56]. As a consequence thereof, the magnon depletion region around the heated Pt strip becomes smaller, resulting in the observed decrease of the critical distance d_0 in experiment [17]. This is consistent with the measurement of the magnon spin conductivity in Ref. [56], which exhibits a qualitative similar temperature dependence as d_0 . The critical distance d_0 for the 2 μm thick film exhibits a saturation feature starting from ~ 250 K at approximately $d_0 \approx 3.5 \mu\text{m}$. This also agrees with previous measurements at room temperature by Shan et al. who found a linear dependence of the sign-reversal distance $d_0(t_{\text{YIG}} = 2 \mu\text{m}) \approx 1.6 \cdot t_{\text{YIG}}$ on the YIG thickness t_{YIG} [33]. However, for the 5 μm thick film $d_0(t_{\text{YIG}} = 5 \mu\text{m}) \approx 4.5 \mu\text{m}$ at $T = 300$ K, which does not match with the predicted proportionality factor 1.6. The experimental finding that the saturation value of d_0 is considerably higher for the thick 5 μm film compared to the 2 μm film further indicates that the extension d_0 of the negative magnon accumulation μ_m (blue color in Fig. 4.17) is determined by the saturation value of the magnon spin conductivity σ_m [56]. This is reasonable, since thicker YIG films are indeed expected to exhibit a larger saturation value of σ_m because of the larger number of thermal magnons in a thick film, giving rise to a larger d_0 . The fact that the saturation sets in at a considerably lower temperature ($T \approx 100$ K) for the thicker film compared to the thinner film ($T \approx 250$ K) indicates that the negative magnon accumulation μ_m cannot be manipulated by temperature as much as for the thinner film. This suggests that the magnon spin conductivity σ_m (which is assumed to determine the temperature dependence of d_0) saturates at a lower temperature for thicker films. This feature can be explained by taking into account the magnon diffusion length $\lambda_m \propto \tau$ with τ the magnon relaxation time (c.f. Eq. 4.6 in Sect. 4.1.3 and Appendix A). Since $\sigma_m \propto \tau$ [31], we expect it to decrease with increasing temperature due to the decreasing λ_m (c.f. Sect. 4.1.3). In contrast to this, the thermally populated magnon number increases with increasing temperature, which suggests an increase of σ_m . These counteracting factors give rise to the saturation of σ_m at certain temperature, as observed in Ref. [56]. In a thin film with a low absolute number of thermal magnons (compared to a thick film), the saturation of σ_m should occur at relatively high temperature, since the number of magnons becomes large not before a certain temperature is reached. In a thicker YIG film with a larger absolute number of thermal magnons, the saturation of σ_m is then expected to set in at lower temperature.

In Ref. [33] it is also proposed that the depletion region becomes larger when the interface transparency becomes more opaque, which can be parameterized by the magnon to spin interface conversion efficiency (g_s in Refs. [31,33]). This is explained by the boundary conditions mentioned before, since a more opaque interface (lower g_s) leads to less magnon spin current $J_m = g_s \mu_m(d=0)$ across the YIG|Pt interface, resulting in a higher amount of persisting "depleted" magnons (negative μ_m). Assuming a $T^{\frac{3}{2}}$ dependence of the spin conversion efficiency g_s [31] (or at least a strong suppression at low T [13,23]), we can conclude that the interface becomes less transparent with decreasing temperature. Consequently,

within the theory of Ref. [33], this should result in a shift of the sign change distance d_0 to larger distances for decreasing temperature, since the depletion region around the heated Pt strip is expected to increase. However, this cannot be corroborated by our data, as evident in Fig. 4.16 (d). For $T \geq 10$ K, we clearly see an increase of d_0 with increasing temperature for both YIG films, suggesting that the interface transparency, in terms of the spin conversion at the interface, does not play a major role in the temperature dependence of the non-local SSE [17]. However, it is certainly too simple to identify the effective spin mixing conductance g_s , and especially its temperature dependence ($g_s \propto T^{\frac{3}{2}}$), as a parameterization of the interface opacity. In particular, the temperature dependence of $g_s \propto g^{\uparrow\downarrow}$ does not arise directly from the spin-mixing conductance $g^{\uparrow\downarrow}$ (which is an established parameter for the interface opacity for spin currents [43]), but rather from the integration over the temperature dependent Bose-Einstein distribution function for magnons (Eq. (8) in Ref. [31]). This means that the temperature dependence of g_s originates from the temperature dependence of the population $N_{\text{mag}} \propto T^{\frac{3}{2}}$ of thermally occupied magnons. Thus, the interface opacity for spin currents should still be parameterized by $g^{\uparrow\downarrow}$, which is roughly independent of temperature [41].

In contrast to the monotonic increase of d_0 with temperature, an increase from $T = 10$ K to $T = 5$ K is evident in Fig. 4.16 (d) for both the $2 \mu\text{m}$ and $5 \mu\text{m}$ thick film. This may be an indicator for the interface transparency to have a higher impact on the magnon distribution at very low temperatures, but might also be related to a change of the temperature gradient due to different thermal coupling to the He bath at the transition to liquid He in the cryostat.

In the following, we argue that a possible contribution from a pure phononic heat transport to the non-local SSE, which was introduced in Fig. 4.14 (b) can be neglected for the non-local SSE signal. In general, a pure phonon heat transport at least cannot be ruled out completely, since it is likely that a finite temperature gradient is present at the detector as well. In addition to this a finite contribution from a non-local temperature gradient across the interface seems reasonable, since the distance dependent data in Fig. 4.16 (b) shows finite signals even at $d = 10 \mu\text{m}$, whereas the resistive MMR signal vanishes for all temperatures at $d = 10 \mu\text{m}$ (c.f. Sect. 4.1.3). However, it should be kept in mind that the thermal non-local SSE yields much larger voltage signals than obtained via direct electric magnon excitation in the MMR (e.g. $\Delta V_{\text{nl}}^{\text{therm}} \approx 700 \text{ nV} \gg \Delta V_{\text{nl}}^{\text{res}} \approx 100 \text{ nV}$ for $d = 500 \text{ nm}$ and $T = 300 \text{ K}$). This means that the thermal excitation of magnons either is much more efficient than the electrical injection, or that the thermal drive is much larger. In any case, a finite non-local voltage signal at much larger distances for the non-local SSE compared to the MMR is not surprising from this point of view. Furthermore we found an increasing magnon diffusion length with decreasing temperature up to $\lambda_m \approx 1.3 \mu\text{m}$ at $T = 50 \text{ K}$ in Sect. 4.1.3. Given this condition, together with the previously discussed decreasing broadening of the negative magnon accumulation μ_m at low temperatures (manifesting itself in the decrease of the critical distance d_0 with decreasing temperature shown Fig. 4.16 (d)), the non-local SSE signal should increase towards negative values with decreasing temperature (which corresponds to the positive magnon accumulation further away from the injector) due to the increase of λ_m and the decrease of d_0 , as observed in Fig. 4.16 (b), (c) and (d). To check this quantitatively, a reasonable number of long distance data starting from $d \approx 2 \mu\text{m}$ (since the positive μ_m is

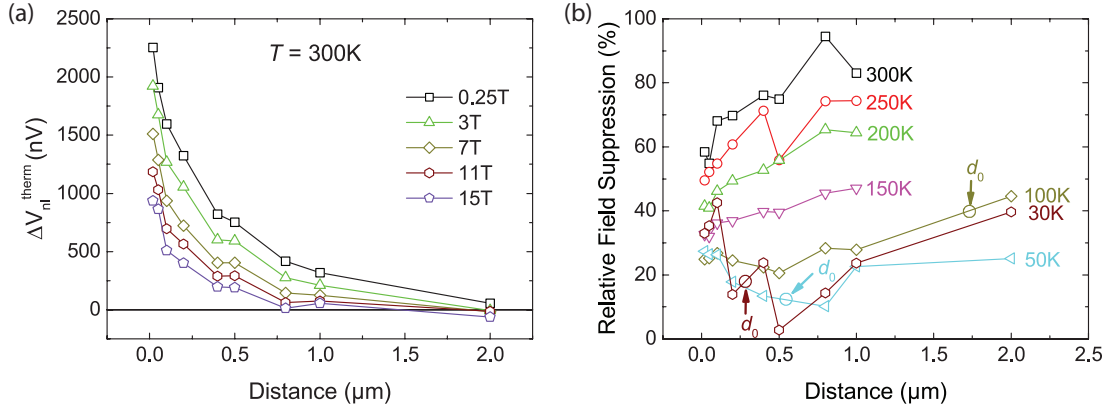


Figure 4.18: (a) Non-local SSE voltage $\Delta V_{nl}^{\text{therm}}$ versus distance at $T = 300\text{K}$ for several magnetic fields up to 15 T. (b) Relative field suppression calculated via Eq. 4.13 plotted versus strip separation distance for various temperatures.

mainly present there, giving rise to the negative signal) has to be investigated, in order to be able to extract a magnon diffusion length λ_m by fitting the negative low temperature signals exponentially. This magnon diffusion length should then be consistent with the diffusion lengths of the MMR at low temperatures. Note, that this is also consistent with the vanishing signals at low temperatures in the MMR, since we found that the thermal energy $k_B T$ of the system is the relevant energy scale for the magnon excitation, and not the electrically-induced spin accumulation μ_s . For the non-local SSE, the heating of the Pt strip ensures a thermal excitation even at very low temperatures $T < 50\text{K}$ (since the heating of the Pt gives rise to a magnon excitation with energies above $k_B T$), where the diffusion length is expected to be large in the order of several μm , resulting in large negative signals at low temperature and large distances.

In a next step, the distance dependence under the influence of higher magnetic fields is investigated. Figure 4.18 (a) exemplarily shows the non-local voltage $\Delta V_{nl}^{\text{therm}}$ for $T = 300\text{K}$ as a function of distance for various magnetic fields up to 15 T. The signals are extracted from field sweeps, where the external field is applied in plane and perpendicular to the Pt strips (corresponds to 90° and 270° in Fig. 4.16 (a), see also Sect. 4.2.2.3). The field suppresses the signal for all distances¹¹. In order to investigate the distance-dependent field evolution of the magnon transport quantitatively, we calculate the relative field suppression as

$$\frac{\Delta V_{nl}^{\text{therm}}(B = 0.25\text{ T}) - \Delta V_{nl}^{\text{therm}}(B = 15\text{ T})}{\Delta V_{nl}^{\text{therm}}(B = 0.25\text{ T})} \quad (4.13)$$

and plot this versus distance for various temperatures in Fig. 4.18 (b), where additionally the critical distance d_0 is indicated¹². The data points at or very close to the critical

¹¹One may notice, that the suppression of the signal at $d = 2\mu\text{m}$ in Fig. 4.18 (a) seems to be suppressed even from positive to negative signals. This is, however, very likely just a spurious effect caused by the low signal-to-noise for small non-local voltages.

¹²Note that for temperatures $T \gtrsim 150\text{K}$ the critical distances are beyond $2\mu\text{m}$ and therefore not covered by the field dependent data in this region.

distance d_0 of the corresponding temperature are omitted in the suppression data, since these cannot be evaluated reliably due to the low signal-to-noise ratio. For temperatures $T \gtrsim 100$ K, the suppression rises with increasing separation d , as expected from a diffusive magnon transport. For $d \gtrsim 1 \mu\text{m}$, however, the suppression with increasing distance is less pronounced. This is not surprising when we recall that $\lambda_m < 800$ nm for $T \gtrsim 150$ K (c.f. Subsect. 4.1.3), resulting in a very low magnon accumulation at distances above ~ 800 nm. As a consequence, the increase of field suppression with increasing distance is less pronounced for distances $d > \lambda_m$. Note that the distance independent field suppression for $d > 1 \mu\text{m}$ could be also an indicator for non-local temperature gradient model (c.f. Fig. 4.14 (b)) for the non-local SSE. In such a description magnons only participate at the detector interface for the generation of the spin current, but not for the lateral transport between the Pt strips, leading to a "local" SSE at the detector. As a result, the field suppression would be independent of distance as well. However, it is reported that the temperature decay along the separation d can be neglected for the non-local signal generation, since it decays much slower than the magnon chemical potential profile, such that the decay of the non-local SSE signal would persist up to very large distances of $\sim 50 \mu\text{m}$ [33]. Therefore the contribution from a phonon-mediated non-local temperature gradient is implausible. For low temperatures $T \leq 50$ K, the suppression seems to lower around d_0 and increases for $d > d_0$, which corroborates the thermally generated magnon distribution picture of Ref. [33] (see Fig. 4.17), since no field suppression should be observed when no magnons are present at d_0 . For $T = 100$ K, this behaviour cannot be observed, since too little data around $d_0(T = 100 \text{ K}) \approx 1.7 \mu\text{m}$ exists. At low temperatures $T \leq 50$ K, the suppression shows an increase with increasing distance for $d > d_0$, which is reasonable in the picture of an increasing magnon accumulation shortly beyond d_0 .

In conclusion, magnon diffusion and the corresponding magnon chemical potential profile (see. Fig. 4.17) rather well describes the non-local SSE, while a picture based on thermal gradients alone (see Fig. 4.14 (b)) does not account for the data. The increase of field suppression with increasing strip distance at short d is strong evidence for magnon diffusion, while the presence of finite signals at large distances $d \gg \lambda_m$ can be explained by a more efficient magnon excitation compared to the MMR and the increasing diffusion length with decreasing temperature.

4.2.2.2 Temperature Dependence

We now turn to the temperature evolution of the local and non-local SSE voltage signals $\Delta V_{\text{loc}}^{\text{therm}}$ and $\Delta V_{\text{nl}}^{\text{therm}}$, respectively. All temperature dependent measurements in this Section are obtained from magnetization orientation dependent measurements at $\mu_0 H = 1$ T for temperatures $5 \text{ K} < T < 300 \text{ K}$. Local measurements are presented for devices on two different YIG films with thicknesses $t_{\text{YIG}} = 2 \mu\text{m}$ and $t_{\text{YIG}} = 5 \mu\text{m}$, both with strip width $w = 500$ nm. The non-local signals were measured simultaneously on devices with separation distances $d = 20$ nm to $d = 10 \mu\text{m}$ on the $2 \mu\text{m}$ thick film, while we studied devices with $d = 50$ nm to $d = 5 \mu\text{m}$ on the $5 \mu\text{m}$ thick film. All devices presented in the following have a constant strip width of $w = 500$ nm.

(Local) Spin Seebeck Effect

Prior to the study of the temperature dependence of the non-local SSE, we first analyze the behaviour of its local analogue. Typical magnetic field rotations of the local thermal voltage signal $V_{\text{loc}}^{\text{therm}}$ are shown in Fig. 4.19 (a) for $T = 300\text{ K}$, 100 K and 5 K . The corresponding amplitudes $\Delta V_{\text{loc}}^{\text{therm}}$ extracted from fitting the angle dependent measurements are shown in Fig. 4.19 (b) as a function of temperature for devices on a $2\text{ }\mu\text{m}$ and $5\text{ }\mu\text{m}$ thick YIG film.

The signals exhibit an enhancement from 300 K down to a peak value at $\sim 100\text{ K}$ for the $2\text{ }\mu\text{m}$ film. This peak shifts to $\sim 90\text{ K}$ for the $5\text{ }\mu\text{m}$ YIG film. Below this temperature, the signal decreases again until $\sim 30\text{ K}$. A large enhancement at very low temperatures starting at approximately 30 K to the lowest measured temperature of 5 K is observed thereafter. This large enhancement sets in slightly earlier for the $2\text{ }\mu\text{m}$ thick film as for the $5\text{ }\mu\text{m}$ thick film. A maximum in the local SSE around 100 K has also been observed by other groups, see e.g. in Ref. [57]. The maximum is attributed to an increase of the mean magnon propagation length ξ of all thermally excited magnons with decreasing temperature. ξ is assumed to be inversely proportional to the Gilbert damping parameter α_G , which in turn is approximately linearly dependent on temperature, leading to $\xi \propto T^{-1}$ [57–59]. As a consequence, more magnons within ξ can be detected via the ISHE in the Pt with decreasing temperature, giving rise to the increase of the signal from 300 K down to the peak at $\sim 100\text{ K}$. The decrease of the signal with decreasing temperature beginning from $\sim 100\text{ K}$ thereafter is then attributed to the counteracting factor of a decreasing number of excited magnons at low temperature (according to the Bose-Einstein distribution function), since the propagation length ξ is assumed to become constant at low temperatures and therefore cannot increase further [57]. Moreover, the maximum shifts to a lower temperature for the thicker $5\text{ }\mu\text{m}$ YIG film, compared to the $2\text{ }\mu\text{m}$ YIG film. This thickness dependence of the local SSE can also be understood in terms of the counteracting temperature dependencies of the thermal magnon population and their propagation length ξ , according to Ref. [57]. For thicker films (as long as $\xi \gtrsim t_{\text{YIG}}$), a large number of magnons within the length scale of ξ can contribute to the SSE voltage, such that the decreasing number of magnons with decreasing temperature dominates not

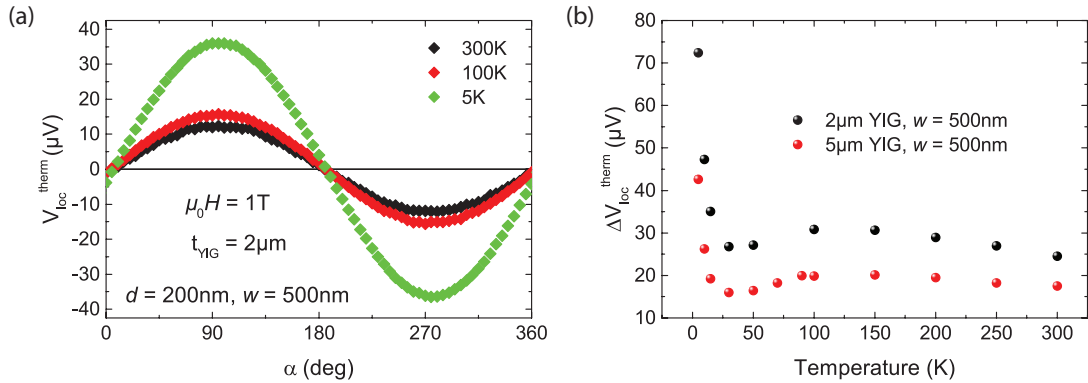


Figure 4.19: (a) ADMR measurements of the local SSE voltage $V_{\text{loc}}^{\text{therm}}$ for $T = 300\text{ K}$, 100 K and 5 K for $\mu_0 H = 1\text{ T}$. (b) Local SSE signal $\Delta V_{\text{loc}}^{\text{therm}}$ plotted versus temperature for a $2\text{ }\mu\text{m}$ and a $5\text{ }\mu\text{m}$ thick YIG film.

before a certain temperature is reached. For a thin film with a fewer number of thermal magnons, however, the dominance of the decrease in the number of magnons with decreasing temperature dominates already for a higher temperature. Note that in this work we use the magnon diffusion length λ_m to describe the propagation length of magnons (see Sect. 4.1.3). The qualitative temperature dependence of λ_m is similar to that of ξ , such that the same arguments can be given. The difference between ξ and λ_m might be hint in the difference between 1D and 2D transport properties, respectively. While the propagation length ξ in Ref. [57] is extracted from YIG thickness dependent 1D (local) spin Seebeck measurements, our magnon diffusion length λ_m is obtained from the distance dependent lateral 2D magnon transport across the strip separation from MMR measurements (c.f. Sect. 4.1.3). Therefore the boundary conditions for ξ and λ_m are distinctly different, since the thickness of the YIG film (which is in the order of several μm in our samples) is very small compared to the lateral film dimension (several mm). Thus it is not surprising that ξ and λ_m deviate strongly in magnitude ($\lambda_m \approx 300 \text{ nm} \neq \xi \approx 1.6 \mu\text{m}$ at $T = 300 \text{ K}$ [57]), since the magnon accumulation profile in the YIG strongly depends on the boundary conditions of the YIG film, as proposed in Ref. [33]. However, there is the inconsistency that $\lambda_m < t_{\text{YIG}}$ (especially at room temperature) in our samples, making the argumentation using λ_m questionable. Nonetheless, to take into account λ_m for the explanation of the maxima in the temperature dependent SSE signals might be still valid, since in Ref. [31] $\lambda_m \approx 10 \mu\text{m} > t_{\text{YIG}}$ at room temperature. This is still reasonable, since the magnon diffusion length λ_m in our measurements is extracted from a short distance regime, in contrast to Ref. [31].

The giant enhancement of the SSE signal at very low temperatures below 30 K has not been reported in literature to our knowledge so far. One could attribute this effect to an increasing propagation length ξ with decreasing temperature, since $\xi \propto T^{-1}$ and the Bose-Einstein distribution function for magnons only changes slightly at low temperatures. However, ξ is assumed to become constant at low temperature due to magnon-phonon interactions and boundary scattering mechanisms [57], making this "simple" explanation rather unlikely. We therefore rather attribute the large enhancement at low temperatures to interface-related effects. This is corroborated by the theory on the non-local SSE put forward in Ref. [33] (introduced in the previous Sect. 4.2.2.1), since the broadening d_0 of the negative magnon accumulation μ_m around the heated Pt strip (c.f. Fig. 4.17) is expected to increase due to an increasing interface opacity, which was observed for very low temperatures $T < 10 \text{ K}$ (see Fig. 4.16 (d)). Possibly, however, the giant enhancement at low temperatures is solely a spurious effect due to the current heating method. This is corroborated by Ref. [60], where the low temperature enhancement of the SSE was only reported for the current heating method and interestingly not for a laser heating method. Furthermore, previous measurements at the WMI using ex situ applied Pt films shows a similar enhancement at low temperatures for the SSE, suggesting that the effect arises from complex YIG|Pt interface properties.

Non-local Spin Seebeck Effect

Subsequently, we focus on the temperature dependence of the non-local SSE. Figure 4.20 (a) shows ADMR modulations of $V_{\text{nl}}^{\text{therm}}$ for $T = 300 \text{ K}$, 100 K and 15 K .

As discussed before, the non-local SSE signal exhibits a sign change at a certain strip separation d_0 , which is dependent on temperature. The temperature dependence for the non-local SSE signal $\Delta V_{\text{nl}}^{\text{therm}}$ for all investigated strip separations d is shown in Fig.

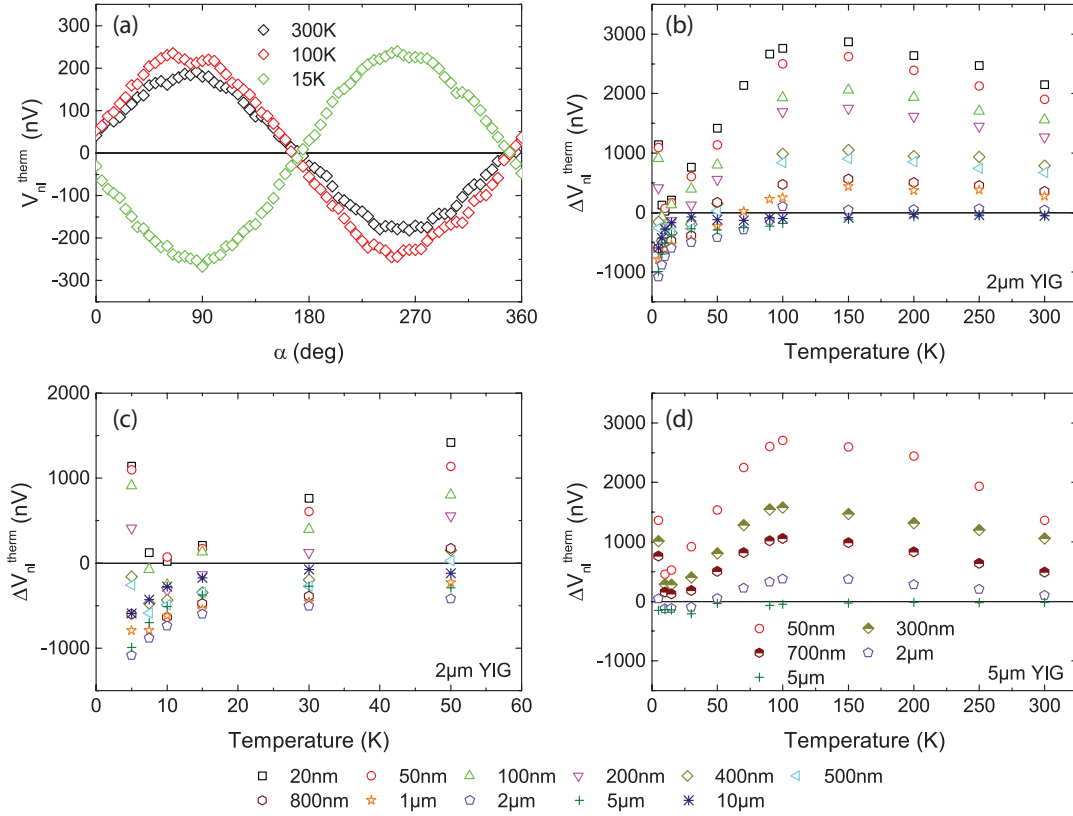


Figure 4.20: (a) Magnetic field orientation dependent signals of the non-local SSE voltage V_{nl}^{therm} for three different temperatures at $\mu_0 H = 1$ T and $d = 800$ nm. (b) Non local SSE amplitudes versus temperature for all investigated Pt strip separations d for a 2 μm thick YIG film. (c) Same as (b) but zoomed in for low temperatures. (d) Non-local thermal signal versus temperature for all investigated Pt strip separations d on a 5 μm thick film.

4.20 (b) and (d) for 2 μm and 5 μm thick YIG, respectively. Besides the sign change, the temperature dependencies of the 2 μm thick film for distances $d \leq 1$ μm look qualitatively similar as for the local case for temperatures down to ~ 50 K (c.f. Fig. 4.19 (b)). For the 5 μm thick film, this is true for distances $d < 2$ μm . The signals exhibit a positive peak at ~ 150 K (~ 100 K) for the 2 μm (5 μm) thick film. These peaks can be understood in the same manner as for the local SSE, i.e. by taking into account the magnon propagation length $\xi \propto T^{-1}$ as proposed in Refs. [57, 58]. In Sect. 4.1.3, we argued that the magnon diffusion length λ_m will increase with decreasing temperature, just as ξ does. In this spirit, we take the magnon diffusion length λ_m to become constant at low temperatures, which is likely to happen, since the scattering lengths of magnons have to be limited by finite magnon-phonon interactions or defect scattering. Then, the increase of λ_m together with the freezing out of thermal magnons with decreasing temperature gives rise to the observed peak in the non-local SSE. In fact, the very similar temperature dependence of the local and non-local SSE strongly corroborates that magnon diffusion is the key origin of the non-local SSE voltage signal, since it is crucial to take into account the magnon diffusion length to explain the temperature dependence. Furthermore, we also observe a peak-shift

to lower temperatures for thicker films, as we did for the local SSE, which is consistent with a magnon diffusion picture.

On a final note, we briefly discuss the low temperature behaviour of the non-local SSE for $T \leq 50$ K. The signals for the $2 \mu\text{m}$ thick film reach their maximum negative values at ~ 5 K for distances $d \gtrsim 2 \mu\text{m}$, as depicted in Fig. 4.20 (c), where the temperature dependence for the $2 \mu\text{m}$ thick film is shown in more detail for low temperatures up to 60 K. For distances $d \lesssim 1 \mu\text{m}$, a signal increase towards positive values is observed at 5 K. This is also observed for the $5 \mu\text{m}$ thick film in Fig. 4.20 (d). However, a very slight increase is now observed even for distances up to $d \approx 5 \mu\text{m}$, compared to only $d \approx 2 \mu\text{m}$ for the $2 \mu\text{m}$ thick film. In general, this increase may be attributed to the large low temperature enhancement of the local SSE, since the increase is more pronounced for short strip distances d , where the non-local devices reach the local limit (this can be also seen from the increase of d_0 from 10 K to 5 K in Fig. 4.16 (d)). The fact that the increase at 5 K is observable at larger distance for the thicker YIG film, corroborates the picture of a negative magnon accumulation around the heated Pt strip proposed in Ref. [33] (c.f. Fig. 4.17). This conclusion is based on the fact that the extension d_0 of the negative magnon accumulation μ_m is larger for thicker films (see Fig. 4.16 (d)) [33]. Given this condition, the increase of the non-local SSE at 5 K is then indeed expected to be evident at larger distances for a thicker film, compared to a thin film.

In conclusion, the very similar qualitative temperature dependence of the non-local SSE compared to its local analogue strongly corroborates the idea that magnon diffusion is the main origin of the non-local SSE. Moreover, the magnon chemical potential profile calculated in Ref. [33] (c.f. Fig. 4.17) has to be taken into account to explain the sign change of the non-local SSE, which is further strong evidence for the magnon diffusion model.

4.2.2.3 Magnetic Field Dependence

In the following, local and non-local field dependent spin Seebeck data is discussed for devices with strip separations up to $d = 2 \mu\text{m}$. To this end, field sweeps up to 15 T were conducted in a temperature range of $1.5 \text{ K} < T < 300 \text{ K}$. The field is applied in plane and perpendicular to the Pt strips, in order to ensure the maximum detectable signal (see Sect. 2.3).

(Local) Spin Seebeck Effect

Figure 4.21 (a) shows the local SSE field sweep signal $V_{\text{loc}}^{\text{therm}}$ for a device with $d = 200$ nm and $w = 500$ nm for several temperatures from 300 K to 1.5 K. The signal amplitude $\Delta V_{\text{loc}}^{\text{therm}} = V_{\text{loc}}^{\text{therm}}(+\mu_0 H) - V_{\text{loc}}^{\text{therm}}(-\mu_0 H)$ is then extracted for every field value. This is shown in Fig. 4.21 (b) for the same structure with $d = 200$ nm and $w = 500$ nm. It is easy to see that the suppression is much larger for low temperatures, while the curves are almost flat for $T \geq 100$ K. This can be seen in Fig. 4.21 (c) as well, where the signal $\Delta V_{\text{loc}}^{\text{therm}}$ is plotted versus temperature for various magnetic fields up to 15 T. The inset shows the data enlarged for temperatures $T \leq 15$ K. The strong enhancement of the signal at low temperatures starting from 15 K is still present for low magnetic fields, but is highly

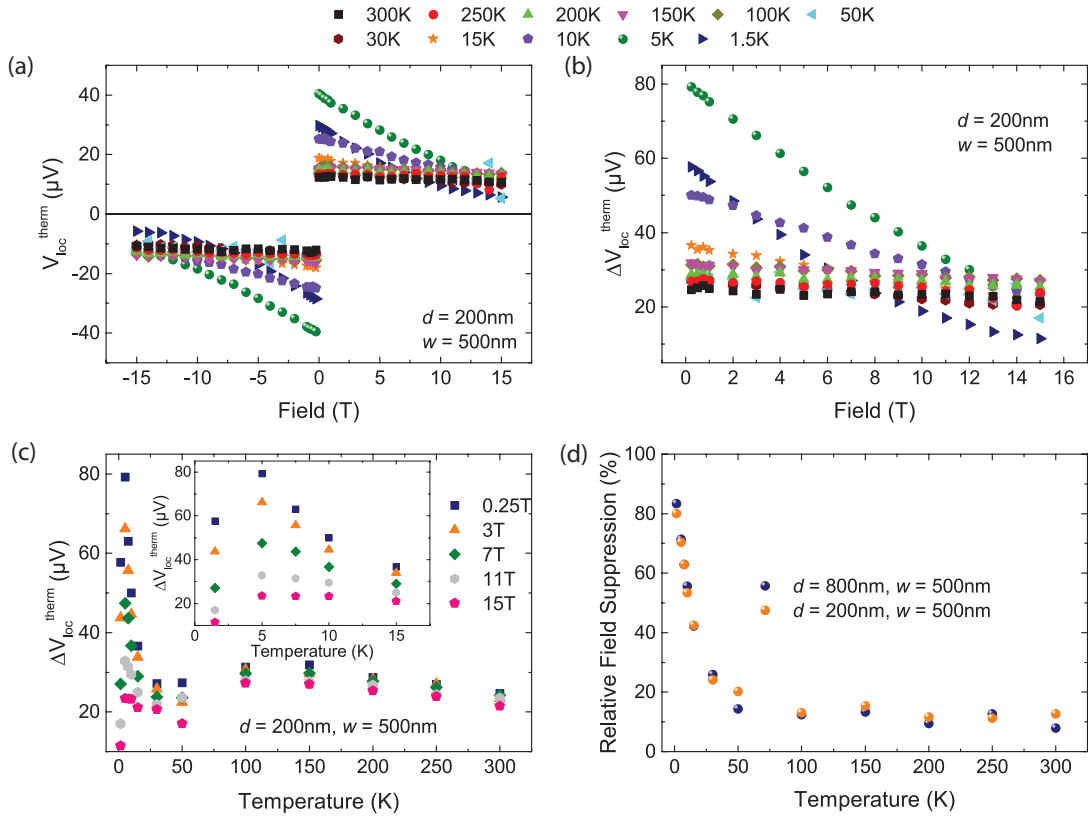


Figure 4.21: (a) Magnetic field sweeps for the local thermal signal V_{loc}^{therm} measured at the local strip of a device with $d = 200\text{ nm}$ and $w = 500\text{ nm}$ for temperatures of 300 K down to 1.5 K. (b) Extracted local SSE amplitude ΔV_{loc}^{therm} from the field sweep data of panel (a). (c) Temperature dependence of ΔV_{loc}^{therm} for different external fields for the same device with $d = 200\text{ nm}$ and $w = 500\text{ nm}$. (d) Relative field suppression versus temperature of the local SSE for two different devices calculated with Eq. 4.14.

suppressed for high magnetic fields. In order to give a more quantitative analysis for the field suppression, we calculate the relative field suppression as

$$\frac{\Delta V_{loc}^{therm}(B = 0.25\text{ T}) - \Delta V_{loc}^{therm}(B = 15\text{ T})}{\Delta V_{loc}^{therm}(B = 0.25\text{ T})}. \quad (4.14)$$

The result is shown in Fig. 4.22 (d) for two different devices with same strip width $w = 500\text{ nm}$.

The suppression is basically constant for $T = 300\text{ K}$ down to 50 K, but is highly enhanced up to $\sim 80\%$ at 1.5 K. This strong suppression of the SSE at low temperatures was already discussed beforehand in Sect. 4.1 for the MMR and is attributed to the field-induced spin wave gap in the magnon excitation spectrum [45]. Intuitively speaking, the suppression is high at low T because the thermally excited magnons only populate low frequency states (corresponding to small wavevectors \mathbf{k}), which can be easily depopulated by the field-induced spin wave gap when $k_B T \sim g\mu_B B$. Due to the fact that the suppression is finite even at high temperature (still roughly $\sim 10\%$), low frequency magnons are assumed to dominate the SSE signal [42, 45, 53].

Interestingly, the low T enhancement of the local SSE signal persists only down to $T = 5$ K, but decreases again for $T = 1.5$ K, in contrast to the still enhanced relative field suppression at 1.5 K (see inset of Fig. 4.22 (c)). This decrease is reasonable, since all temperature gradients should vanish at very low temperatures, such that the signal should completely vanish for $T \rightarrow 0$. The still enhanced field suppression is reasonable as well, since the small thermal magnon population can be suppressed with field even more efficiently.

Non-local Spin Seebeck Effect

The non-local SSE field sweep data is exemplarily shown in Fig. 4.22 (a) for a device with $d = 100$ nm for several temperatures from 300 K to 5 K¹³. The corresponding non-local SSE amplitudes $\Delta V_{\text{nl}}^{\text{therm}} = V_{\text{nl}}^{\text{therm}}(+\mu_0 H) - V_{\text{nl}}^{\text{therm}}(-\mu_0 H)$ are then extracted for every field, as depicted in Fig. 4.22 (b). For the same device with $d = 100$ nm the non-local SSE voltage amplitude $\Delta V_{\text{nl}}^{\text{therm}}$ is plotted versus temperature for several different magnetic fields up to 15 T in Fig. 4.22 (c). As expected for a magnon driven effect [14], the signal is suppressed by an external magnetic field. For a quantitative analysis of the data, the relative field suppression calculated as

$$\frac{\Delta V_{\text{nl}}^{\text{therm}}(B = 0.25 \text{ T}) - \Delta V_{\text{nl}}^{\text{therm}}(B = 15 \text{ T})}{\Delta V_{\text{nl}}^{\text{therm}}(B = 0.25 \text{ T})} \quad (4.15)$$

is shown in Fig. 4.22 (d) for different strip separations $20 \text{ nm} < d < 1 \mu\text{m}$. The local suppression previously depicted in Fig. 4.21 (d) is included in Fig. 4.22 (d) for comparison¹⁴.

The strong increase of the suppression below 50 K, which is similar to the local SSE, is ascribed to the efficient suppression of magnons with low \mathbf{k} at low T , as discussed for the MMR in Sect. 4.1.2. Furthermore, the minimum of the suppression at approximately 50 K for the non-local signals in Fig. 4.22 (d) can be attributed to the picture put forward in Sect. 4.1.2, where the suppression of the magnon population for intermediate temperatures is lowered due to the ineffective suppression of magnons with large energies and large \mathbf{k} -vectors. While the field suppression of the local SSE signal remains at a constant value of $\sim 10\%$ for $T > 50$ K, the non-local SSE is subject to a strong field suppression even at high temperatures. A similar field suppression at high temperatures was also observed for the MMR (see Sect. 4.1.2). We attributed this effect to the contribution of a second optical magnon branch at high temperatures, which has opposite chirality compared to the fundamental mode. Thus, the high temperature field suppression of the non-local SSE can be rationalized in the same manner as in the MMR (see Fig. 4.7 of Sect. 4.1.2). Due to the thermal population of the optical mode for $T \geq 260$ K [48, 50], this mode should obviously contribute to both the local and non-local SSE. Apparently, the influence of the optical mode cannot be observed for the local SSE, since the field suppression remains constant up to 300 K. This indicates that the optical magnons exhibit a larger diffusion length than the magnons of the acoustic fundamental mode, such that their contribution to the non-local SSE is larger. Then, the local signal is dominated by the large amount of magnons with the short diffusion length at all temperatures, while the non-local signal at high temperatures and large strip separations is affected more strongly by magnons

¹³Note, that the non-local SSE data is not shown and discussed for the lowest measured temperature $T = 1.5$ K, since these data exhibits very strange features that have to be investigated in more detail in the future with high resolution field sweeps around 0 T.

¹⁴For reasons of clarity, Fig. 4.22 (d) does not show all of the investigated strip separations.

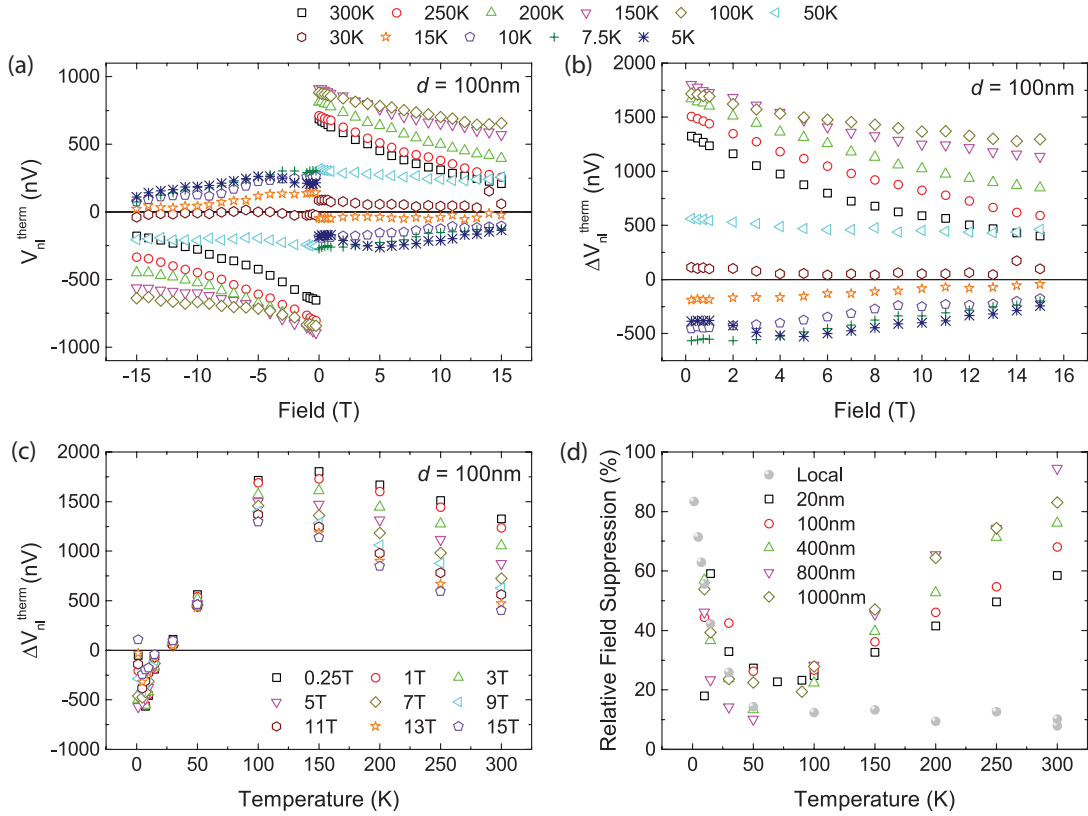


Figure 4.22: (a) Magnetic field sweeps for the spin Seebeck voltage signal on a 100 nm distant Pt strip for temperatures of 300 K down to 5 K. (b) Extracted non-local SSE amplitude ΔV_{nl}^{therm} from the field sweep data of panel (a). (c) Temperature dependence of ΔV_{nl}^{therm} for different external fields for the same device with $d = 100$ nm. (d) Relative field suppression versus temperature for the local SSE and certain distances of the non-local SSE.

of the optical branch at large distances with a long diffusion length. Unfortunately it is experimentally very difficult to distinguish between individual diffusion lengths of magnons at different energies, since we always measure a superposition of all thermally populated magnons. Still, in this case the observed temperature dependent field suppression for the local and non-local SSE is consistent with our model.

However, it is rather surprising that the suppression is even large for the shortest measured distance $d = 20$ nm ($\sim 60\%$ for $T = 300$ K), where the magnon diffusion process should have a minor impact on the temperature and field behaviour. Additionally, the acoustic magnons should contribute to the non-local signal for the short distance $d = 20$ nm, since their diffusion length is expected to exceed 20 nm. We would therefore expect a considerably lower field suppression for $d = 20$ nm, which is closer to the locally observed suppression of $\sim 10\%$ at 300 K. This discrepancy between model and experiment should be more thoroughly investigated in future work. Note further that in contrast to our data, the authors of Ref. [57] report an increase of the local SSE suppression with temperature by roughly $\sim 20\%$ from 30 K to 300 K, which fits well to our model.

4.3 Summary

In summary, we have investigated the resistive (Sect. 4.1) as well as the thermal response (Sect. 4.2) in local and non-local YIG|Pt devices.

The resistive response exhibits the typical SMR fingerprint in the local signal [18,19] and the MMR signal in the non-local Pt strip [12,13]. The temperature dependence of the non-local (MMR) signal shows different quantitative evolutions for different strip separations d , but vanishes for all distances at $T = 10$ K within the experimental resolution [13]. We have further argued (in Sect. 4.1.1) that the magnon excitation energy is not governed by the interface electron spin accumulation μ_s , but rather by the thermal energy $k_B T$ present in the system.

An important part of the work in this Chapter was the detailed investigation of the magnetic field dependence of the MMR. Hereby we postulated a qualitative model for the field dependence by taking into account the fundamental acoustic and high energy optical magnon modes of YIG [48]. Due to a different chirality of the high energy optical mode compared to the fundamental acoustic mode, a counteracting MMR signal generation is expected from the optical magnons. The optical mode is populated at high temperatures and becomes even more populated for larger magnetic fields due to the field induced downshift of the optical branch [51]. Based on these properties of the YIG magnon spectrum, we gave a qualitative model of the field dependence of the MMR in Fig. 4.7. This model was validated by the measurement of a non-local device with $d = 1 \mu\text{m}$, which shows a signal inversion at high temperatures and large magnetic fields, corroborating the impact of the optical mode.

A second important set of data taken in this Chapter relates to the impact of the Pt strip separation. We could convincingly strengthen our model for the MMR field dependence (which takes into account the optical magnon mode) by separately plotting the temperature and field dependence of the prefactor $V_{\text{nl}}^0(T, B)$ and the diffusion length $\lambda_m(T, B)$ of the fit function for the distant dependent MMR data (c.f. Eq. 4.5). Thereby we were able to distinguish quantitatively between temperature and field dependencies arising from either the magnon population or the magnon transport (see Figs. 4.10 and 4.13).

Regarding the thermal contribution, the well-known spin Seebeck effect in the local signal as well as a non-local thermal contribution were measured. We introduced two different scenarios for the non-local SSE, based on either pure heat transport between Pt strips or diffusion of thermally excited magnons from the heated Pt strip. For both scenarios the sign of the signal amplitudes is expected to be opposite to the sign of the local amplitude.

For the distance dependent data of the non-local SSE signal we found that the signal reveals a sign change at a certain strip separation distance d_0 . The positive sign for short distances is consistent with the sign of the local SSE, while it is reversed (negative) for large distances. We found that the critical distance d_0 strongly depends on temperature and YIG-thickness. The data was compared to a recent theory on the sign change of the non-local SSE put forward by Cornelissen et al. (see Ref. [33]). This model is based on a thermally generated distribution of the magnon accumulation μ_m in YIG, which is negative around the local strip and becomes positive farther away, changing sign in between. The negative (positive) magnon accumulation then gives rise to a positive short-

distance (negative long-distance) SSE signal. In order to explain our data, the increase of d_0 with increasing temperature was described in terms of an increase of the magnon spin conductivity σ_m with increasing temperature [31].

Besides the sign change of the non-local SSE, the temperature dependence of the local and non-local SSE showed qualitatively similar behaviour down to ~ 50 K. Since the temperature dependence of the local SSE is already reported in Ref. [57] and attributed to the magnon propagation length ξ , we concluded that the temperature dependence of the non-local signal can be explained in the same manner with the magnon diffusion length λ_m . We attributed the difference of ξ and λ_m to the difference between 1D and 2D diffusion, respectively (and especially to the different boundary conditions for a 1D and 2D measurement configuration). Since it is crucial to take into account a magnon propagation length scale, we found strong evidence for the magnon diffusion to be the leading process for the non-local SSE.

Finally, we investigated the relative field suppression for the local as well as the non-local SSE. As for the MMR, we could apply the model introduced for the field dependence of the MMR (c.f. Fig. 4.7), i.e. the impact of the optical magnon branch, to the non-local SSE as well. The experimental results furthermore indicate that the optical magnons have a larger diffusion length compared to the acoustic ones.

Chapter 5

Magnon Logic in a Multiterminal YIG|Pt Nanostructure

In this Chapter, we extend the concepts introduced in Chap. 4 for the two strip YIG|Pt structure to a multiple strip device allowing for magnon logic operations in the form of a magnon based majority gate [61]. Sect. 5.1 characterizes the behaviour of the magnon mediated magnetoresistance (MMR) in a three strip device, while Sect. 5.2 focusses on the implementation of a majority gate using a four strip YIG|Pt nanostructure.

5.1 Characterization of a three Strip Device

We start with the characterization of a three strip YIG|Pt nanostructure shown schematically in Fig. 5.1 (a). An optical micrograph of the device is depicted in Fig. 5.1 (b), including the wiring scheme. All three Pt strips have a width of $w = 1 \mu\text{m}$ and an edge-to-edge distance of $d = 500 \text{ nm}$. The measurements discussed in the following are conducted at a temperature of 275 K (this temperature can be very well stabilized in the magnet cryostat systems variable temperature insert, minimizing temperature drift effects in the experiments) and an external field of $\mu_0 H = 1 \text{ T}$ is applied in the film plane, perpendicular to the strips, to ensure the magnon excitation and a finite non-local signal (see Sect. 2.4 for theory and Sect. 3.3 for experimental techniques).

5.1.1 One Injector, two Detectors

In a first set of measurements, we apply a charge current I_1 to injector 1 and measure the non-local voltage V_2 and V_3 at detector 2 and 3 simultaneously, as shown in Fig. 5.1 (b). The resulting current-voltage characteristic is shown in Fig. 5.1 (c) for V_2 and V_3 . As anticipated, the current-voltage characteristic is linear, since the non-local voltage detected via the inverse spin Hall effect is proportional to the number of excited magnons, which in turn is proportional to the injector current. As expected from the strip separation dependence of the MMR discussed in Sect. 4.1, the non-local voltage signal V_2 is higher than V_3 , since the detector strip 2 is closer to the injector strip 1 than detector strip 3.

As a next step, we investigate the influence of the electrical boundary conditions of detector strip 2. While the signal V_3 of the outer strip 3 is measured, strip 2 is either short-circuited, open-circuited or connected to a nanovoltmeter. According to the phenomenological model of Ref. [12] the non-local platinum strip can be assumed to be a perfect magnon sink, meaning that all magnons at a distance d from the injector should be fully absorbed. However, our measurements in Fig. 5.1 (d) show that an additional strip within the magnon diffusion path does not affect the signal V_3 at the outer strip,

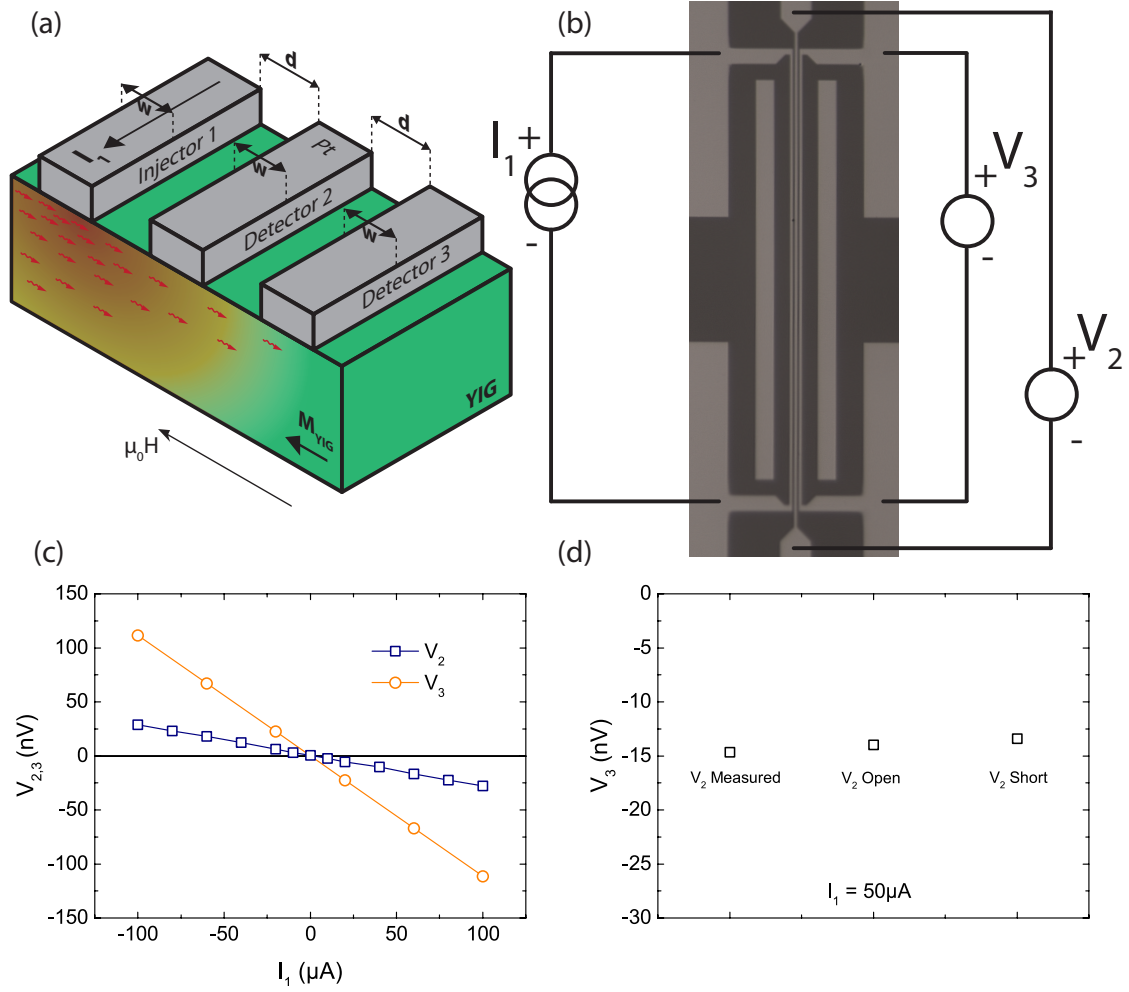


Figure 5.1: (a) Three strip YIG|Pt structure. A charge current I_1 is applied to injector 1, while the non-local voltages V_2 and V_3 are measured on detector 2 and 3. A magnetic field $\mu_0 H = 1$ T is applied in the film plane, perpendicular to the strips to ensure magnon excitation and a finite non-local signal. (b) Optical micrograph of the YIG (dark)|Pt (bright) structure with three equidistant Pt strips. A current source is attached to strip 1, while the voltage drop is measured across the detector strips 2 and 3 using nanovoltmeters. (c) V_2 and V_3 measured simultaneously, while applying different currents I_1 . (d) V_3 , detected at the detector strip 3 for different electrical boundary conditions at strip 2 and an injector current of $I_1 = 50 \mu\text{A}$.

independent of the electrical boundary conditions (short-circuited, open circuited or connected to nanovoltmeter). The detected non-local voltage V_3 is the same for all three measurement configurations of strip 2 within our experimental uncertainty of about 5 nV. Therefore we can state that the platinum, independent of electrical configuration, does not work as a perfect magnon sink¹.

¹The Pt coverage even seems not to impact the non-equilibrium magnon distribution in the YIG beneath within our experimental resolution.

5.1.2 Two Injectors, one Detector

We now address the superposition of magnons generated by different injectors. As shown in Fig. 5.2 (a) and (b), the two outer strips (1 and 3) are now used as injectors, while the center strip (2) works as a detector.

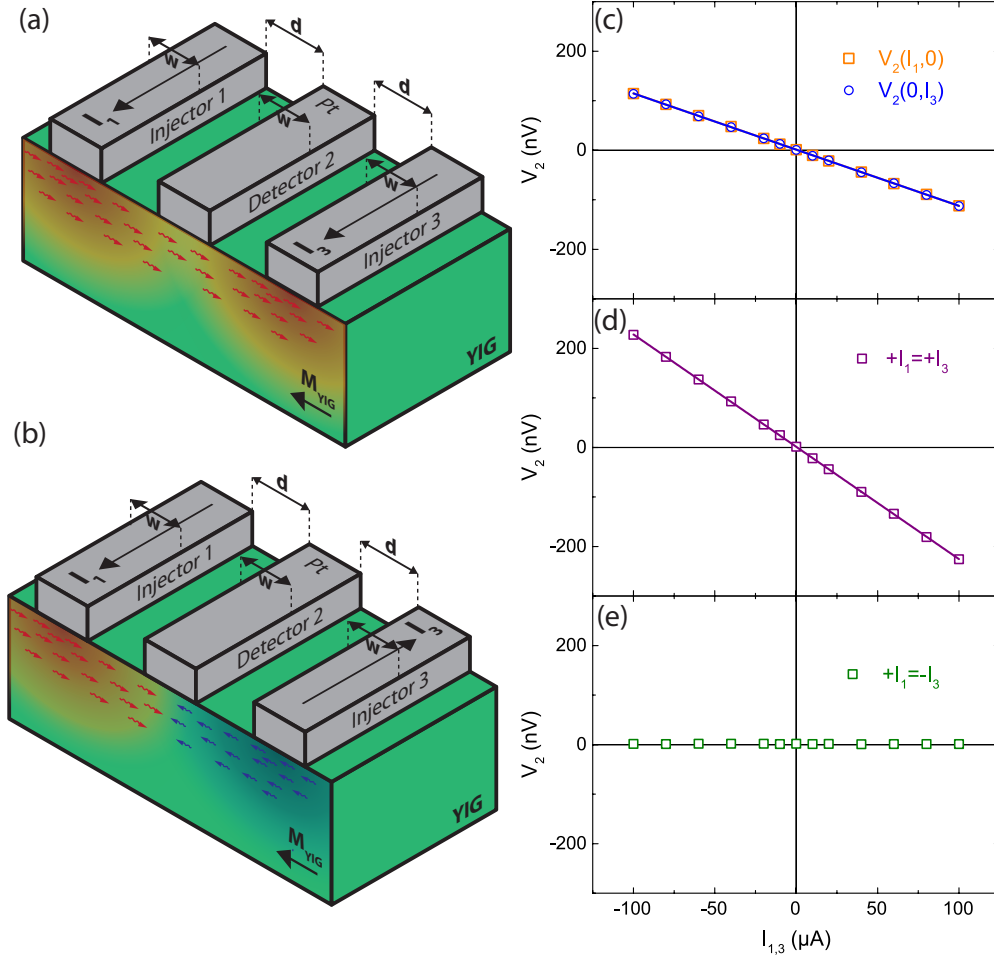


Figure 5.2: (a) Three strip YIG|Pt structure with parallel injector currents I_1 and I_2 . Note, that the arrows indicate the magnon polarization and not the diffusion direction, which we assume to be isotropic. Here, injector 1 and injector 3 generate magnons of the same polarization. At the detector strip 2 the diffusing magnons superimpose incoherently and generate a non-local voltage. (b) Three strip YIG|Pt structure with antiparallel injector currents. Injector 1 and 2 therefore generate magnons of opposing polarization in YIG. Since the non-local voltage at the detector is sensitive to the number of magnons as well as their polarization, the signal goes to zero when the current magnitudes are equal. (c) The detected voltage signal $V_2(I_1, 0)$ (orange open squares) when only injector 1 is current-biased, and $V_2(0, I_3)$ (blue open circles) when only injector 3 is driven, measured as a function of the applied current I_1 . The data is fitted linearly (blue and orange lines). (d) $V_2(I_1, I_3)$ when the injectors are driven with equal current directions and magnitudes. The purple line represents a linear fit. (e) Measured V_2 signal when the injectors are driven with currents of equal magnitude, but opposite polarity, resulting in the vanishing of the non-local voltage within our experimental error. Figure adapted from [61].

As already discussed in Sect. 2.4, we assume the magnons to have the same polarization \mathbf{m} as the magnetic moment of the original electron spin accumulation at the interface². We are therefore able to inject magnons of desired polarization by setting the polarity of the initial charge current, which in turn generates differently polarized interface spin accumulations. As a consequence, the polarity (sign) of the non-local voltage signal V_2 also changes sign with the injector current polarity. Note furthermore that the arrows in Fig. 5.2 (a) and (b) indicate the magnon polarization \mathbf{m} and not the diffusion direction, which we assume to be isotropic.

The non-local voltage $V_2(I_1, I_3)$ is measured as a function of the charge current I_1 (I_3) applied to strip 1 (strip 3). As evident from Fig. 5.2 (c), we observe $V_2(I_1, 0) = V_2(0, I_3)$ (blue open squares and orange open circles) within the experimental uncertainty of 5 nV, showing that the magnon generation efficiency of both injectors is identical. Quantitatively, we fit the data linearly with $V_2(I_1, 0) = \alpha_1 \cdot I_1$ and $V_2(0, I_3) = \alpha_3 \cdot I_3$ (blue and orange line) and extract the corresponding fit parameters $\alpha_1 = -1.140 \text{ m}\Omega \pm 0.002 \text{ m}\Omega$ and $\alpha_3 = -1.140 \text{ m}\Omega \pm 0.003 \text{ m}\Omega$. Thereafter, we apply charge currents of the same polarity $I_1 = I_3$ simultaneously to injectors 1 and 3, leading to the generation of magnons of the same polarization, which diffuse to detector strip 2. This is depicted in Fig. 5.2 (a). We find that the magnons from both injectors superimpose and generate a non-local voltage, as shown in Fig. 5.2 (d) (purple open squares). The linear fit (purple line) with a slope of $\alpha_{1+3} = -2.270 \text{ m}\Omega \pm 0.003 \text{ m}\Omega$ agrees nicely with $\alpha_{1+3} = \alpha_1 + \alpha_3$. These results indicate that the observed non local voltage originates from an incoherent superposition of magnons generated by different injectors. This is confirmed by the measurement shown in Fig. 5.2 (e), which shows the detector signal V_2 for injector currents $I_1 = -I_3$ of opposite polarity (green open squares). The oppositely polarized magnon accumulations arising from injector currents $I_1 = -I_3$ are illustrated in Fig. 5.2 (b). A linear fit to the data in Fig. 5.2 (e) shows a slope of $\alpha_{1-3} = -0.003 \text{ m}\Omega \pm 0.001 \text{ m}\Omega$, such that $\alpha_{1-3} = \alpha_1 - \alpha_3$ within our experimental uncertainty. In addition to the measurements shown in Fig. 5.2, the linearity as well as the incoherent superposition was also checked for $I_1 \neq I_3$, as well as for injecting different combinations of current magnitudes to strips 1 and 2 (data not shown here), confirming that $V_2(I_1, I_3) = \alpha_1 \cdot I_1 + \alpha_3 \cdot I_3$.

5.2 Magnon-based Majority Gate

With these properties in mind, we can implement a so called majority gate with three inputs and one output. The essential property of a majority gate is that the output always displays the majority of its logic inputs. Furthermore one input can be used as a control channel to switch between AND and OR operations, allowing for multiple logic operations in one and the same device. For the realization of the majority gate, a fourth Pt strip is added to the three strip device shown in Fig. 5.1 (a). This four strip device is schematically depicted in Fig. 5.3 (a), where the additional strip is designated as the control strip "C". All strips have a width $w = 500 \text{ nm}$ and the same edge to edge distance $d = 500 \text{ nm}$. An optical micrograph of the structure is shown in 5.3 (b), including the wiring scheme. The strips are labelled with "control C" (control channel), "injector 1", "injector 2" and "injector 3" from left to right. For the implementation of a majority gate, the control channel, as well as strip 1 and 3 are used as inputs (magnon injectors) and strip 2 is the

²Recall that the spin is oppositely oriented to its magnetic moment, $\mathbf{s} = -\mathbf{m}$.

output (magnon detector), where the non-local signal V_2 is measured. As shown in Sect. 4.1 and Sect. 5.1.2, a positive (negative) charge current applied to the inputs generates a negative (positive) non-local voltage at the output. We define the logical 1 and 0 at the inputs as positive current and negative current, respectively. Therefore a negative non-local voltage detected at strip 2 is defined as a logical 1, a positive one as a logical 0. If the inputs 1 and 3 inject the same number of magnons of opposite polarization, the detector signal vanishes³. In this case, the control channel works as its name says and injects either a logical 1 or 0.

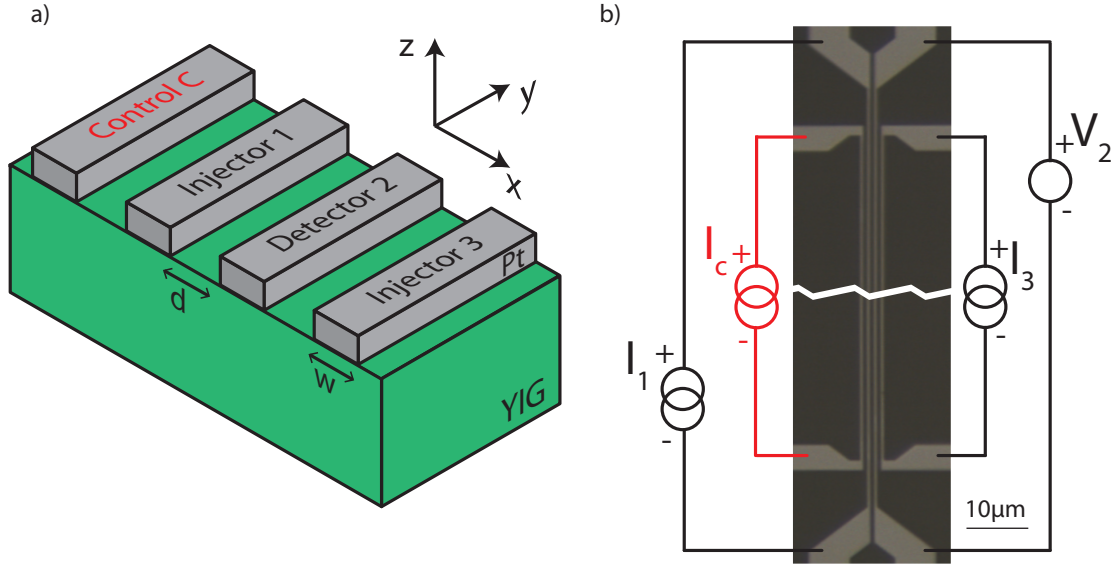


Figure 5.3: (a) Schematic of the 4 strip YIG|Pt device. Strips are labelled with C (control), 1 (injector), 2 (detector) and 3 (injector). (b) Optical micrograph of the YIG (dark)|Pt (bright) pattern. Strips C, 1 and 3 are attached to current sources. The non-local voltage at detector strip 2 is measured with a nanovoltmeter. Figure taken from [61].

³Note that the non-local voltage is sensitive to the number and polarization of the magnons accumulating beneath the injector. Since the magnon accumulation decreases exponentially for larger injector-detector separations, the strip separation needs to be taken into account as well. This is however not necessary in our device, as both injectors 1 and 3 are equidistant from the detector.

Control C	Injector 1	Injector 3	Detector 2
1	1	1	1
1	0	1	1
1	1	0	1
1	0	0	0
0	1	1	1
0	0	1	0
0	1	0	0
0	0	0	0
I_c	I_1	I_3	V_2
+	+	+	-
+	-	+	-
+	+	-	-
+	-	-	+
-	+	+	-
-	-	+	+
-	+	-	+
-	-	-	+

Table 5.1: Truth table of a majority gate (Ref. [62]). The bottom half of the table shows the sign of the bias currents for the input channels as well as the sign of the resulting non-local voltage V_2 in an MMR based majority gate. Positive and negative bias currents in the injectors are defined as logical "1" and "0", respectively. Since a positive bias current in the injector yields a negative non-local voltage V_2 (Ref. [13]), we define $V_2 < 0$ as "1" and $V_2 > 0$ as "0". Table taken from [61].

The input of the control channel is marked in red and set to either "1" for an "OR" operation or "0" for an "AND" operation.

It is furthermore important to focus on the signal amplitude in more detail. The observed signals with control channel currents of $I_c = 100 \mu\text{A}$ are in the range of a few 100 nV. For applications, it is of great interest to increase the signal to obtain a reasonable signal-to-noise ratio, even with low injector currents. In fact, it would be even desirable to obtain enough non-local voltage at the output to drive a further logic device. To increase the signal, the interconversion processes of spin currents to electrical currents and vice versa in the normal metal (Pt in the device discussed here) need to be optimized. This interconversion is parameterized by the spin Hall angle Θ_{SH} . Since the detector signal is proportional to Θ_{SH}^2 , new materials with a large spin Hall angle ($\Theta_{\text{SH}} \gg 1$ has been reported in topological insulators [63], while $\Theta_{\text{SH}} = 0.11$ in Pt [19]) can potentially significantly increase the detected non-local voltage, making corresponding devices more suitable for applications. A second important aspect are high switching frequencies. For the MMR, the relevant time scale is governed by the SHE-induced interface spin accumulation and the magnon transport through YIG. It has been shown experimentally that the spin Hall effect induced spin accumulation persists up to frequencies of at least a few GHz

Table 5.1 is the truth table for a majority gate. The upper part represents the logic table for all inputs and the detector output, while the bottom part shows the polarity of the corresponding injector currents and the detector voltage V_2 . The magnitudes of the input currents I_c , I_1 and I_3 are always assumed to be the same, while the exact magnitude of the detected voltage signal V_2 is dependent on the actual input configuration. Figure 5.4 illustrates the performance of the gate and shows experimental data with the respective logic inputs for two different injector currents.

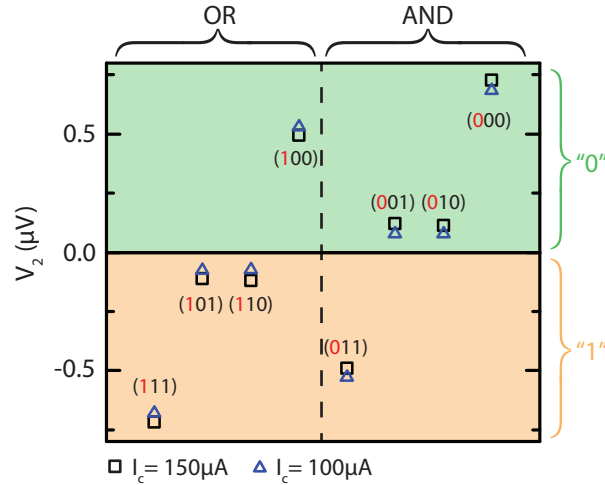


Figure 5.4: Measurement of the four-strip majority gate. The detected non-local voltage V_2 is depicted for different input signals ($I_c I_1 I_3$), where the bit of the control channel is marked in red. The magnitudes of the injector currents I_1 and I_3 are kept constant, and V_2 is measured for control current magnitudes $I_c = 150 \mu\text{A}$ and $100 \mu\text{A}$ (black and blue symbols). The experimental data faithfully reproduces all the properties of a majority gate. Figure taken from [61].

corresponding to spin accumulation build up times well below a nanosecond [64]. For the magnon transport the limiting quantity is their propagation velocity, which is in the order of $1 \mu\text{m ns}^{-1}$ [65]. For the device shown in Fig. 5.3 (a) this leads to a lower limit of 2 ns and a switching frequency of $f = 1/T = 500 \text{ MHz}$, assuming the center-to-center distance of $d = 2 \mu\text{m}$ from the control channel to the detector. Technically, it is straightforward to reduce the width of the Pt strips down to 50 nm (or even smaller) and hence their center-to-center separation to 100 nm (or smaller), yielding a factor 10 increase of the switching frequency, to several GHz. Furthermore, the downscaling provides remarkably higher detection signals, since the signal is decaying exponentially with distance [12]. This eventually requires even lower bias currents for a proper device performance. Since the logical bit is encoded in the polarization of the generated magnons and not in the frequency, phase, or amplitude of the spin waves, down-scaling does not perturb the functionality of the logic gate.

In summary, in this Chapter we have characterized the MMR in YIG|Pt nanostructures with multiple injector strips. We demonstrated that the magnons generated by different injectors superimpose incoherently and showed that an additional Pt strip within the magnon diffusion path has no detectable effect on the non-local voltage. Furthermore a proof of principle 4-strip majority gate was introduced, with which we were able to perform standard bitwise logic operations such as "AND" and "OR". Thereby bits are encoded in the polarization of magnons, that can be chosen by the polarity of the injector currents. The majority gate concept was published in Appl. Phys. Lett. 109, 022405 (2016) [61] during the course of this thesis.

Chapter 6

Non-local Spin Transport in GIG|Pt Nanostructures

The influence of different magnon modes and their chirality on the spin Seebeck effect has already been studied in Gadolinium-Iron-Garnet ($\text{Gd}_3\text{Fe}_5\text{O}_{12}$, GIG) [67]. However, the diffusion of either electrically or thermally excited magnons has not been studied in GIG up to now. In this Chapter we take a first glance at the diffusive magnon transport in Gadolinium-Iron-Garnet|Platinum (GIG|Pt) devices (c.f. Sect. 3.1). As described in Sect. 3.2, the Pt layers are patterned into two parallel, isolated platinum strips with different strip separations d . As the GIG film exhibits a very rough surface, only two different devices with strip distances $d = 200$ nm and $d = 500$ nm and strip widths $w = 500$ nm were functional and could be studied. Two different injector currents $I = 50$ μA and $I = 100$ μA are applied to the injector strips, while the respective resistive (thermal) non-local voltage $V_{\text{nl}}^{\text{res}}$ ($V_{\text{nl}}^{\text{therm}}$) are measured at the detector strip (c.f. Sect. 3.3). In addition to this, the local resistive (thermal) voltage $V_{\text{loc}}^{\text{res}}$ ($V_{\text{loc}}^{\text{therm}}$) are simultaneously measured at the injector strip in a 4-point measurement configuration (c.f. Sect. 3.3).

For the detailed characterization, in plane ADMR rotations with fields up to 15 T are conducted in a temperature range of $5 \text{ K} < T < 300 \text{ K}$. Additionally, we performed "max/min" measurements, i.e. measuring the local and non-local voltage signals for in plane field directions along (max) and perpendicular (min) to the Pt strips,

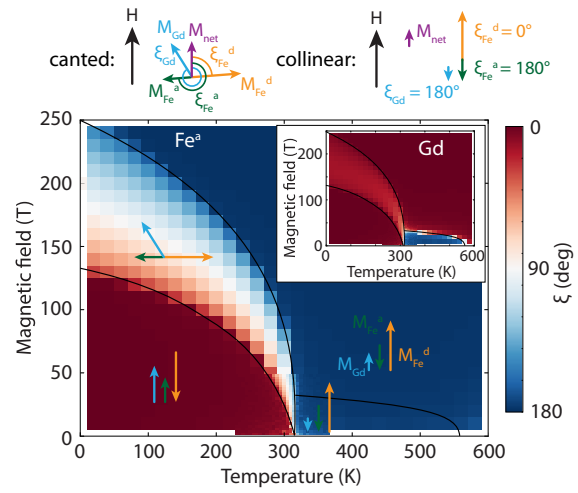


Figure 6.1: Magnetic phase diagram of GIG calculated by atomistic spin simulations (see Ref. [66] for details). The solid black lines mark the boundaries between magnetic phases with different magnetic sublattice structure, which are determined by the temperature dependencies of the upper ($\mu_0 H_{c2}$) and lower ($\mu_0 H_{c1}$) critical fields. The color code shows the relative angle $\xi_{\text{Fe}^a}^a$ of the sublattice magnetization $\mathbf{M}_{\text{Fe}^a}^a$ with respect to the direction of the external field \mathbf{H} , while the inset shows the same for ξ_{Gd}^a of the Gd sublattice. Due to the strong antiferromagnetic coupling, the Fe^a and Fe^d iron moments are antiparallel. For each phase, the corresponding sublattice orientations are indicated by arrows. Figure adapted from [66].

allowing for a quick evaluation of the amplitudes of both the resistive and thermal signals, without conducting a full rotation.

For the following discussions, a profound understanding of the magnetic phase diagram of GIG is required. As described in Sect. 3.1, GIG exhibits two antiferromagnetically coupled iron sublattices ($\mathbf{M}_{\text{Fe}}^{\text{d}}$ and $\mathbf{M}_{\text{Fe}}^{\text{a}}$, similar to YIG) and an additional sublattice magnetization from the Gd atoms \mathbf{M}_{Gd} . The temperature- and field-dependent magnetic phase diagram of GIG, obtained from atomistic spin calculations in Ref. [66], is shown in Fig. 6.1. The color code represents the relative angle $\xi_{\text{Fe}}^{\text{a}}$ of the sublattice magnetization $\mathbf{M}_{\text{Fe}}^{\text{a}}$ with respect to the direction of the external field \mathbf{H} . Note that this angle is an average over all the magnetic moments of the corresponding sublattice. The antiferromagnetic coupling is strong, such that $\xi_{\text{Fe}}^{\text{a}} = \xi_{\text{Fe}}^{\text{d}} + 180^\circ$ always holds. The inset shows the magnetic phase diagram with the color plot representing the relative orientation ξ_{Gd} of the Gd magnetization \mathbf{M}_{Gd} . Moreover, the solid black lines depict the phase boundaries, at which the sublattice magnetizations reorient to minimize the total energy in the system. Above the compensation temperature $T_{\text{Comp}} \approx 300$ K and low magnetic fields the net iron moment $\mathbf{M}_{\text{Fe}}^{\text{net}} = \mathbf{M}_{\text{Fe}}^{\text{d}} - \mathbf{M}_{\text{Fe}}^{\text{a}}$ points parallel to the external field \mathbf{H} , while the Gd moment \mathbf{M}_{Gd} is antiparallely aligned to \mathbf{H} . An increase of the external field gives rise to a depolarization of the Gd moments, which causes the horizontal phase boundary (solid black line for ~ 300 K $< T < \sim 560$ K) above T_{Comp} in Fig. 6.1. Beyond this phase boundary at high magnetic fields, the Gd moment \mathbf{M}_{Gd} is aligned along the external field, while the configuration of the iron moments is unchanged. At T_{Comp} the compensated ferrimagnet enters the spin canting phase, where the sublattice magnetizations enclose angles $\xi_{\text{Fe}}^{\text{a,d}} \neq \xi_{\text{Gd}} \neq 0^\circ, 180^\circ$ with the external field \mathbf{H} . The spin canting phase becomes broader and shifts to lower temperatures with increasing field strength. Below T_{Comp} another collinear phase is present, where the net iron moment $\mathbf{M}_{\text{Fe}}^{\text{net}}$ points against the external field, while the Gd moment \mathbf{M}_{Gd} is parallelly aligned to \mathbf{H} .

In the following, local and non-local signals are investigated in terms of their resistive contribution in Sect. 6.1 as well as their thermal contribution in Sect. 6.2.

6.1 Resistive Contribution

The electrical injection of magnons (the MMR, c.f. Sect. 2.4) was found to be strongly affected by the thermal magnon population in YIG in Sect. 4.1. In this context, we found that the acoustic and optical mode of the magnon spectrum (arising from the two sublattice magnetizations) have a visible impact on the MMR. Hence, the investigation of the MMR in the compensated insulating ferrimagnet Gadolinium-Iron-Garnet (GIG) with an even more complex three sublattice-magnetization structure (c.f. Chap. 3) and the accompanying complex magnon spectrum is of great interest [67]. In addition to the complex magnon spectrum, GIG also yields a magnetic phase diagram with transitions from collinear to canted phases. It has been shown that SMR measurements can be used to map out these magnetic phases, suggesting that the orientation of the individual magnetic sublattices is relevant for the spin transfer torque [66]. This conclusion is manifested in the sign change observed for the SMR in GIG/Pt around the magnetic compensation temperature T_{Comp} reported in Ref. [66], indicating that the net iron moment $\mathbf{M}_{\text{Fe}}^{\text{net}}$ of GIG is dominantly responsible for the SMR, since $\mathbf{M}_{\text{Fe}}^{\text{net}}$ is roughly oriented perpendicular to the external field \mathbf{H} in the spin canting phase (see Fig. 6.1). This 90° phase shift of

the net iron sublattice magnetization gives rise to the sign change (which corresponds to a 90° phase shift of the magnetic field orientation dependent SMR modulation) of the SMR around T_{Comp} . In this Section, we study the impact of the canting phase on the MMR, which is based on the electrical generation and detection of magnons. Moreover, the antiferromagnetically coupled net iron magnetization $\mathbf{M}_{\text{Fe}}^{\text{net}}$ and Gd magnetization \mathbf{M}_{Gd} in GIG reorient and exchange roles around the compensation temperature T_{Comp} (see Chap. 3), which gives rise to interesting field and temperature dependencies of the MMR.

The temperature dependence of the local (SMR) and non-local (MMR) resistive signals is investigated in Sect. 6.1.1, while we focus on the magnetic field dependence in Sect. 6.1.2.

6.1.1 Temperature Dependence

All experimental data shown in this Section is conducted at a magnetic field $\mu_0 H = 1$ T. Prior to the non-local MMR, we focus on the temperature dependence of the local resistive SMR voltage signal $V_{\text{loc}}^{\text{res}}$ of the GIG|Pt devices. Magnetic field orientation dependent modulations of the SMR voltage signal $\frac{V_{\text{loc}}^{\text{res}}}{V_0}$ (normalized to the maximum voltage level V_0 , c.f. Sect. 4.1) are shown in Fig. 6.2 (a) for different temperatures measured on a device with $d = 200$ nm and $w = 500$ nm and an applied injector current $I = 100$ μA . The field rotations are shown for temperatures around the compensation temperature $T_{\text{Comp}} \approx 268$ K and a low temperature $T = 10$ K. We find that the SMR amplitude is roughly equal well above and well below T_{Comp} , whereas it is highly suppressed around the compensation temperature (see measurement for $T = 270$ K in Fig. 6.2 (a)). Down to low temperatures $T = 10$ K, the SMR amplitude decreases, which is consistent with the decrease of the SMR observed in YIG|Pt heterostructures [41]. The ADMR data are fitted with $\Delta V_{\text{loc}}^{\text{res}} \cos^2(\alpha)$ and the amplitude $\Delta V_{\text{loc}}^{\text{res}}$ is extracted. The SMR ratio is then calculated as $\frac{\Delta V_{\text{loc}}^{\text{res}}}{V_0}$ and plotted as a function of temperature in Fig. 6.2 (b). The graph additionally shows SMR ratios extracted from max/min measurements and ADMR measurements with an applied current $I = 50$ μA ("Amp" and "ADMR", respectively, in Fig. 6.2 (b)). Note that the current amplitude has no visible impact on the SMR amplitude and temperature dependence, indicating that additional heating at $I = 100$ μA can be neglected. For $T < T_{\text{Comp}}$, the SMR ratio decreases roughly by a factor of 2 from 250 K to 10 K, which is consistent with measurements in YIG|Pt [41]. Around T_{Comp} the SMR ratio vanishes, while a sign change of the SMR around T_{Comp} was reported in GIG|Pt bilayers in Ref. [66]¹. Note, however, that the sharp decrease (and vanishing) of the SMR signal close to T_{Comp} is qualitatively very similar in the sample studied here and in those of Ref. [66]. The only marked difference is the absence of a sign change in our GIG|Pt structure. According to Ref. [66], the sign change arises from the dominant net iron moment in the GIG, which exhibits an almost perpendicular configuration with respect to the external field in the spin canting phase (see Fig. 6.1). As a consequence, the maxima (or minima) of the ADMR modulations exchange roles, leading to a sign change of the SMR. The discrepancy between the measurements conducted in this work and Ref. [66] could be due to the imperfect surface quality of the GIG film, as mentioned in the

¹One may notice that in Fig. 6.2 (b) a single data point at $T = 268$ K $\approx T_{\text{Comp}}$ exhibits negative sign. However, this data point is extracted from a max/min measurement and is additionally very small in magnitude, which makes it less reliable compared to the amplitudes extracted from full rotations. Therefore this should be checked with an ADMR measurement at that temperature.

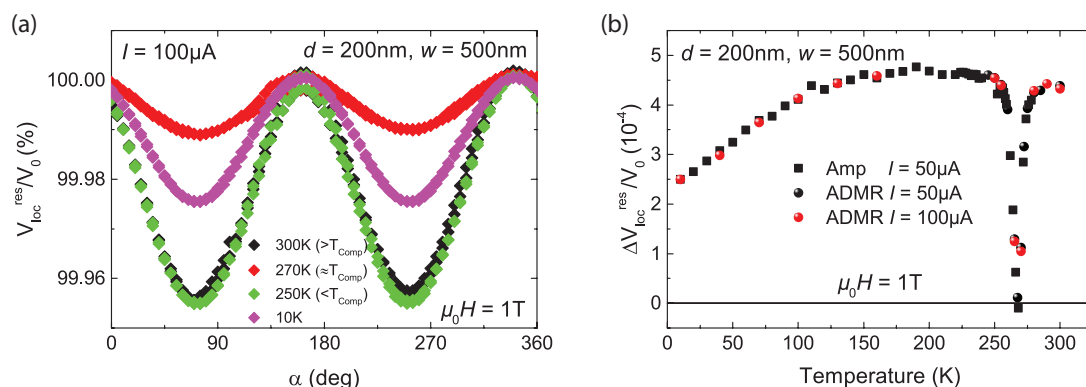


Figure 6.2: (a) Magnetic field orientation dependent SMR voltage modulations $\frac{V_{loc}^{res}}{V_0}$ for a device with $d = 200\text{ nm}$ and $w = 500\text{ nm}$ for $T = 300\text{ K} > T_{Comp}$, $270\text{ K} \approx T_{Comp}$, $250\text{ K} < T_{Comp}$ and $10\text{ K} \ll T_{Comp}$. The applied current and field strength is $I = 100\ \mu\text{A}$ and $\mu_0 H = 1\text{ T}$, respectively. (b) SMR ratio $\frac{\Delta V_{loc}^{res}}{V_0}$ plotted as a function of temperature. The SMR ratios are extracted from ADMR measurements with applied currents of $I = 100\ \mu\text{A}$ and $50\ \mu\text{A}$ and max/min measurements with $I = 50\ \mu\text{A}$.

beginning of this Chapter. More specifically, we speculate that at the rough GIG surface, the magnetic sublattice configuration in the spin canting phase close to T_{Comp} might be very different from the bulk. Since the calculations for the sign change of the SMR in Ref. [66] are based on the bulk sublattice magnetization orientations, they might only give a rough idea of the SMR arising from the rough GIG surface. Local shape anisotropies leading to complex demagnetization fields at the interface could thus be responsible for complex sublattice magnetization configurations, which may be distinctly different from the bulk. However, since this work focusses on the non-local magnon transport, we do not go into further detail regarding the temperature dependence of the SMR.

The non-local voltage modulations are shown in Fig. 6.3 (a) for different temperatures around T_{Comp} for a device with strip separation $d = 200\text{ nm}$ and an applied current $I = 50\ \mu\text{A}$. Similar to the SMR, the MMR signal is roughly equal for temperatures well above and well below T_{Comp} , while it vanishes at T_{Comp} . Furthermore, the signal is considerably lower for $T = 50\text{ K}$. We further evaluate the temperature dependence of the MMR by extracting the amplitudes ΔV_{nl}^{res} from ADMR modulations as well as from max/min measurements for an injector current $I = 50\ \mu\text{A}$ and $I = 100\ \mu\text{A}$ and two different devices with distance $d = 200\text{ nm}$ and $d = 500\text{ nm}$, as shown in Fig. 6.3 (b).

First of all, the voltage signals reproduce the linear scaling with the injector current, since the signal increases by a factor of 2 when the current is increased from $I = 50\ \mu\text{A}$ to $I = 100\ \mu\text{A}$ [12]. Additionally, the voltage amplitudes decrease with increasing strip distance, which is expected for a diffusive magnon transport through the GIG (c.f. Sect. 4.1). Moreover, the MMR signal vanishes at low temperature $T = 10\text{ K}$ within our experimental uncertainty of 5 nV . This is consistent with MMR measurements in YIG/Pt [13], which further suggests the dominance of thermal magnons for the MMR (c.f. Sect. 4.1). For $T > 10\text{ K}$, the signal increases with increasing temperature, but exhibits a plateau for approximately 100 K to 125 K . The vanishing signal at T_{Comp} , where GIG enters the spin canting phase, is similar to the temperature behaviour observed for the SMR in Fig. 6.2

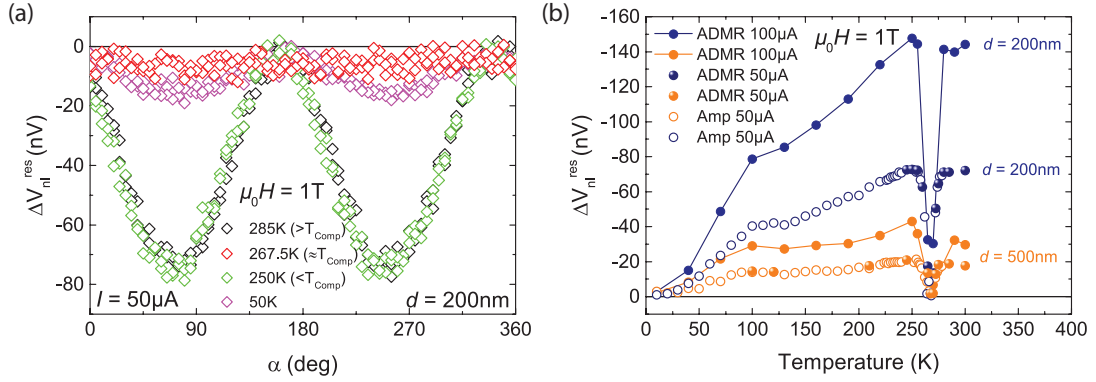


Figure 6.3: (a) ADMR modulations of the MMR voltage signal V_{nl}^{res} for a device with $d = 200 \text{ nm}$ and $w = 500 \text{ nm}$ for $T = 285 \text{ K} > T_{\text{Comp}}$, $267.5 \text{ K} \approx T_{\text{Comp}}$, $250 \text{ K} < T_{\text{Comp}}$ and $50 \text{ K} \ll T_{\text{Comp}}$. The applied current and field strength is $I = 50 \mu\text{A}$ and $\mu_0 H = 1 \text{ T}$, respectively. (b) MMR voltage amplitude $\Delta V_{nl}^{\text{res}}$ plotted as a function of temperature for devices with strip separation $d = 200 \text{ nm}$ and $d = 500 \text{ nm}$. The MMR amplitudes are extracted from ADMR measurements (full symbols) and from max/min measurements ("Amp", open symbols) with injector currents $I = 50 \mu\text{A}$ and $I = 100 \mu\text{A}$.

(b). We therefore conclude that the individual sublattice magnetizations at the interface, which cause the local SMR signal to vanish, give rise to a vanishing MMR signal as well. In order to investigate the influence of the canting phase on the MMR in more detail, the non local MMR should be studied in an additional GIG|Pt sample which exhibits a SMR sign change at T_{Comp} as predicted for a "clean" canting phase (similar to Ref. [66]). As discussed in Ref. [66], the SMR is governed by the strongly antiferromagnetically coupled iron sublattices $\mathbf{M}_{\text{Fe}}^{\text{d}}$ and $\mathbf{M}_{\text{Fe}}^{\text{a}}$, which are roughly perpendicular to the external field in the spin canting phase (see Fig. 6.1) and therefore lead to a 90° phase shift (i.e. sign change) of the SMR signal. Assuming that the orientation of the Fe sublattices also governs the MMR, the MMR signal should also exhibit a phase shift of roughly 90° due to the reorientation of sublattice magnetizations in the spin canting phase.

We further emphasize that in contrast to the local SSE signal in GIG|Pt [67] (c.f. Sect. 6.2.1), the MMR voltage does not change sign around T_{Comp} . This is due to the fact that the sign change of the SSE is induced by the inversion of the spin quantization axis at the compensation temperature (caused by the reorientation of magnetizations) [67], which does not affect the MMR, which scales as \mathbf{M}^2 . Contributions from magnon modes with different chiralities, however, might be able to change the absolute sign of the MMR, as indicated in the MMR measurements in YIG|Pt in Sect. 4.1.2. Within the spin canting phase, the magnon spectrum is likely to be rather different. Therefore, the absolute sign of the MMR voltage signal V_{nl}^{res} in this case depends on how the thermal population of magnon modes with the corresponding $+/-$ chiralities (which we assume to generate opposite signs for the MMR signal) contribute to the MMR signal. For a collinear magnet such as YIG, the MMR was found to be dominated by the fundamental mode of the magnon spectrum (c.f. Sect. 4.1), which one can naively relate to the net magnetization of YIG. For a canted magnet such as GIG, however, it is very difficult to predict the prevalent magnon spectrum in the canted phase. Thus, more detailed future experiments of the MMR in complex magnets appear very interesting.

6.1.2 Magnetic Field Dependence

We proceed with the magnetic field dependence of the resistive response in GIG|Pt bilayers. Firstly, the SMR response is studied for different magnetic fields. In Figure 6.4 (a) the normalized voltage signal $\frac{V_{loc}^{res}}{V_0}$ is shown as a function of magnetic field orientation for $\mu_0 H = 1$ T, 3 T, 5 T and 7 T at $T = 255$ K with an applied current of $I = 100 \mu\text{A}$. The SMR ratio $\frac{\Delta V_{loc}^{res}}{V_0}$ is then extracted from ADMR measurements with injector currents $I = 50 \mu\text{A}$ and $I = 100 \mu\text{A}$, as well as from max/min measurements with $I = 50 \mu\text{A}$ for all measured fields and temperatures. The result is shown in Fig. 6.4 (b). For the majority of the temperature range, no significant field dependence can be observed. This weak field dependence of the SMR is consistent with the field-independent macrospin-based theory of Ref. [20]. However, a slight SMR enhancement with increasing field strength is still evident. Around the compensation temperature T_{Comp} , as well as at the lowest measured temperature $T = 10$ K, the field-induced enhancement of the SMR is larger. The slight enhancement with increasing field strength for the SMR was already discussed in Sect. 4.1.2 for YIG|Pt, where we took into account a possible magnonic contribution to the SMR. The more pronounced field dependence around T_{Comp} may therefore be attributed to the more sensitive magnetization structure in vicinity to the phase boundary around T_{Comp} , which gives rise to a stronger population of magnons due to larger fluctuations in the magnetization. As a consequence thereof, an increasing magnetic field is able to depopulate these magnons efficiently by the spin wave gap. Provided that we assume a magnon contribution to the SMR, the field-induced efficient depopulation of magnons (disturbing the collinearity of the magnetization) is expected to enhance the SMR ratio more pronounced around T_{Comp} , compared to temperatures which are conspicuously different to T_{Comp} .

Subsequently, we give a detailed study of the magnetic field dependence of the non-local MMR in GIG|Pt hybrid structures. Magnetic field rotations up to $\mu_0 H = 7$ T are shown for $T = 300$ K $> T_{Comp}$ for the device with $d = 200$ nm and current $I = 100 \mu\text{A}$

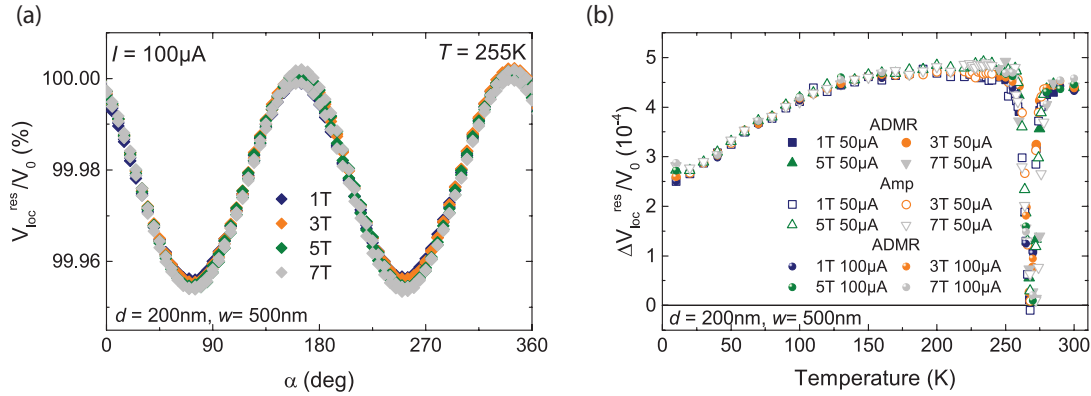


Figure 6.4: (a) Magnetic field rotations of the normalized SMR voltage $\frac{V_{loc}^{res}}{V_0}$ for fields up to $\mu_0 H = 7$ T at $T = 255$ K $< T_{Comp}$, measured for a device with $d = 200$ nm, $w = 500$ nm and an applied current $I = 100 \mu\text{A}$. (b) SMR ratio $\Delta \frac{V_{loc}^{res}}{V_0}$ as a function of temperature for the same device as in (a). The SMR amplitudes are extracted from ADMR modulations with applied currents $I = 50 \mu\text{A}$ and $I = 100 \mu\text{A}$ (full symbols), as well as from max/min measurements with $I = 50 \mu\text{A}$ (open symbols).

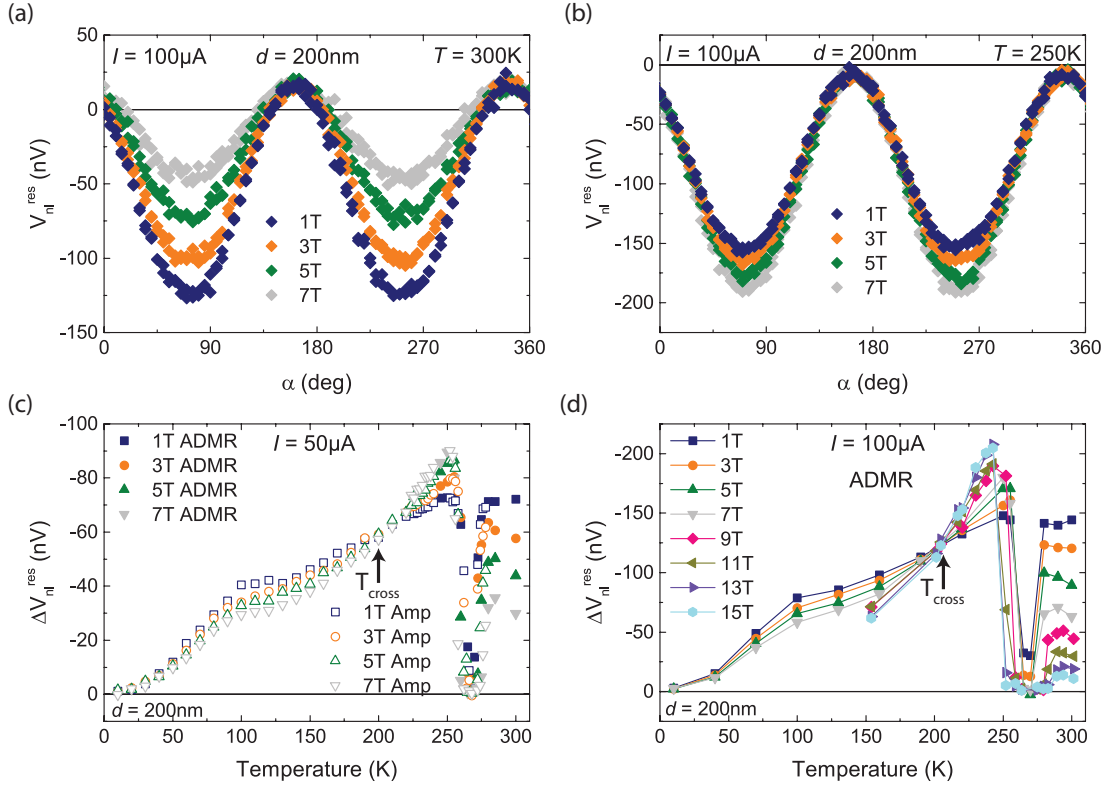


Figure 6.5: Magnetic field dependence of the MMR in GIG|Pt for a device with $d = 200$ nm. (a) Non-local resistive signal V_{nl}^{res} for $\mu_0 H = 1$ T, 3 T, 5 T and 7 T at $T = 300$ K $> T_{\text{Comp}}$ and (b) $T = 250$ K $< T_{\text{Comp}}$. (c) MMR amplitude $\Delta V_{nl}^{\text{res}}$ as a function of temperature for different magnetic fields. The amplitudes are extracted from ADMR measurements (full symbols) and max/min measurements (open symbols) for an applied current $I = 50 \mu\text{A}$. (d) MMR amplitude $\Delta V_{nl}^{\text{res}}$ for magnetic fields up to $\mu_0 H = 15$ T, extracted from ADMR measurements with injector current $I = 100 \mu\text{A}$.

in Fig. 6.5 (a). As expected, the signal amplitude is suppressed by the external field, since magnons are depopulated by the field-induced spin wave gap (c.f. Sect. 4.1.2). Figure 6.5 (b) shows ADMR modulations for the same field strengths as in panel (a) for $T = 250$ K $< T_{\text{Comp}}$. At this temperature slightly below T_{Comp} , the signal is enhanced with increasing field strength. This feature is puzzling, since the magnon spectrum is always expected to be depopulated with an external field. In order to acquire a more detailed picture of the evolution of the field dependence with temperature, the MMR signal amplitudes $\Delta V_{nl}^{\text{res}}$ are plotted for four different magnetic fields in Fig. 6.5 (c) for $I = 50 \mu\text{A}$ and $d = 200$ nm. The signals are extracted from ADMR measurements (full symbols) as well as from max/min measurements (open symbols). The field-induced enhancement slightly below $T_{\text{Comp}} = 268$ K decreases with decreasing temperature until the signal becomes independent of field at a temperature $T_{\text{cross}} \approx 205$ K. Thereafter, for $T < T_{\text{cross}}$ the signal is suppressed again, as expected from the MMR effect [44]. To see if the qualitative behaviour of the temperature dependent field suppression/enhancement remains at higher fields, ADMR measurements up to $\mu_0 H = 15$ T were carried out with an applied current $I = 100 \mu\text{A}$ for the temperature range 150 K $< T < 300$ K. The result

for $d = 200$ nm is plotted in Fig. 6.5 (d). The signal is still enhanced slightly below T_{Comp} up to 15 T, while it is strongly suppressed for $T > T_{\text{Comp}}$. Moreover, the region around T_{Comp} , where the signal is zero, becomes broader with increasing field strength. This is reasonable, since higher magnetic fields broaden the temperature range within the spin canting phase, as evident from the magnetic phase diagram of GIG in Fig. 6.1.

We proceed by calculating the relative field suppression for every temperature with

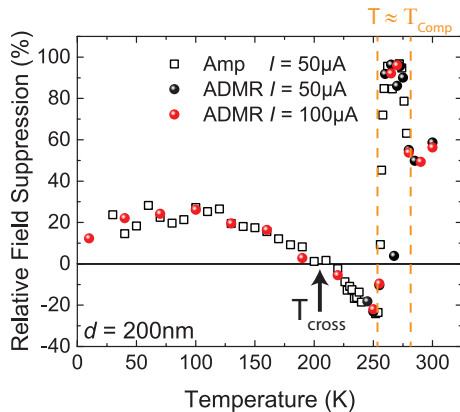


Figure 6.6: Relative field suppression of the MMR for the $d = 200$ nm device as a function of temperature calculated using Eq. 6.1. Negative values correspond to a field-induced enhancement.

$$\frac{\Delta V_{\text{nl}}^{\text{res}}(B = 1 \text{ T}) - \Delta V_{\text{nl}}^{\text{res}}(B = 7 \text{ T})}{\Delta V_{\text{nl}}^{\text{res}}(B = 1 \text{ T})}, \quad (6.1)$$

where 100 % correspond to complete suppression, while negative values correspond to a field-induced enhancement. The result of Eq. 6.1 is depicted in Fig. 6.6. We find that for $T = 300 \text{ K} > T_{\text{Comp}}$ the suppression reaches $\sim 60\%$. At $T \approx T_{\text{Comp}}$, the suppression reaches high values up to 100 %, since we then compare MMR signals in Eq. 6.1 within and out of the spin canting phase when the external field $\mu_0 H = 7 \text{ T}$ exceeds the lower critical field $\mu_0 H_{c1}$. For the temperature range $T_{\text{cross}} = 205 \text{ K} < T < 250 \text{ K}$, the signal is enhanced up to $\sim 25\%$. For temperatures

$T < T_{\text{cross}}$, the field suppression increases and becomes roughly constant for $T < 100 \text{ K}$, at approximately $\sim 20\%$.

In order to understand the complex field dependence of the MMR in GIG, we have to take into account the magnon spectrum of GIG. This is shown in Fig. 6.7 [68]. The fundamental mode below 1 THz corresponds to the ferrimagnetic resonance mode (α -mode). Around 1 THz, there are two almost dispersion-less modes, which correspond to the Gd moments precessing in the exchange field of the Fe-moments. The next approximately parabolic mode (β -mode) exhibits an energy gap Δ at $k = 0$, which is strongly dependent on the exchange coupling between the Fe and Gd moments [67]. Moreover, the β -mode (blue color) exhibits opposite chirality compared to the α -mode (red color) and the energy gap Δ of the β -mode decreases significantly with increasing temperature. This is due to the fact that the thermal fluctuations decrease the order in the Gd moments, which consequently decreases the Fe-Gd exchange coupling and lowers Δ [67]. Around 6 THz, a further parabolic acoustic mode (γ -mode) is situated, which also shifts down in the frequency spectrum with increasing temperature [48].

With these features of the magnon spectrum in mind, it is possible to give a qualitative explanation for the temperature evolution of the field dependence of the MMR in GIG/Pt, as illustrated schematically in Fig. 6.8. In the following, we combine the α -mode and the two flat Gd modes to an effective α_{eff} -mode, since all these modes are already populated for $T \approx 40 \text{ K}$ (c.f. Fig.6.7). Moreover, we assume that the α_{eff} -mode of the magnon spectrum with positive chirality (red color in Figs. 6.8 and 6.7) dominates the MMR signal for the whole temperature range up to 300 K, since we always observe the same absolute sign

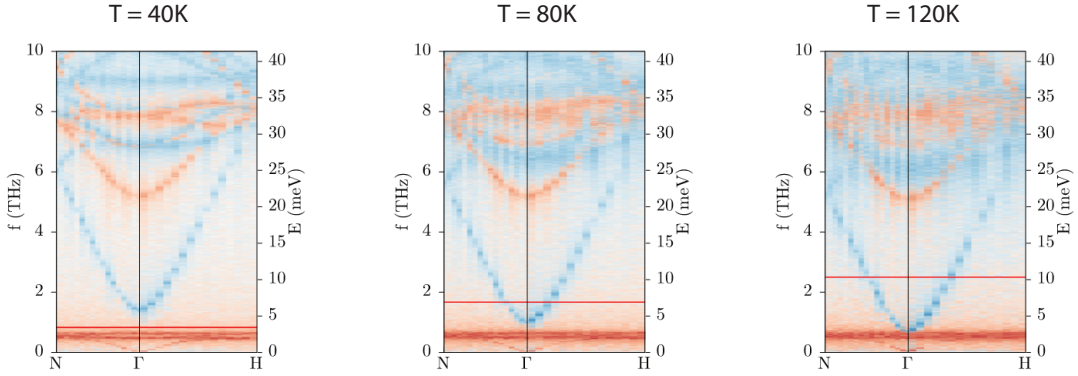


Figure 6.7: Dispersion relation of magnons in GIG for low temperatures, calculated by Joseph Barker (Tohoku University, Japan) [68]. Red and blue coloring denotes the $+/-$ chirality of the modes. The solid red lines represent the thermal energy $k_B T$. Up to $T = 40$ K the red colored modes with positive chirality govern the population of the magnon spectrum: a uniform precession mode in the GHz-regime (α -mode) and two almost dispersion-less modes at approximately 1 THz, which correspond to the Gd moments precessing in the exchange field of the Fe-moments. The next higher mode is a gapped optical mode (β -mode), precessing in opposite sense to the α -mode (blue color). For room temperature ($\hat{=} 6$ THz), even the parabolic red mode at higher energy (γ -mode) will be populated. Figure taken from [68].

of the MMR voltage $\Delta V_{\text{nl}}^{\text{res}}$ in Figs. 6.5 (c) and (d). On the left hand side of panel (a) in Fig. 6.8 the GIG magnon spectrum for a temperature $T \approx 300$ K $> T_{\text{Comp}}$ is schematically shown, where the net Fe moment $\mathbf{M}_{\text{Fe}}^{\text{net}}$ points parallel to the external field B , whereas the Gd moment \mathbf{M}_{Gd} is antiparallely oriented. All three modes (α_{eff} , β and γ) are thermally populated at $T \approx 300$ K. In addition to this, we assume a small, but finite gap Δ of the β -mode, even at room temperature². On the right hand side of panel (a), an external magnetic field B is switched on, such that the α_{eff} - and γ -mode shift upwards in the spectrum by the Zeemann energy $g\mu_B B$, depopulating acoustic magnons (red color). Due to the antiparallel alignment, the Gd moment \mathbf{M}_{Gd} is increasingly depolarized by the external field, which leads to a decrease of the gap Δ by an energy δ . As a consequence, the β -mode shifts down in energy and becomes even more strongly populated, which leads to a further suppression of the MMR signal, since the β -mode is assumed to generate a contribution with opposite sign to the MMR signal. All these effects suppress the MMR signal, which results in the large suppression of $\sim 60\%$ (calculated with Eq. 6.1) observed in experiment (c.f. Fig. 6.6). Note that the depolarization of the Gd moment above T_{Comp} is also evident in the magnetic phase diagram in Fig. 6.1. According to our measurements depicted in Fig. 6.5 (d), the MMR signal is almost completely suppressed for an external field of 15 T at $T = 300$ K $> T_{\text{Comp}}$, which might correspond to the phase boundary above T_{Comp} in Fig. 6.1. However, the calculation of the phase diagram predicts much larger values (approximately 30 T) for the critical field at the phase boundary slightly above T_{Comp} . Still, to identify the field suppression of the MMR above T_{Comp} with the depo-

²In Ref. [67] the gap Δ of the β -mode is very small for room temperature, which causes the α - and β -mode to be almost degenerate. However, for the discussion of the field dependence of the MMR we still assume a finite gap Δ at high temperature.

larization of the Gd moment seems reasonable, since we expect an additional suppression due to the transport of magnons across the strip separation d , such that the critical field, where the MMR signal is completely suppressed, might be smaller than 30 T. When the external field exceeds the critical field of the phase boundary, such that the Gd moment is aligned along the external field, the ensuing increase of polarization in the Gd moment may give rise to a recovery of the MMR signal due to the increase of the gap Δ and the accompanying depopulation of the β -mode. To proof this assumption the current data is not sufficient. However, more detailed and systematic MMR experiments extending to higher magnetic fields $\mu_0 H > 15$ T would be an ideal test case for this picture.

The left hand side of panel (b) in Fig. 6.8 depicts the thermally populated magnon spectrum for $T < T_{\text{Comp}}$ with no external magnetic field. The magnon gap Δ is assumed to be slightly larger due to the lower temperature compared to the case depicted in panel (a). With an applied field B (right hand side of panel (b)), the α_{eff} - and γ -mode shift upward by $g\mu_B B$. In contrast to the previous case, the net iron moment $\mathbf{M}_{\text{Fe}}^{\text{net}}$ points antiparallel to the external field, while the Gd moment \mathbf{M}_{Gd} is aligned with field. Consequently, the gap Δ increases by an energy δ due to the increasing order in the Gd moment, resulting in the depopulation of the β -mode³. Qualitatively, this field-behaviour of the magnon spectrum could explain the increasing MMR signal with increasing field observed for $T_{\text{cross}} < T < T_{\text{Comp}}$, since the depopulation of the β -mode with negative chirality gives rise to an increasing MMR signal, which we assumed to be dominated by the acoustic modes with positive chirality. However, in this case it has to be assumed that the field-induced depopulation of the β -mode is more efficient than the depopulation of the α_{eff} and γ -modes. While the depopulation of the γ -mode might be neglected due to its high energy and therefore low occupation, the depopulations of the α_{eff} - and β -mode, parameterized by the Zeeman energy and δ , respectively, have to be investigated quantitatively to proof this approach, which is beyond the scope of this work.

For temperatures $T < T_{\text{cross}}$, the field dependence changes its qualitative behaviour and the signal is again suppressed with increasing field. We attribute this behaviour to the decreasing thermal population of the β -mode, as well as the increasing gap Δ with decreasing temperature. At some point, the depopulation of the α_{eff} -mode is more efficient than the depopulation of the β -mode, which can be measured as the temperature T_{cross} , where the field suppression is zero (c.f. Fig. 6.6). In panel (c) of Fig. 6.8 this is depicted for the case $T \ll T_{\text{Comp}}$, where the β -mode is fully depopulated due to the low thermal energy $k_B T$ and the large gap Δ . As a result, the MMR signal is suppressed due to the depopulation of magnons in the α_{eff} -mode.

It is important to keep in mind that the contributions of the individual magnon modes can have distinctly different weights, which are not only determined by the thermal population. This can be either different excitation efficiencies of magnons with different energies (or \mathbf{k} -vectors) or that different magnon branches exhibit different diffusion lengths, such that the non-local contribution has to be different as well. Note also, that the plateau observed for $T \geq 100$ K in the temperature dependence of the MMR (see Fig. 6.5 (c), (d)) might be an indication for the initiating influence of the optical β -mode due to the increasing thermal population of this mode for intermediate temperatures $T \approx 100$ K (c.f.

³Note that the energy shift δ of the β -mode is likely to depend on the external field, but the exact expression for the field-induced energy shift δ has to be determined accurately by calculating the increase/decrease in order of the Gd moments.

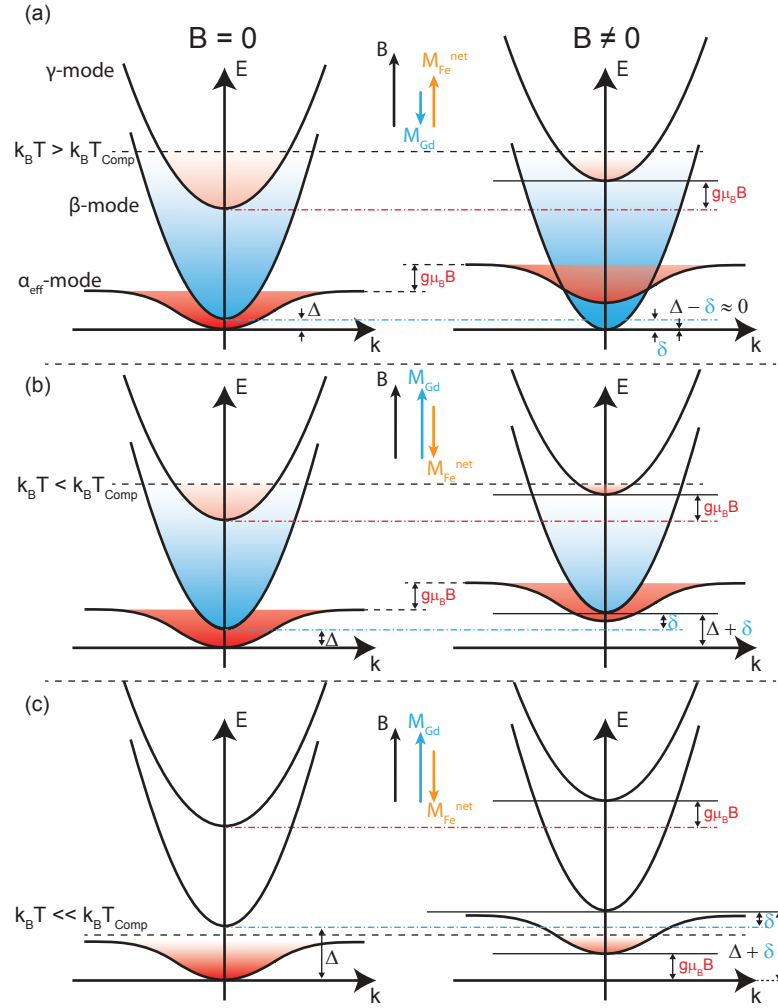


Figure 6.8: Schematics of the GIG magnon spectrum. Three modes (α_{eff} , β and γ) are considered, which are assumed to be considerably occupied near room temperature. (a) For $k_B T > k_B T_{\text{Comp}}$, all three modes are thermally occupied and contribute to the MMR. By switching on the external field, the α_{eff} and γ -mode shift upward by $g\mu_B B$, while the β mode shifts downward by an energy δ due to the increasing depolarization of the Gd moment \mathbf{M}_{Gd} with increasing field strength, since it is antiparallely oriented to the field. As a result, the depopulation of the α_{eff} - and γ -mode with positive chirality and the increasing population of the β -mode with negative chirality give rise to a very strong field suppression. (b) For $k_B T < k_B T_{\text{Comp}}$, still all of the modes are assumed to be (partly) occupied. An external field leads to an upshift by $g\mu_B B$ for the α_{eff} - and γ -mode, while the β -mode now shifts up by δ due to an increasing order in the Gd moments, since the sublattice magnetizations reorient at T_{Comp} . The accompanying depopulation of magnons with negative chirality of the β -mode gives rise to a field-induced enhancement of the MMR signal. (c) For lower temperatures $k_B T \ll k_B T_{\text{Comp}}$ the β -mode is shifted to higher energies due to the increasing order in the Gd moments with decreasing temperature. As a result, the β -mode is only weakly populated, giving rise to the expected field suppression of the signal by the field-induced depopulation of the α_{eff} -mode.

Fig. 6.7). Regarding the MMR field dependence, the influence of the β -mode is visible not until $T_{\text{cross}} \approx 205$ K, which is considerably larger than 100 K. This is nonetheless not surprising, since the efficiency of the field-induced shifts of the different magnon modes is strongly dependent on their exact placement in the dispersion relation due to the energy dependent occupation statistics.

6.2 Thermal Contribution

Due to the Joule heating generated by the applied current in the Pt injector strip, a thermal injection of magnons into the compensated ferrimagnet GIG occurs. As for the MMR, the magnon spectrum of GIG is also a crucial factor for the temperature and field dependence of the thermal effects, as shown in Ref. [67] for the spin Seebeck effect (SSE) (c.f. Sect. 2.3). Therefore, it is of great interest to study the non-local SSE (c.f. Sect. 4.2) in GIG|Pt structures, in order to investigate the transport properties of thermally excited magnons. The experimental data shown in this Section focusses on an injector current of $I = 100 \mu\text{A}$, which ensures enough heating power for a reasonable detection of local and non-local signals. In the following, we investigate the local and non-local SSE signal as a function of temperature in Sect. 6.2.1 and for different magnetic fields up to 7 T in Sect. 6.2.2.

6.2.1 Temperature Dependence

We start with the temperature dependence of the local SSE signals. All data shown in the following were taken at an applied magnetic field $\mu_0 H = 1$ T. The thermal voltage signal $V_{\text{loc}}^{\text{therm}}$ is shown for three different temperatures $T = 300$ K, 100 K and 10 K for a device with $d = 200$ nm and $w = 500$ nm in Fig. 6.9 (a). The signal amplitude $\Delta V_{\text{loc}}^{\text{therm}}$ extracted from the ADMR measurements is plotted as a function of temperature in Fig. 6.9 (b) for two different devices. The SSE voltage signal $\Delta V_{\text{loc}}^{\text{therm}}$ changes sign twice for the measured temperature range, which was already reported in Ref. [67]. The first sign change occurs at the compensation temperature $T_{\text{Comp}} \approx 268$ K of the GIG thin film and a second one at $T_{\text{sign,loc}} \approx 70$ K, which agrees well with the reported $T_{\text{sign,loc}} \approx 70$ K in Ref. [67]. Note also that positive SSE amplitudes feature the same sign of the (local) SSE signal as the SSE signals in YIG|Pt (c.f. Sect. 4.2). The sign change at T_{Comp} is due to the reorientation of the sublattice magnetizations. As a consequence, the spin polarization of the thermally driven interface spin current is inverted, which leads to an inverted SSE signal [67]. The sign change at $T_{\text{sign,loc}}$ is attributed to the thermal population of magnon modes with different chirality, as we discussed for the MMR in Sect. 6.1.2. Below $T_{\text{sign,loc}}$, the α_{eff} -mode with positive chirality dominates the signal, while the contribution from the β -mode with negative chirality steadily increases with temperature [67] (c.f. Sect. 6.1.2), giving rise to a negative signal for $T > T_{\text{sign,loc}}$. We would like to emphasize that this sign inversion is not seen for the MMR in GIG (Sect. 6.1.2). For the MMR, we assumed that magnon modes with positive chirality govern the signal at all temperatures. The observation of a second sign change in the local SSE then implies that different ensembles of magnons must be generated electrically viz. thermally. This might be attributed to the distinctly different excitation process of electrically (MMR) and thermally (SSE) excited magnons, resulting in different properties of the interface spin currents as well. Nonetheless, it might be also reasonable that $T_{\text{sign,loc}}$ corresponds to T_{cross} , where the MMR signal changes its

qualitative field behaviour (see Fig. 6.5 (d)). In this case, the influence of the magnons of the β -mode dominate at different temperatures $T_{\text{sign,loc}} \approx 70$ K and $T_{\text{cross}} \approx 205$ K for the SSE and MMR, respectively. As mentioned in Sect. 6.1.2, the plateau in the temperature dependence of the MMR (c.f. Fig. 6.3 (b)), beginning at $T \approx 100$ K, might also be linked to the initiating influence of the optical β -mode and therefore to the sign change of the local SSE at $T_{\text{sign,loc}}$. A comparison between these two effects (SSE and MMR) is likely to be valid only up to a certain point, since the exact influence of acoustic and optical modes for the sign of the signal generation for the MMR is not fully understood and is subject of ongoing study.

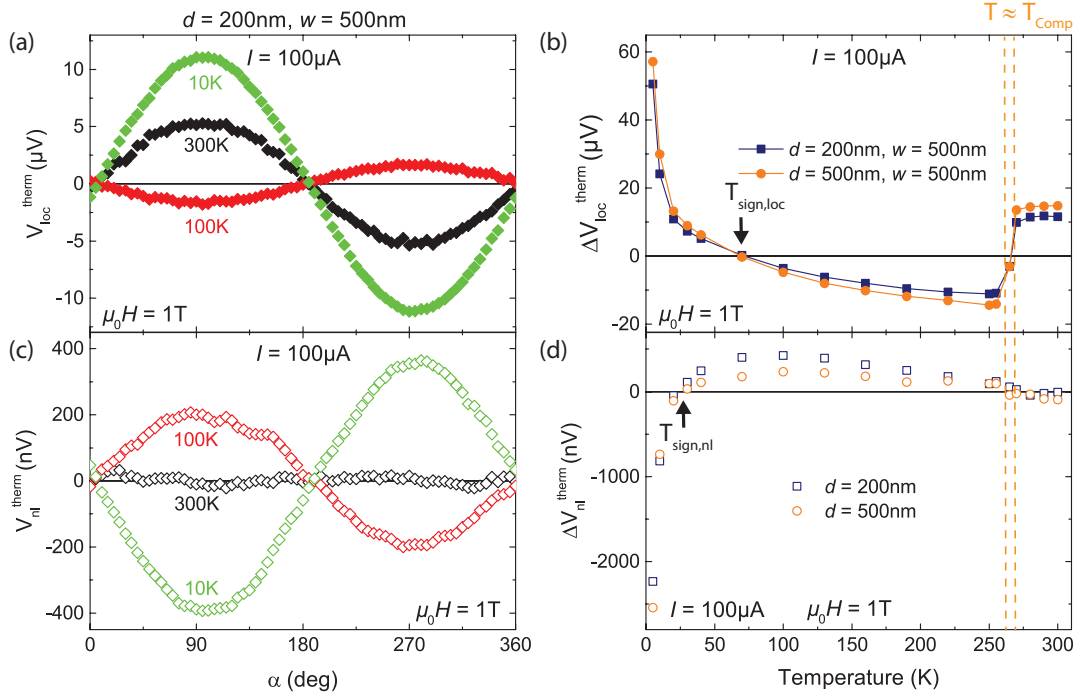


Figure 6.9: (a) Magnetic field orientation dependent modulations of the (local) SSE voltage $V_{\text{loc}}^{\text{therm}}$ for three different temperatures $T = 300$ K, 100 K and 10 K measured for a device with $d = 200$ nm and $w = 500$ nm. (b) (Local) SSE amplitude $\Delta V_{\text{loc}}^{\text{therm}}$ extracted from ADMR measurements for two different devices. The sign of the SSE signal changes sign twice at $T_{\text{Comp}} \approx 268$ K and $T_{\text{sign,loc}} \approx 70$ K. (c) Non-local SSE measurements as a function of magnetic field angle for three different temperatures $T = 300$ K, 100 K and 10 K measured for a device with $d = 200$ nm and $w = 500$ nm. (d) Extracted non-local SSE voltage amplitudes $\Delta V_{\text{nl}}^{\text{therm}}$ versus temperature for $d = 200$ nm and $d = 500$ nm. As for the local case, the non-local SSE signal changes sign at T_{Comp} , whereas a second sign change occurs at $T_{\text{sign,nl}} \neq T_{\text{sign,loc}}$.

Simultaneously, the non-local SSE signal was measured as a function of the magnetic field orientation and different temperatures, as shown in Fig. 6.9 (c) for a device with $d = 200$ nm and $w = 500$ nm exemplarily for $T = 300$ K, 100 K and 10 K. The signal amplitudes are extracted from the field orientation dependent measurements and plotted versus temperature in Fig. 6.9 (d). As for the local case, the signal changes sign at T_{Comp} , but the absolute sign is reversed with respect to the local signal. This is expected for the non-local SSE (at least in the long distance regime $d > d_0$), as we discussed in Sect.

4.2. Therefore, the sign change at T_{Comp} can be explained by the same argument as for the local SSE, where the inversion of the spin quantization axis at T_{Comp} gives rise to the inversion of the spin polarization of the interface spin currents [67]. In the future, more samples with shorter strip separation distances should be investigated to clarify whether the sign change in the non-local SSE signal at T_{Comp} is as abrupt and steep as in the local SSE.

We now turn to the second sign change in the non-local SSE signal at $T_{\text{sign,nl}} \approx 23$ K for $d = 200$ nm and $T_{\text{sign,nl}} \approx 28$ K for $d = 500$ nm. The fact that $T_{\text{sign,nl}} \neq T_{\text{sign,loc}}$ and that the sign change temperature seems to depend on the strip distance leads to the conclusion that this feature does not arise from the same physics as the low temperature sign change of the local SSE signal at $T_{\text{sign,loc}}$. Rather, we attribute this sign change to the same phenomenon occurring in the non-local SSE signals in YIG|Pt discussed in Sect. 4.2.2.1, which is based on the calculations of Ref. [33]. Here, the thermally excited magnon distribution μ_m in YIG is calculated and shows a spherical depletion region (negative μ_m) around the heated Pt strip, whereas the magnons accumulate (positive μ_m) further away from the strip (c.f. Fig. 4.17 in Sect. 4.2.2.1). At this point, it is important to note that a low temperature sign change is expected to occur for the non-local SSE as well, since the interplay between differently polarized modes in the magnon spectrum of GIG responsible for the low temperature sign change in the local SSE should be relevant for the non-local SSE as well. However, for the non-local MMR discussed in Sect. 6.1 we found that the MMR signal does not change its sign at $T_{\text{sign,loc}}$. We therefore assume that the fundamental magnon modes (with positive chirality, $\alpha_{\text{eff-mode}}$) in GIG are key for the understanding of the non-local SSE and MMR signals. As mentioned before, the qualitative change of the MMR field dependence at T_{cross} (see Fig. 6.5 (c),(d)) possibly corresponds to the low temperature sign change at $T_{\text{sign,loc}}$ of the (local) SSE, indicating a pronounced influence of the β -mode also for the MMR (which we assumed to explain the MMR field dependence, c.f. Fig. 6.8). However, to understand how the different modes contribute to the non-local SSE, further investigation in several devices with different strip separations is necessary, in order to confirm that $T_{\text{sign,nl}}$ is indeed distance dependent and not related to the local sign change at $T_{\text{sign,loc}}$.

Besides the sign change at T_{Comp} , we find that the general temperature dependence of the non-local SSE in GIG|Pt is qualitatively similar to the temperature dependence of the non-local SSE in YIG|Pt. In particular, we observe a positive peak of the signal at approximately $T \approx 100$ K. Therefore, similar to the discussion in Sect. 4.2.2.2 for the non-local SSE in YIG|Pt, we attribute this peak to the counteracting factors of an increasing magnon diffusion length λ_m and a decreasing magnon number with decreasing temperature [57]. Thus also the non-local SSE in GIG|Pt is very likely to originate in the diffusion of thermally excited magnons and not attributed to a spurious effect due to a non-local temperature gradient at the detector.

Both the local and non-local SSE in GIG|Pt are highly enhanced for low temperatures. A similar enhancement was observed for the local SSE in the YIG|Pt bilayers in Sect. 4.2. Interestingly, the non-local signal amplitude $\Delta V_{\text{nl}}^{\text{therm}}$ at the lowest measured temperature $T = 5$ K of the device with $d = 500$ nm is larger than the one in the device with $d = 200$ nm. Since this is also the case for the local SSE signals of these two devices, we conclude that this effect is related to interface properties rather than the transport of magnons. As discussed for the YIG|Pt bilayers in Sect. 4.2, this large enhancement might be an artefact

due to the ex situ applied Pt film and the current heating method and should be checked with a different heating method in future experiments [60].

6.2.2 Magnetic Field Dependence

We finally address the magnetic field dependence of the thermal signal in our GIG|Pt structures. The local signal $V_{\text{loc}}^{\text{therm}}$ is shown as a function of magnetic field orientation in Fig. 6.10 (a) for fields up to $\mu_0 H = 7$ T for $T = 250$ K. We find that the local SSE signal is almost independent of field for this temperature. This is true for the majority of the temperature range, as depicted in Fig. 6.10 (b), where the SSE amplitude $\Delta V_{\text{loc}}^{\text{therm}}$ is plotted versus temperature for different magnetic fields. A finite field suppression is observed for low temperatures, which is expected, since the depopulation of thermal magnons by the field-induced spin wave gap is more efficient at low temperatures [45] (c.f. Sect. 4.2.2.3). In contrast to the local SSE in YIG|Pt (c.f. Sect. 4.2), the field dependence vanishes for temperatures $T \gtrsim T_{\text{sign,loc}} = 70$ K, which supports the dominance of the β -mode above $T_{\text{sign,loc}}$ proposed in Ref. [67]. According to this picture, the external field has less impact on the magnon population of the gapped β -mode than on the fundamental α_{eff} , due to the larger population of low energy magnons in the α_{eff} -mode.

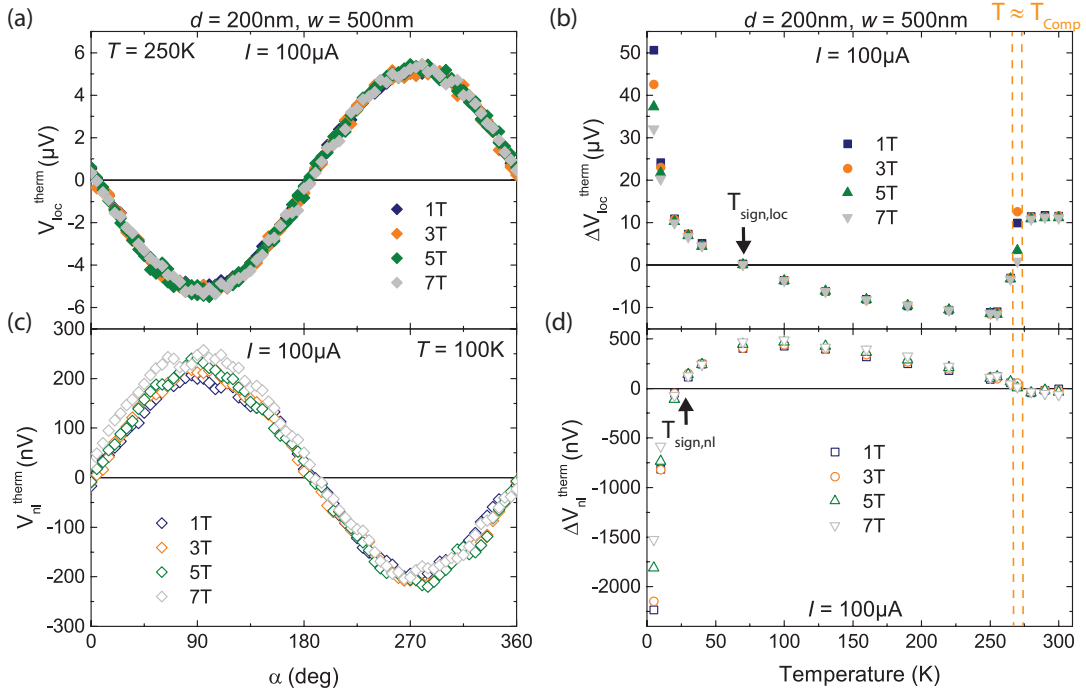


Figure 6.10: Magnetic field dependence of the local and non-local thermal signal in GIG|Pt bilayers for the device with $d = 200$ nm and $w = 500$ nm. (a) Local SSE signal $V_{\text{loc}}^{\text{therm}}$ as a function of magnetic field orientation for different field strengths $\mu_0 H = 1$ T, 3 T, 5 T and 7 T for $T = 250$ K. (b) SSE signal amplitude $\Delta V_{\text{loc}}^{\text{therm}}$ versus temperature for different magnetic fields. (c) Magnetic field orientation dependent measurements of the non-local SSE signal $V_{\text{nl}}^{\text{therm}}$ for different magnetic fields for $T = 100$ K. (d) Non-local SSE amplitude $\Delta V_{\text{nl}}^{\text{therm}}$ versus temperature for different magnetic field strengths.

The evolution of the non-local SSE signal $V_{\text{nl}}^{\text{therm}}$ with temperature and magnetic field

strength is shown in the bottom part of Fig. 6.10. Panel (c) depicts $V_{\text{nl}}^{\text{therm}}$ as a function of magnetic field orientation for $T = 100$ K and the device with $d = 200$ nm and $w = 500$ nm. From these measurements the signal amplitude $\Delta V_{\text{nl}}^{\text{therm}}$ is extracted and plotted versus temperature and different magnetic fields in Fig. 6.10 (d). As for the local case, we find the expected strongly enhanced field suppression for very low temperatures $T \leq 10$ K (c.f. Sect. 4.2). At the temperature of the first sign change $T_{\text{sign,nl}} \approx 23$ K for $d = 200$ nm, the field dependence vanishes due to the vanishing magnon accumulation μ_{m} at this temperature [33]. In the temperature range $T_{\text{sign,nl}} < T < T_{\text{Comp}}$ the signal is even slightly enhanced with increasing field strength. This behaviour is qualitatively consistent with the picture discussed for the field dependence of the MMR in Sect. 6.1.2. The field-induced shift to higher energies of the β -mode with negative chirality below T_{Comp} gives rise to the depopulation of the β -magnons, and eventually an enhancement of the signal, which is assumed to be generated dominantly by the acoustic fundamental mode (see Fig. 6.8) (b)). Due to the very low signal-to-noise ratio around the compensation temperature T_{Comp} , no reasonable statement for the field dependence for this temperature range can be given.

6.3 Summary

In summary, in this Chapter we have presented our exploratory experiments regarding the transport of electrically and thermally injected magnons in the compensated ferrimagnet Gadolinium-Iron-Garnet (GIG). The temperature and field dependence of the local and non-local signal was investigated for both the resistive and thermal contribution.

The thermally occupied magnon spectrum of GIG, together with the magnetic phase diagram is of key importance for the magnon currents in the (local) SSE, non-local SSE and MMR. For the SMR, which is currently only described in a macrospin model [20], the individual magnetic sublattice configuration is highly relevant, while the specific magnon spectrum has a minor effect.

We could almost fully reproduce the SMR temperature dependence reported in Ref. [66] except for a sign change of the SMR at the compensation temperature T_{Comp} . We rather found a vanishing SMR amplitude at T_{Comp} , which we attributed to the rough surface of our GIG film. The rough surface might be responsible for complex sublattice magnetization configurations at the interface due to local shape anisotropies.

The investigation of the non-local resistive signal (i.e. the MMR) yielded a linear scaling of the MMR signal with the applied injector current and a MMR signal decay with increasing strip distance, as expected for the MMR [12]. Moreover, we found a vanishing MMR signal in GIG/Pt for low temperatures $T \approx 10$ K, similar to the behaviour of the MMR in YIG/Pt [13]. As for the SMR, the MMR vanishes at T_{Comp} , which we attributed to the magnetic sublattice structure, i.e. canting in this temperature region.

A key insight in this Chapter was that the different magnon modes of the complex compensated ferrimagnet GIG give rise to interesting field and temperature dependencies. While the magnetic phase diagram (in particular the reorientation of sublattices at T_{Comp}) and the thermal population of magnon modes with different chiralities are responsible for the two sign changes in the spin Seebeck effect in GIG/Pt [67] (at T_{Comp} and at lower temperature $T_{\text{sign,loc}}$), the same physical background accounts for the two qualitative changes in the field behaviour of the MMR (at T_{Comp} and at lower temperature T_{cross} , see

Figs. 6.5 (d) and 6.8). We qualitatively modelled the field dependence of the MMR in GIG|Pt by taking into account the GIG magnon spectrum (calculated in Refs. [67,68]) and worked out the field-induced shifts of each thermally populated magnon mode ($\alpha_{\text{eff-}}$, β - and γ -mode) in GIG above and below T_{Comp} with the help of the magnetic phase diagram of GIG [66]. Due to the reorientation of the sublattice magnetizations at T_{Comp} , the field-induced shift in energy of the β -mode with negative chirality is qualitatively different above and below T_{Comp} , since the magnon gap Δ of the β -mode is dependent on the order of the Gd moments [67]. All observed features of the MMR field dependence could be explained with this model (c.f. Fig. 6.8).

For the non-local spin Seebeck effect, the magnetic phase diagram also describes the sign change at T_{Comp} , but the thermal population of different magnon modes is rather unlikely to explain the low temperature sign change at $T_{\text{sign,nl}}$ of the non-local SSE. Due to the distance dependence of $T_{\text{sign,nl}}$ it is rather described by the positive and negative magnon chemical potential profile [33] around the Pt heater.

Chapter 7

Summary and Outlook

In this work, we investigated the non-local magnon transport in ferrimagnetic insulator/normal metal bilayers. The magnons were generated either electrically, via an electronic spin accumulation, or via a thermal gradient. We studied both Yttrium-Iron-Garnet (YIG)|Platinum (Pt) and Gadolinium-Iron-Garnet (GIG)|Pt [12] bilayers in experiment. The Pt layers were patterned into pairs or sets of long and very narrow wires electrically isolated from one another. In this way, a charge current could be applied to one Pt strip, and non-local voltage signals were measured along the adjacent Pt wires. The main goal hereby was to obtain a systematic understanding of the physical processes behind the electrical and thermal excitation of magnons in the ferrimagnet, as well as their diffusive transport across finite distances. To this end, we systematically studied the non-local magnon transport for different temperatures, magnetic fields and distances. These measurements were performed in magneto-transport type experiments, either rotating a magnetic field of constant magnitude with respect to the sample or via magnetic field sweeps. The key conclusion from these experiments is that several different magnon branches in the ferrimagnet (featuring different helicities/chiralities) must be taken into account for a reasonable description of the data. Moreover, based on our understanding of the electrical injection of magnons in YIG|Pt heterostructures, we were able to build a magnon-based logic device, which performs bitwise operations by pure magnon spin current superposition [61].

A summary of the main results of this work is given in the subsequent Sect. 7.1, while we give proposals for future experiments on this topic in Sect. 7.2.

7.1 Summary

In Chapter 4 we set our focus on the insulating ferrimagnet YIG. Firstly, we studied the purely electrical injection and (non-local) detection of magnons, which characteristically changes as a function of the orientation of the magnetic moments in the ferrimagnet and is called the magnon mediated magnetoresistance (MMR) [13]. The strong temperature dependence of the MMR signal (in particular the vanishing signal for $T < 10$ K) confirms the importance of thermal magnons, i.e. all thermally populated magnon states at a given temperature have to be taken into account for the non-local magnon transport. The dominance of thermal magnons for the MMR was corroborated by the magnetic field dependence, where we introduced a qualitative model based on the thermal population of the fundamental acoustic and high energy optical mode of the YIG magnon spectrum (see Fig. 4.7). Due to the opposite chirality of this optical high energy magnon mode compared to the acoustic fundamental mode [48], the optical and acoustic mode generate a MMR voltage signal of opposite polarity. By rigorously evaluating the distance dependent MMR data, we were able to correlate the impact from the thermal population of the magnon

spectrum in YIG with the MMR behaviour observed in samples with Pt wire separations below $d \approx 1 \mu\text{m}$, while above $1 \mu\text{m}$ the magnon diffusion related effects prevail.

As described in the second part of Chap. 4, we also systematically studied the Joule heating-induced thermal contribution to the non-local voltage signal in YIG|Pt. We compared our Pt strip separation dependent data to a recent theory on the non-local SSE put forward by Cornelissen et al. in Ref. [33]. Hereby, the magnon chemical potential μ_m (induced by the heating of the Pt strip) exhibits a spherical depletion region (negative μ_m) in the YIG around the Pt heater, whereas an accumulation (positive μ_m) is present beyond the depletion region, with μ_m changing its sign at a distance d_0 (see Fig. 4.17). This model is fully consistent with our data. Moreover, we found an increase of d_0 with increasing temperature, which we attributed to the similar temperature dependence of the magnon spin conductivity σ_m [56]. Similar to the qualitative model of the peak in the temperature dependence of the local SSE in Ref. [57], we could give a model for the non-local SSE voltage signal (exhibiting a similar peak in the temperature dependence compared to the SSE) by taking into account the (lateral) magnon diffusion length λ_m . We further could apply our model for the field dependence of the MMR (see Fig. 4.7) to the non-local SSE as well, corroborating the contribution of the thermally occupied optical magnon mode in YIG near room temperature.

Henceforth, in Chap. 5 we utilized the electrical MMR effect for the implementation of a proof of principle 4-strip magnon-based majority gate, with which we were able to perform standard bitwise logic operations such as "AND" and "OR". Our experiments in particular show that magnons generated by different injectors superimpose incoherently. In addition, Pt strips within the magnon diffusion path have no detectable effect on the non-local voltage. We argued that this magnon-based majority gate represents an easy pathway for magnon current based information processing due to the pure DC electrical injection and detection method. Regarding a possible commercial use of such a device, downscaling of the majority gate is technically easy achievable and does not perturb the functionality of the gate, since the logical bits are encoded in the polarization of magnons, and not in their frequency, phase or amplitude. Moreover, the downscaling should even increase the measured voltage signals due to the exponential distance dependence of the MMR. In view of the technologically very important switching frequencies of such devices, we estimated that commercially competitive frequencies up to a few GHz are possible with proper downscaling.

In the final Chapter 6 we investigated the non-local magnon transport in Gadolinium-Iron-Garnet (GIG)|Pt bilayers. To our knowledge this is the first measurement of the non-local diffusive magnon transport in a material different from YIG. The MMR data reproduced the expected linear dependence on the injector current, as well as the decrease of the signal with increasing strip separation [12]. Moreover, the temperature dependence of the resistive MMR signal exhibited the expected vanishing of the signal at very low temperatures $T < 10 \text{K}$, while we also observed a vanishing MMR signal at the compensation temperature T_{Comp} . By taking into account the GIG magnon spectrum [67, 68], the magnetic phase diagram of GIG and the prevalent thermal magnon population of the mode spectrum, a qualitative explanation for the field dependence of the MMR was given (see Fig. 6.8). This model is mainly based on the field-induced increase (decrease) of order in the Gd moments below (above) T_{Comp} , which causes qualitatively different shifts

of the mode spectrum above and below T_{Comp} . Consequently, we could account for the two qualitative changes of the field behaviour (i.e. field enhancement/suppression) of the MMR signal at temperatures T_{cross} and T_{Comp} .

Finally, in the second part of Chap. 6 we addressed the current heating-induced thermal excitation of magnons in GIG. The temperature dependence of the local spin Seebeck effect in GIG|Pt is consistent with the two sign changes at $T_{\text{sign,loc}}$ and T_{Comp} reported in Ref. [67]. In the non-local SSE signal, we also found a sign change at T_{Comp} , and a further one at low temperature $T_{\text{sign,nl}} \neq T_{\text{sign,loc}}$, which is additionally dependent on the strip separation d . Due to the discrepancy that $T_{\text{sign,nl}} \neq T_{\text{sign,loc}}$ and the distance dependence of $T_{\text{sign,nl}}$, we attributed the non-local low temperature sign change at $T_{\text{sign,nl}}$ to the same physics responsible for the sign change of the non-local SSE in YIG|Pt structures, i.e. a sign change in the magnon chemical potential μ_{m} [17, 33].

7.2 Outlook

7.2.1 Influence of Optical Magnons on the MMR Effect

In Sect. 4.1.2 we proposed a model for the field dependence of the MMR in YIG|Pt, based on the thermal population of the spin wave mode spectrum in YIG. Thereby we tacitly assumed that optical magnons, which exhibit an opposite chirality compared to acoustic magnons, generate the opposite sign in the non-local voltage signal of the MMR, compared to acoustic magnons. This assumption is based on the fact that the thermal population or excitation of optical magnons indeed increases the net magnetization, rather than decreasing it (as usually expected for spin waves) [48]. Eventually we assumed that this leads to the diffusion of magnons with magnetic moment $+\hbar$ (acoustic magnons) and $-\hbar$ (optical magnons), generating different signs at the detector. This picture is problematic, however, in the sense that the polarization of the excited non-equilibrium magnons should be fixed by the orientation of the SHE-induced electron spin accumulation μ_{s} at the interface. Still, the experimental evidence and the consistency of our model is striking, such that we maintain the assumption of the different chirality of acoustic and optical magnons for the signal generation in the MMR. This implies that the electronic spin accumulation at the YIG|Pt interface can indeed "generate" magnons with both positive and negative chirality, i.e. carrying " $+\hbar$ " and " $-\hbar$ ". Alternatively, if we assume that all thermally populated magnons (i.e. acoustic and optical ones) contribute to the diffusion, independent of whether the corresponding magnons are directly affected by the SHE-induced spin accumulation or not, a non-equilibrium state (parameterized by the magnon chemical potential μ_{m}) in the magnon spectrum is sufficient to motivate the different signs for acoustic and optical magnons. This assumption should be true for a strong magnon-magnon interaction, such that the diffusion of magnons (which arises via a finite magnon chemical potential μ_{m} [31]) does not have to be solely related to directly excited non-equilibrium magnons (i.e. acoustic or optical ones). In fact a strong interaction within the thermal magnon population and an externally induced out of equilibrium state in the magnon distribution would lead to a redistribution of all thermally excited acoustic and optical magnons, such that all populated magnons should participate in the diffusion process. From an experimental point of view, it is therefore important to measure an explicit footprint of the optical mode, i.e. measure the sign change of the MMR when the optical magnons dominate. In Sect. 4.1.2, this behaviour was emerging in field sweep data

of the MMR, where the non-local voltage sign indeed seems to change for high temperature and high magnetic fields, for which the population of the optical mode becomes more and more substantial. In addition to this, the sign change might be only visible for certain strip separations, since the different magnons (acoustic and optical ones) are likely to have different diffusion lengths, such that the modes no longer contribute equally for longer distances. For future experiments, it would therefore be very important to measure the MMR at temperatures well above room temperature, as well as in high magnetic fields, in an attempt to further increase the population of the optical mode. To do this properly, a full rotation of the external magnetic field should be conducted, in order to be able to compare the maxima and minima of the MMR signal and thereby exclude possible effects from offset voltages. In this way, the MMR constitutes a comparatively simple method to map out the thermal spectrum of magnons in the THz-regime, which usually requires sophisticated methods such as neutron scattering or THz spectroscopy.

7.2.2 Influence of Magnetic Damping/Structure on Magnon Diffusion

The diffusion of spin waves is a complex subject, since magnons do not conserve particle number, which is a requirement for the usual diffusion equation of classical particles. However, it is proposed that the diffusion of magnons is parameterized by the magnon temperature T_m and the magnon chemical potential μ_m , where the timescale of the diffusion of magnons is assumed to be limited by the magnon non-conserving relaxation time into the phonon bath [31], which is related to the relaxation of the magnon chemical potential μ_m into its equilibrium value $\mu_m = 0$. This relaxation of magnons can be roughly parameterized by the Gilbert damping parameter α_G [31]. Thus, to prove the assumed strong influence of α_G for the diffusion of magnons, MMR experiments in magnet|metal heterostructures made from insulating magnets with different damping parameters should be considered for the MMR effect, such as magnetite (Fe_3O_4) [69]. Instead of investigating a completely different magnetic insulator, one could also manipulate the damping of the well-known Yttrium-Iron-Garnet (YIG) by doping. The doping of non-magnetic atoms can be utilized to affect the saturation magnetization of the YIG and therefore its magnetic damping [70].

In addition to this, the electrical or thermal injection of magnons in a non-local antiferromagnet (AFM)|Pt bilayer will allow for a deeper understanding of the non-local magnon diffusion process. For both the electrical and thermal excitation of magnons (MMR and non-local SSE, respectively), it would be interesting to see if one can measure a finite non-local signal at all. Regarding the electrical effect (MMR), the excitation of the non-equilibrium magnon accumulation is subject to the interchange of spin angular momentum, which might be suppressed in an AFM with vanishing net magnetization. If no signal can be measured, the interchange of spin momentum at the interface can be assumed to require a finite net magnetization. If, however, a finite non-local signal can be measured in the AFM|Pt structure, this would suggest that a thermal population of antiferromagnetic magnons with finite magnetic moment is sufficient for forming a non-equilibrium population. Due to the strong evidence we found in this work for the dominance of thermal magnons for the MMR, we expect a finite non-local signal in an antiferromagnet. In this context, the investigation of the non-local transport in a compensated ferrimagnet such as Gadolinium-Iron-Garnet (GIG) (as presented in Chap. 6), where the (local) SMR changes sign at T_{Comp} , would be very instructive. If the MMR exhibits a 90° phase shift at T_{Comp}

(within the spin canting phase, similar to the SMR in GIG [66]), one would conclude that the MMR depends on the orientation of individual sublattice moments (the local moments at the interface). In this picture, we would expect a finite non-local MMR signal in an antiferromagnet as well, since the thermally populated antiferromagnetic magnon modes should contribute to the non-local signal. However, as predicted in Ref. [71] for the spin Seebeck effect (SSE), a vanishing SSE signal in an AFM for very low magnetic fields is expected, since the antiferromagnetic magnon branches are degenerate and therefore inject the same amount of oppositely polarized magnons. For larger magnetic fields, however, the different magnon branches of an antiferromagnet lose their degeneracy, such that a finite SSE signal is expected in Ref. [71]. These predictions (i.e. vanishing SSE signal for low magnetic fields, finite SSE signal for large magnetic fields in an AFM) should be also valid for the MMR in an AFM, since we found that acoustic and optical modes contribute differently to the effect (see Sect. 4.1.2), similar to the SSE in GIG (as reported in Ref. [67]). Note, however, that the investigation of the non-local magnon transport in an AFM is not straightforward, since due to the vanishing net magnetization an external magnetic field cannot rotate the antiparallel sublattice magnetizations. Therefore, an antiferromagnet with a Néel temperature $T_N < 300$ K should be considered, such that field-cooling from $T > T_N$ to $T < T_N$ in an external field allows to set the orientation of the magnetic sublattices. It should be also kept in mind that a vanishing non-local signal in an AFM|Pt structure does not have to be necessarily attributed to the magnetic structure, but can be also due to the damping in the AFM, which might be distinctly different to a ferrimagnet with a finite net magnetization. Moreover, a comparison of the electrical to the thermal excitation of magnons in an AFM|Pt bilayer would be interesting, since this might give further information about the microscopic origin of both effects.

7.2.3 Phonon Heat Transport in the Non-local Spin Seebeck Effect

During this thesis, we emphasized that a "spurious" contribution to the non-local spin Seebeck effect via a non-local temperature gradient at the detector strip cannot be ruled out completely. Therefore, this should be checked in experiment for a non-local FMI|Pt structure, where the diffusion path of magnons in the FMI is interrupted by a gap in the FMI. Then the diffusion of magnons is completely suppressed, while phononic heat transfer across the non-magnetic substrate is still possible. The magnitude of the non-local signal should then indicate whether the contribution is really neglectable.

7.2.4 Non-local Spin Transport in YIG|FM Nanostructures

At the end of this thesis, we additionally investigated the non-local spin transport in bilayers consisting of YIG and a ferromagnetic metal (FM), instead of the non-magnetic platinum. To this end, we structured non-local devices (see Chap. 3) of either 10 nm thick e-beam evaporated Cobalt (Co) or Nickel (Ni) on a 1 μ m thick YIG film. In order to prevent oxidation processes of the ferromagnetic metals, a thin ~ 2.5 nm aluminum (Al) capping layer was sputtered on top of the Co layer, while this could not be done for the YIG|Ni sample due to technical issues. Moreover, we fabricated two reference samples with non-local devices of Co(10 nm)|Al(2.5 nm) and Ni(10 nm)|Al(2.5 nm) on an insulating Yttrium-Aluminum-Garnet (YAG) substrate, in order to exclude possible spurious contributions to the non-local signals, which are not related to the YIG. In Fig. 7.1, all field orientation

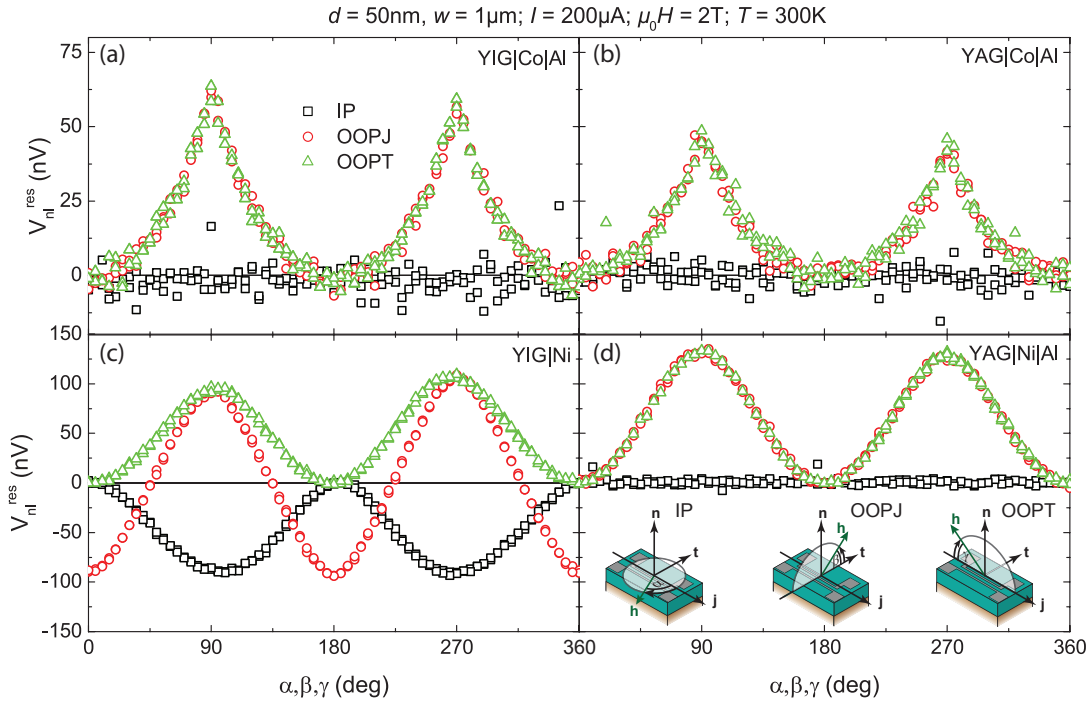


Figure 7.1: Non-local resistive ADMR measurements of V_{nl}^{res} for various bilayer samples consisting of (a) YIG|Co|Al, (b) YAG|Co|Al, (c) YIG|Ni and (d) YAG|Ni|Al. The data is shown for all three orthogonal rotation planes (IP, OOPJ, OOPT) with external parameters $I = 100 \mu\text{A}$ (injector current), $\mu_0 H = 2 \text{ T}$ (magnetic field strength) and temperature $T = 300 \text{ K}$. Non-local signals are measured for similar devices with $d = 50 \text{ nm}$ and $w = 1 \mu\text{m}$ for all samples.

dependent MMR data for these samples is shown for similar devices with $d = 50 \text{ nm}$ and $w = 1 \mu\text{m}$, as well as an injector current $I = 200 \mu\text{A}$, a magnetic field strength $\mu_0 H = 2 \text{ T}$ and at a temperature $T = 300 \text{ K}$. Panel (a) of Fig. 7.1 exemplarily depicts the resistive contribution of the non-local signal measured on a YIG|Co|Aluminum (Al) sample as a function of magnetic field orientation for all three orthogonal rotation planes (IP, OOPJ, OOPT). For a MMR-like effect (c.f. Sect. 2.4), we would expect a finite 180° periodic negative voltage signal with extrema in V_{nl}^{res} for 90° and 270° in the IP and OOPJ rotation planes for the present measurement configuration. Instead, we find a positive 180° periodic signal for both the OOPJ and OOPT configurations, while the signal is constantly zero for the IP rotation. These finite signals only arise for out of plane field directions. At first glance, this suggests an effect which generates an out of plane spin polarization in the FM and hence an excitation and detection of magnons in YIG with solely out of plane polarization. However, the reference sample with non-local Co|Al structures on the insulator YAG interestingly exhibits the exact same behaviour as the YIG|Co|Al sample, as shown in Fig. 7.1 (b) for a similar device with $d = 50 \text{ nm}$ and $w = 1 \mu\text{m}$. Consequently, the observed effect in YIG|Co cannot be exclusively related to a non-local signal generation via magnon transport. The spikes in Fig. 7.1 (a) and (b) are attributed to the large out of plane shape anisotropy of the thin Cobalt layer ($\approx 10 \text{ nm}$), which can be overcome for higher magnetic fields $\mu_0 H \geq 3 \text{ T}$ (not shown here).

The non-local response of a device on a YIG|Ni bilayer is depicted in Fig. 7.1 (c). In contrast to the YIG|Co sample, we now observe a typical MMR-like signal in the IP configuration, exhibiting the expected negative voltage signals $V_{\text{nl}}^{\text{res}}$ when the external field is collinear to the \mathbf{t} -axis, while zero voltage is detected when the external field points along the \mathbf{j} -axis. As expected from the MMR, this negative signal is also observed for the OOPJ rotation, but is superimposed by the yet unknown positive non-local signal observed for out of plane directions. In the OOPT configuration, the (negative) MMR fingerprint vanishes, but the positive out of plane signal remains. The reference sample YAG|Ni|Al, which is shown in Fig. 7.1 (d), indeed does not exhibit the YIG-related negative MMR voltage signals. Still, the positive out of plane signal is also present for the YAG|Ni|Al sample. These findings suggest that Co either has a low spin Hall angle Θ_{SH} or a low spin diffusion length, such that no magnons can be excited/detected in the YIG, giving rise to a vanishing MMR signal for the YIG|Co|Al sample.

The positive voltage signals for the out of plane directions of non-local devices consisting of non-magnetic insulator and ferromagnetic metals are very puzzling, since there is, up to now, no easy explanation for the effect. One could think of a phonon-mediated signal. However, phonons typically do not carry spin angular momentum, making this rather unlikely. Furthermore, an inductive contribution due to the current reversal method we use for the separation of resistive and thermal contributions (see Sect. 3.3) could be an issue. Thereby, it might be possible that during the current reversal a time-dependent Oersted field emerges, which may induce a voltage at the non-local FM strip. However, this effect should not depend on the magnetization orientation, such that also this explanation fails. An electrical crosstalk between the strips might give rise to an anisotropic magnetoresistance in the non-local signal. However, in this case no signal in the OOPJ rotation plane would be expected, in contrast to the results shown in Fig. 7.1. Additionally, the fact that the signal goes to zero for field directions in the plane of the thin film does not corroborate a crosstalk between the strips, since this should not depend on the external field direction. Future experiments on this kind of material systems should be carried out for different strip separations, in order to extract the distance dependence of the effect to possibly imply which effect is responsible for the signal. In addition to this, the MMR-like effect observed for the YIG|Ni sample in Fig. 7.1 (c) is also interesting for further experiments, since there are unexpected field behaviours that seem to be strongly related to the Ni magnetization (not shown here).

Appendix A

Theoretical Model for the Temperature and Field Dependence of the Magnon Diffusion Length

The magnon diffusion length λ_m , which we extracted from the distance dependent MMR data in Sect. 4.1.3, is assumed to be a superposition of all \mathbf{k} -dependent mean free paths $\lambda_{\mathbf{k}} = v_{\mathbf{k}}\tau_{\mathbf{k}}$ of all thermally populated magnon states with magnon group velocity $v_{\mathbf{k}} = \frac{1}{\hbar} \frac{\partial \epsilon}{\partial \mathbf{k}}$ and magnon relaxation time $\tau_{\mathbf{k}}$. We therefore can write down a simple equation for λ_m by calculating the statistical average over all microscopic mean free paths $\lambda_{\mathbf{k}}$ as

$$\lambda_m = \frac{1}{N_{\text{mag}}} \int_{\epsilon_z}^{\epsilon_{\text{max}}} d\epsilon \lambda_{\mathbf{k}} \mathcal{D}(\epsilon, B) f_{\text{BE}}(\epsilon, T) \quad (\text{A.1})$$

where $N_{\text{mag}} = \int_{\epsilon_z}^{\epsilon_{\text{max}}} d\epsilon \mathcal{D}(\epsilon, B) f_{\text{BE}}(\epsilon, T)$ is the total number of excited magnons at temperature T , $\mathcal{D}(\epsilon) = \frac{1}{4\pi^2 J_s^{3/2}} \sqrt{\epsilon - \epsilon_z}$ is the density of states per energy and volume and $f_{\text{BE}}(\epsilon, T) = \left(\exp\left(\frac{\epsilon}{k_B T}\right) - 1 \right)^{-1}$ the Bose-Einstein distribution function. We assume an isotropic, quadratic magnon dispersion $\epsilon = J_s \mathbf{k}^2 + \epsilon_z$ with spin wave stiffness $J_s = 8.458 \cdot 10^{-40} \text{J m}^2$ [31] and the spin wave gap (Zeeman energy) $\epsilon_z = g\mu_B B$. The integration takes place from ϵ_z up to the maximum magnon energy $\epsilon_{\text{max}} \approx \frac{3k_B T_C}{S+1}$ with $T_C = 560 \text{K}$ the Curie temperature and $S = 10$ the spin quantum number per unit cell of YIG [23,31]. While it is straightforward to write down the magnon group velocity via the magnon dispersion as $v_{\mathbf{k}} = \frac{2J_s \mathbf{k}}{\hbar} = \frac{2J_s \sqrt{\epsilon - \epsilon_z}}{\hbar}$, it is quite difficult to obtain a simple expression for the \mathbf{k} -dependent magnon scattering rates $\tau_{\mathbf{k}}$, since this is strongly dependent on the microscopic scattering processes with phonons, magnons or defects [31,50,54]. However, we can give a rough model for the scattering times, considering two assumptions: at first, we assume that the relaxation of magnons for $\mathbf{k} = 0$ is limited by non-conserving magnon-phonon interactions, parameterized by $\tau_{\alpha} \approx \frac{\hbar}{\alpha_G k_B T}$ with α_G the Gilbert damping parameter (see Ref. [31]). Secondly, we assume that the relaxation time $\tau_{\mathbf{k}}$ decreases with increasing wavevector \mathbf{k} as $\tau_{\mathbf{k}} \propto \frac{1}{k^n}$ [31,50,54]. These two assumptions then give rise to the expression

$$\tau_{\mathbf{k}} = \frac{\tau_{\alpha}}{(|\mathbf{k}|a)^n + 1} = \frac{\tau_{\alpha}}{\left(\sqrt{\frac{\epsilon - \epsilon_z}{J_s}} a \right)^n + 1} \quad (\text{A.2})$$

with $a = 12.376 \text{\AA}$ the lattice constant of YIG [36]. As can be seen from Eq. A.2, $\tau_{\mathbf{k}} \rightarrow \tau_{\alpha}$ for $\mathbf{k} = 0$, while $\tau_{\mathbf{k}} \rightarrow 0$ for $\mathbf{k} \rightarrow \infty$. Finally, we can calculate Eq. A.1 as

Appendix A Theoretical Model for the Temperature and Field Dependence of the Magnon Diffusion Length

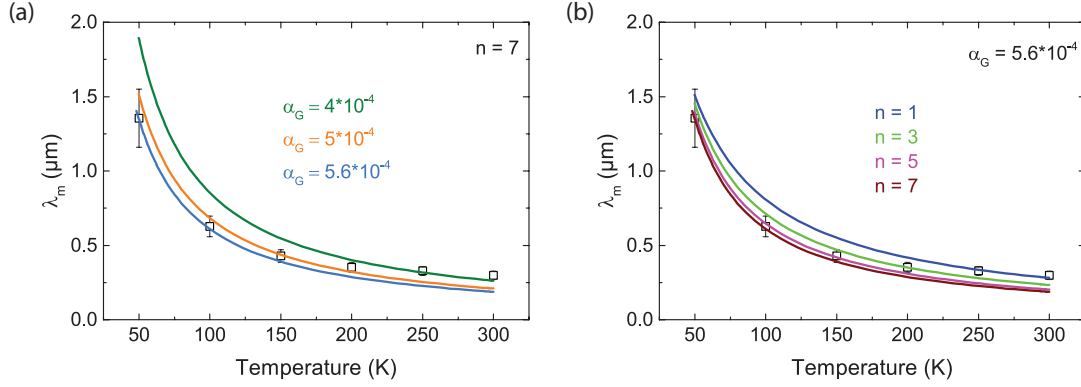


Figure A.1: Magnon diffusion length λ_m calculated with Eq. A.3 for (a) different Gilbert damping parameters α_G and (b) different exponents n (solid lines). The open squares represent the measured λ_m of Sect. 4.1.3.

$$\begin{aligned}
 \lambda_m &= \frac{1}{N_{\text{mag}}} \int_{\epsilon_z}^{\epsilon_{\text{max}}} d\epsilon \underbrace{\frac{2J_s \sqrt{\epsilon - \epsilon_z}}{\hbar}}_{v_{\mathbf{k}}} \underbrace{\frac{\tau_\alpha}{\left(\sqrt{\frac{\epsilon - \epsilon_z}{J_s}} a\right)^n + 1}}_{\tau_{\mathbf{k}}} \\
 &\times \underbrace{\frac{1}{4\pi^2 J_s^{3/2}} \sqrt{\epsilon - \epsilon_z}}_{\mathcal{D}(\epsilon, B)} \underbrace{\left(\exp\left(\frac{\epsilon}{k_B T}\right) - 1\right)^{-1}}_{f_{\text{BE}}(\epsilon, T)} = \\
 &\frac{1}{N_{\text{mag}}} \frac{k_B T}{2\pi^2 J_s \alpha_G} \int_{x_z}^{x_{\text{max}}} dx \frac{x - x_z}{\exp(x) - 1} \frac{1}{\left(\sqrt{\frac{k_B T(x - x_z)}{J_s}} a\right)^n + 1} \quad (\text{A.3})
 \end{aligned}$$

where we substituted $x = \frac{\epsilon}{k_B T}$ and defined $x_z = \frac{\epsilon_z}{k_B T}$, $x_{\text{max}} = \frac{\epsilon_{\text{max}}}{k_B T}$. The integral in Eq. A.3 can be evaluated numerically via the "NIntegrate[]"-function in Mathematica. The external field is set to $B = 1$ T. Together with the measured λ_m of Sect. 4.1.3 (open symbols in Fig. A.1), the result of the calculation of Eq. A.3 is shown as a function of temperature in Fig. A.1 (a) for different Gilbert damping parameters α_G with $n = 7$ and in panel (b) for different exponents n with $\alpha_G = 5.6 \cdot 10^{-4}$.

In order to get reasonable agreement with measurements, the Gilbert damping α_G has to be chosen in the order of several $\sim 10^{-4}$. The exponent n only slightly affects the temperature dependence, but has a large impact on the field dependence, as we will see later. We further see, that the qualitative temperature dependence of the measured λ_m is not fully reproduced by Eq. A.3, which indicates that an additional temperature dependence might be included to get proper agreement. Still, with respect to the rough assumptions for the calculation, the agreement is reasonable.

Furthermore, we can also evaluate Eq. A.3 as a function of the external magnetic field B . In the following, the Gilbert damping is always set to $\alpha_G = 5.6 \cdot 10^{-4}$. The magnetic

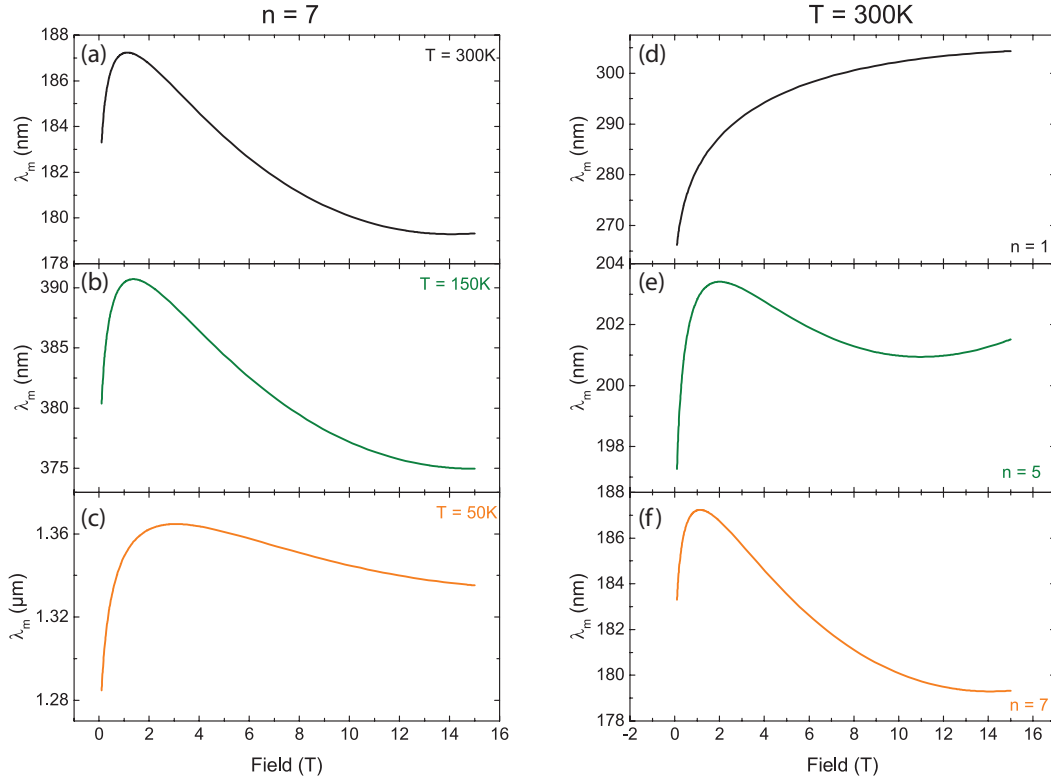


Figure A.2: Magnetic field dependence of the magnon diffusion length λ_m for $n = 7$ and different temperatures: (a) $T = 300$ K, (b) $T = 150$ K and (c) $T = 50$ K (c). For a fixed temperature $T = 300$ K the magnetic field dependence of λ_m is shown for different exponents $n = 1$ (a), $n = 5$ (b) and $n = 7$ (c).

field dependence calculated with Eq. A.3 is shown in the left column of Fig. A.2 for $n = 7$ and different temperatures $T = 300$ K (a), 150 K (b) and 50 K (c). While for low magnetic fields $B \leq 1$ T the magnon diffusion length increases with field, it decreases for higher magnetic fields up to 15 T. The overall field dependence is strongly dependent on the choice of the exponent n , which is depicted in Figs. A.2 (d)-(f) for different n and fixed temperature $T = 300$ K. In order to account for a decreasing λ_m beyond ~ 1 T we choose $n = 7$, since the decrease is expected and was measured in Sect. 4.1.3.

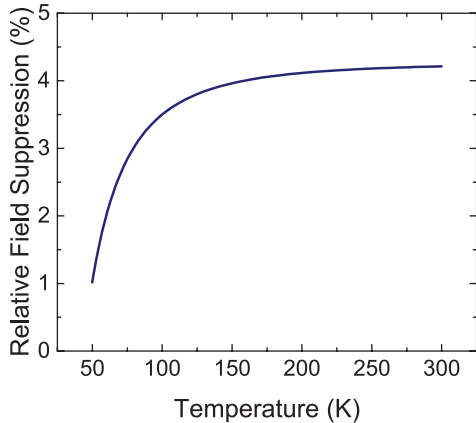


Figure A.3: Relative field suppression of λ_m versus temperature, calculated using Eq. A.4.

λ_m is larger by roughly $\sim 25\%$. This discrepancy might be due to a further field dependence of τ_α , which we disregarded in our model. In the course of this, we therefore tried to include a field dependence in the relaxation time as $\tau_\alpha \propto \frac{1}{B}$. With this, the relative field suppression obviously becomes larger, but also changes its qualitative behaviour with temperature, since an increase with decreasing temperature is then evident (not shown here). Intuitively, such a behaviour would be expected, since the suppression of magnons with small wavevectors and therefore large relaxation times is expected to be more efficient at low temperature. Hence, for future experiments the field dependence of the MMR should be remeasured properly at low temperatures, since the present data at low temperatures exhibits a large signal to noise ratio. In order to enhance the resolution, one could simply increase the injector current, such that reasonable signals can be measured at low temperature, where the MMR signal is low due to its $\sim T^{\frac{3}{2}}$ -dependence at low temperature (c.f. Sect. 4.1.1).

As a next step we can calculate the relative field suppression of λ_m as

$$\frac{\lambda_m(B = 1 \text{ T}) - \lambda_m(B = 15 \text{ T})}{\lambda_m(B = 1 \text{ T})}, \quad (\text{A.4})$$

where we evaluate $\lambda_m(B)$ with Eq. A.3. The result of Eq. A.4 as a function of temperature is shown in Fig. A.3. Qualitatively, the increasing suppression with increasing field reproduces the observed behaviour of the relative field suppression of the diffusive part in Sect. 4.1.3 (c.f. 4.11 and Fig. 4.13 (c)). However, the quantitative agreement is poor, since the measured suppression of

Appendix B

Crosstalk between Electrically Isolated Pt Strips on YIG

The possibility of an electrical crosstalk between the Pt strips on YIG is discussed in the following. During this work, we observed a finite non-local offset voltage in the order of a few 10 nV in some devices. However, this offset voltage was not reproducible and appeared irregularly in different measurement setups. In order to quantitatively examine a possible origin of the offset, an equivalent circuit diagram of the two strip structure including the high resistance of the insulating layer is shown in Fig. B.1.

We estimate the resistance of the insulating film to approximately $R_I \approx 1 \text{ G}\Omega$, while the metal strips exhibit a resistance of roughly $R_M \approx 10 \text{ k}\Omega$. A sourcemeter is attached to the left metal strip and applies a current $I = 100 \mu\text{A}$. Following Kirchhoff's first law, the current I splits in the first node as $I = I_1 + I_2$. According to Kirchhoff's second law, the applied voltage follows $V = V_1 = V_2 + V_3 + V_4$. Therefore, the current $I_2 = \frac{V}{2R_I + R_M}$ with $V = R_{\text{tot}} \cdot I$, where $R_{\text{tot}} = \frac{R_M(2R_I + R_M)}{2R_I + 2R_M}$ is the total resistance of the whole network. Using the above mentioned values, the expected voltage of the non-local metal strip is $V_3 = I_2 \cdot R_M \approx 5 \mu\text{V}$. This value

is three orders of magnitude higher than the measured offset voltages of a few 10 nV, concluding that the offset voltage cannot be explained by a crosstalk through the YIG itself or that the equivalent circuit diagram does not describe the current behaviour well. Both is likely to be true, wherefore we infer that these irregular offset voltages arise from slightly conductive surface contaminations or moisture, which give rise to complex current paths and therefore voltage offsets.

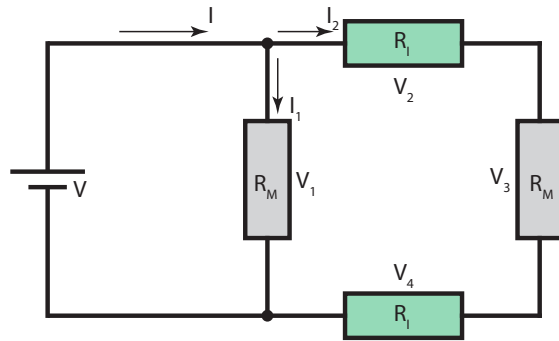


Figure B.1: Equivalent circuit diagram of a typical two strip structure. A current I is applied to the left metal strip with resistance R_M . In this network, the insulating layer beneath the metal strips is treated as a large resistance R_I .

Bibliography

- [1] R. M. Brown. *Sudden Death* (Bantam Doubleday Dell Publishing Group Inc, United States (1998), 1984).
- [2] L. S.-C. World Service Conference. Narcotics Anonymus (1981). Basic Text.
- [3] Wikipedia, The Free Encyclopedia. https://en.wikipedia.org/wiki/Magnetic_storage.
- [4] J. E. Hirsch. Spin Hall Effect. *Physical Review Letters* **83**, 1834–1837 (1999). URL.
- [5] E. Saitoh, M. Ueda, H. Miyajima & G. Tatara. Conversion of spin current into charge current at room temperature: Inverse spin-Hall effect. *Applied Physics Letters* **88**, 182509–182509–3 (2006). URL.
- [6] S. Murakami, N. Nagaosa & S.-C. Zhang. Dissipationless Quantum Spin Current at Room Temperature. *Science* **301**, 1348–1351 (2003). URL.
- [7] O. Mosendz, V. Vlaminck, J. E. Pearson, F. Y. Fradin, G. E. W. Bauer, S. D. Bader & A. Hoffmann. Detection and quantification of inverse spin Hall effect from spin pumping in permalloy/normal metal bilayers. *Physical Review B* **82**, 214403 (2010). URL.
- [8] F. D. Czeschka, L. Dreher, M. S. Brandt, M. Weiler, M. Althammer, I.-M. Imort, G. Reiss, A. Thomas, W. Schoch, W. Limmer, H. Huebl, R. Gross & S. T. B. Goennenwein. Scaling Behavior of the Spin Pumping Effect in Ferromagnet-Platinum Bilayers. *Physical Review Letters* **107**, 046601 (2011). URL.
- [9] C. H. Du, H. L. Wang, Y. Pu, T. L. Meyer, P. M. Woodward, F. Y. Yang & P. C. Hammel. Probing the Spin Pumping Mechanism: Exchange Coupling with Exponential Decay in $\text{Y}_3\text{Fe}_5\text{O}_{12}$ /Barrier/Pt Heterostructures. *Physical Review Letters* **111**, 247202 (2013). URL.
- [10] C. Hahn, G. de Loubens, M. Viret, O. Klein, V. V. Naletov & J. Ben Youssef. Detection of Microwave Spin Pumping Using the Inverse Spin Hall Effect. *Physical Review Letters* **111**, 217204 (2013). URL.
- [11] Y. K. Kato, R. C. Myers, A. C. Gossard & D. D. Awschalom. Observation of the Spin Hall Effect in Semiconductors. *Science* **306**, 1910–1913 (2004). URL.
- [12] L. J. Cornelissen, J. Liu, R. A. Duine, J. B. Youssef & B. J. van Wees. Long-distance transport of magnon spin information in a magnetic insulator at room temperature. *Nature Physics* **advanced online publication** (2015). URL.

- [13] S. T. B. Goennenwein, R. Schlitz, M. Pernpeintner, K. Ganzhorn, M. Althammer, R. Gross & H. Huebl. Non-local magnetoresistance in YIG/Pt nanostructures. *Applied Physics Letters* **107**, 172405 (2015). URL.
- [14] J. Xiao, G. E. W. Bauer, K.-c. Uchida, E. Saitoh & S. Maekawa. Theory of magnon-driven spin Seebeck effect. *Physical Review B* **81**, 214418 (2010). URL.
- [15] M. Schreier, A. Kamra, M. Weiler, J. Xiao, G. E. W. Bauer, R. Gross & S. T. B. Goennenwein. Magnon, phonon, and electron temperature profiles and the spin Seebeck effect in magnetic insulator/normal metal hybrid structures. *Physical Review B* **88**, 094410 (2013). URL.
- [16] M. Schreier, N. Roschewsky, E. Dobler, S. Meyer, H. Huebl, R. Gross & S. T. B. Goennenwein. Current heating induced spin Seebeck effect. *Applied Physics Letters* **103**, 242404 (2013). URL.
- [17] K. Ganzhorn, T. Wimmer, J. Cramer, S. Geprägs, R. Gross, H. Huebl, M. Kläui & S. T. B. Goennenwein. Temperature dependence of the non-local spin Seebeck effect in YIG/Pt nanostructures. *In preparation* (2016).
- [18] H. Nakayama, M. Althammer, Y.-T. Chen, K. Uchida, Y. Kajiwara, D. Kikuchi, T. Ohtani, S. Geprägs, M. Opel, S. Takahashi, R. Gross, G. E. W. Bauer, S. T. B. Goennenwein & E. Saitoh. Spin Hall Magnetoresistance Induced by a Nonequilibrium Proximity Effect. *Physical Review Letters* **110**, 206601 (2013). URL.
- [19] M. Althammer, S. Meyer, H. Nakayama, M. Schreier, S. Altmannshofer, M. Weiler, H. Huebl, S. Geprägs, M. Opel, R. Gross, D. Meier, C. Klewe, T. Kuschel, J.-M. Schmalhorst, G. Reiss, L. Shen, A. Gupta, Y.-T. Chen, G. E. W. Bauer, E. Saitoh & S. T. B. Goennenwein. Quantitative study of the spin Hall magnetoresistance in ferromagnetic insulator/normal metal hybrids. *Physical Review B* **87**, 224401 (2013). URL.
- [20] Y.-T. Chen, S. Takahashi, H. Nakayama, M. Althammer, S. T. B. Goennenwein, E. Saitoh & G. E. W. Bauer. Theory of spin Hall magnetoresistance. *Physical Review B* **87**, 144411 (2013). URL.
- [21] K. Uchida, J. Xiao, H. Adachi, J. Ohe, S. Takahashi, J. Ieda, T. Ota, Y. Kajiwara, H. Umezawa, H. Kawai, G. E. W. Bauer, S. Maekawa & E. Saitoh. Spin Seebeck insulator. *Nature Materials* **9**, 894–897 (2010). URL.
- [22] S. S.-L. Zhang & S. Zhang. Magnon Mediated Electric Current Drag Across a Ferromagnetic Insulator Layer. *Physical Review Letters* **109**, 096603 (2012). URL.
- [23] S. S.-L. Zhang & S. Zhang. Spin convertance at magnetic interfaces. *Physical Review B* **86**, 214424 (2012). URL.
- [24] F. D. Czeschka. *Spin Currents in Metallic Nanostructures*. Ph.D. thesis, Technische Universität München (2011).
- [25] M. V. Berry. Quantal Phase Factors Accompanying Adiabatic Changes. *Proceedings of the Royal Society of London. A. Mathematical and Physical Sciences* **392**, 45–57 (1984). URL.

-
- [26] J. Smit. The Spontaneous Hall Effect in Ferromagnetics II. *ArXiv e-prints* **24**, 39 – 51 (1958). URL.
- [27] L. Berger. Side-Jump Mechanism for the Hall Effect of Ferromagnets. *Physical Review B* **2**, 4559–4566 (1970). URL.
- [28] H. Haken & H. C. Wolf. *Atom- und Quantenphysik. Einführung in die experimentellen und theoretischen Grundlagen.* (Springer, 2003), 8 edn.
- [29] F. P. Witek. *Spin Hall Magnetoresistance Noise.* Master’s thesis, Technische Universität München (2013).
- [30] A. Brataas, Y. V. Nazarov & G. E. W. Bauer. Finite-Element Theory of Transport in Ferromagnet–Normal Metal Systems. *Physical Review Letters* **84**, 2481–2484 (2000). URL.
- [31] L. J. Cornelissen, K. J. H. Peters, G. E. W. Bauer, R. A. Duine & B. J. van Wees. Magnon spin transport driven by the magnon chemical potential in a magnetic insulator. *Physical Review B* **94**, 014412 (2016). URL.
- [32] B. L. Giles, Z. Yang, J. S. Jamison & R. C. Myers. Long-range pure magnon spin diffusion observed in a nonlocal spin-Seebeck geometry. *Physical Review B* **92**, 224415 (2015). URL.
- [33] J. Shan, L. J. Cornelissen, N. Vlietstra, J. B. Youssef, T. Kuschel, R. A. Duine & B. J. van Wees. Influence of yttrium iron garnet thickness and heater opacity on the nonlocal transport of electrically and thermally excited magnons. *ArXiv e-prints* (2016). URL.
- [34] R. Schlitz. *Spin Transport Experiments in Hybrid Nanostructures.* Master’s thesis, Technische Universität München (2015).
- [35] N. Miura, I. Oguro & S. Chikazumi. Computer Simulation of Temperature and Field Dependences of Sublattice Magnetizations and Spin-Flip Transition in Gallium-Substituted Yttrium Iron Garnet. *Journal of the Physical Society of Japan* **45**, 1534–1541 (1978). URL.
- [36] G. F. Dionne. *Magnetic Oxides* (Springer US, 2009), first edn.
- [37] J. Bernasconi & D. Kuse. Canted Spin Phase in Gadolinium Iron Garnet. *Physical Review B* **3**, 811–815 (1971). URL.
- [38] A. E. Clark & E. Callen. Néel Ferrimagnets in Large Magnetic Fields. *Journal of Applied Physics* **39**, 5972–5982 (1968). URL.
- [39] S. Hoffman, K. Sato & Y. Tserkovnyak. Landau-Lifshitz theory of the longitudinal spin Seebeck effect. *Physical Review B* **88**, 064408 (2013). URL.
- [40] K.-i. Uchida, Z. Qiu, T. Kikkawa, R. Iguchi & E. Saitoh. Spin Hall magnetoresistance at high temperatures. *Applied Physics Letters* **106** (2015). URL.

- [41] S. Meyer, M. Althammer, S. Geprägs, M. Opel, R. Gross & S. T. B. Goennenwein. Temperature dependent spin transport properties of platinum inferred from spin Hall magnetoresistance measurements. *Applied Physics Letters* **104**, 242411 (2014). URL.
- [42] I. Diniz & A. T. Costa. Microscopic origin of subthermal magnons and the spin Seebeck effect. *New Journal of Physics* **18**, 052002 (2016). URL.
- [43] M. Weiler, M. Althammer, M. Schreier, J. Lotze, M. Pernpeintner, S. Meyer, H. Huebl, R. Gross, A. Kamra, J. Xiao, Y.-T. Chen, H. Jiao, G. E. W. Bauer & S. T. B. Goennenwein. Experimental Test of the Spin Mixing Interface Conductivity Concept. *Physical Review Letters* **111**, 176601 (2013). URL.
- [44] L. J. Cornelissen & B. J. van Wees. Magnetic field dependence of the magnon spin diffusion length in the magnetic insulator yttrium iron garnet. *Physical Review B* **93**, 020403 (2016). URL.
- [45] T. Kikkawa, K.-i. Uchida, S. Daimon, Z. Qiu, Y. Shiomi & E. Saitoh. Critical suppression of spin Seebeck effect by magnetic fields. *Physical Review B* **92**, 064413 (2015). URL.
- [46] S. A. Bender & Y. Tserkovnyak. Interfacial spin and heat transfer between metals and magnetic insulators. *Physical Review B* **91**, 140402 (2015). URL.
- [47] S. A. Bender, R. A. Duine & Y. Tserkovnyak. Electronic Pumping of Quasiequilibrium Bose-Einstein-Condensed Magnons. *Physical Review Letters* **108**, 246601 (2012). URL.
- [48] J. Barker & G. E. W. Bauer. Thermal spin dynamics of yttrium iron garnet. *ArXiv e-prints* (2016), 1607.03263. URL.
- [49] J. S. Plant. Spinwave dispersion curves for yttrium iron garnet. *Journal of Physics C: Solid State Physics* **10**, 4805 (1977). URL.
- [50] I. V. Kolokolov, V. S. L'vov & V. . Cherepanov. Magnon interaction and relaxation in yttrium iron garnet, a twenty-sublattice ferromagnet. *Soviet Physics - Journal of Experimental and Theoretical Physics* 1946–1960 (1984).
- [51] M. P. Ross. *Spin Dynamics in an Antiferromagnet*. Master's thesis, Technische Universität München (2013).
- [52] I. V. Kolokolov, V. S. L'vov & V. B. Cherepanov. Spin-wave spectra and thermodynamics of yttrium iron garnet-a twentysublattice ferrimagnet. *Journal of Experimental and Theoretical Physics* **84**, 1043–1058 (1983).
- [53] H. Jin, S. R. Boona, Z. Yang, R. C. Myers & J. P. Heremans. Effect of the magnon dispersion on the longitudinal spin Seebeck effect in yttrium iron garnets. *Physical Review B* **92**, 054436 (2015). URL.
- [54] J. Morkowski. The mean life-time of magnons in the itinerant electron model of ferromagnetism. *Physics Letters* **21**, 146 – 148 (1966). URL.

-
- [55] M. Schreier, G. E. W. Bauer, V. I. Vasyuchka, J. Flipse, K. ichi Uchida, J. Lotze, V. Lauer, A. V. Chumak, A. A. Serga, S. Daimon, T. Kikkawa, E. Saitoh, B. J. van Wees, B. Hillebrands, R. Gross & S. T. B. Goennenwein. Sign of inverse spin Hall voltages generated by ferromagnetic resonance and temperature gradients in yttrium iron garnet platinum bilayers. *Journal of Physics D: Applied Physics* **48**, 025001 (2015). URL.
- [56] L. J. Cornelissen & B. J. van Wees. Temperature dependence of the magnon spin diffusion length and magnon spin conductivity in the magnetic insulator yttrium iron garnet. *ArXiv e-prints* (2016). URL.
- [57] E.-J. Guo, J. Cramer, A. Kehlberger, C. A. Ferguson, D. A. MacLaren, G. Jakob & M. Kläui. Influence of Thickness and Interface on the Low-Temperature Enhancement of the Spin Seebeck Effect in YIG Films. *Physical Review X* **6**, 031012 (2016). URL.
- [58] U. Ritzmann, D. Hinzke & U. Nowak. Propagation of thermally induced magnonic spin currents. *Physical Review B* **89**, 024409 (2014). URL.
- [59] U. Ritzmann, D. Hinzke, A. Kehlberger, E.-J. Guo, M. Kläui & U. Nowak. Magnetic field control of the spin Seebeck effect. *Physical Review B* **92**, 174411 (2015). URL.
- [60] N. Roschewsky. *Spin Seebeck Effect Experiments*. Master's thesis, Technische Universität München (2014).
- [61] K. Ganzhorn, S. Klingler, T. Wimmer, S. Geprägs, R. Gross, H. Huebl & S. T. B. Goennenwein. Magnon-based logic in a multi-terminal YIG/Pt nanostructure. *Applied Physics Letters* **109** (2016). URL.
- [62] S. Klingler, P. Pirro, T. Brächer, B. Leven, B. Hillebrands & A. V. Chumak. Design of a spin-wave majority gate employing mode selection. *Applied Physics Letters* **105** (2014). URL.
- [63] A. R. Mellnik, J. S. Lee, A. Richardella, J. L. Grab, P. J. Mintun, M. H. Fischer, A. Vaezi, A. Manchon, E.-A. Kim, N. Samarth & D. C. Ralph. Spin-transfer torque generated by a topological insulator. *Nature* **511**, 449–451 (2014). URL.
- [64] J. Lotze, H. Huebl, R. Gross & S. T. B. Goennenwein. Spin Hall magnetoimpedance. *Physical Review B* **90**, 174419 (2014). URL.
- [65] A. V. Chumak, A. A. Serga & B. Hillebrands. Magnon transistor for all-magnon data processing. *Nature Communications* **5** (2014). URL.
- [66] K. Ganzhorn, J. Barker, R. Schlitz, M. Althammer, S. Geprägs, H. Huebl, B. A. Piot, R. Gross, G. E. W. Bauer & S. T. B. Goennenwein. Spin Hall Magnetoresistance in a Canted Ferrimagnet. *ArXiv e-prints* (2016). URL.
- [67] S. Geprägs, A. Kehlberger, F. D. Coletta, Z. Qiu, E.-J. Guo, T. Schulz, C. Mix, S. Meyer, A. Kamra, M. Althammer, H. Huebl, G. Jakob, Y. Ohnuma, H. Adachi, J. Barker, S. Maekawa, G. E. W. Bauer, E. Saitoh, R. Gross, S. T. B. Goennenwein & M. Kläui. Origin of the spin Seebeck effect in compensated ferrimagnets. *Nature Communications* **7**, – (2016). URL.

- [68] J. Barker. Atomistic Spin Dynamics of Ferromagnetic Insulators. Talk (2015).
- [69] M. Nagata, K. Tanabe, T. Moriyama, D. Chiba, J. I. Ohe, M. Myoka, T. Niizeki, H. Yanagihara, E. Kita & T. Ono. Ferromagnetic Resonance in Magnetite Thin Films. *IEEE Transactions on Magnetics* **50**, 1–3 (2014).
- [70] S. Mankovsky, D. Ködderitzsch, G. Woltersdorf & H. Ebert. First-principles calculation of the Gilbert damping parameter via the linear response formalism with application to magnetic transition metals and alloys. *Physical Review B* **87**, 014430 (2013). URL.
- [71] Y. Ohnuma, H. Adachi, E. Saitoh & S. Maekawa. Spin Seebeck effect in antiferromagnets and compensated ferrimagnets. *Physical Review B* **87**, 014423 (2013). URL.

Acknowledgements

There were many people during the past year who deserve great gratitude for the realization of this work. In particular I want to thank:

- Prof. Dr. Rudolf Gross for giving me the opportunity to accomplish my Master's degree at the Walther-Meissner-Institut (WMI).
- Prof. Dr. Sebastian T. B. Goennenwein for welcoming me to the Magnetiker group, pushing me to my limits, his eagerness on physics, leading me into the right direction for measurements, for very valuable discussions about my measurements and for proof-reading this thesis.
- Kathrin Ganzhorn for the brilliant supervision and her willingness to answer all my frequent questions, for introducing me to all the different measurement setups and fabrication procedures, for not being too serious on all the complicated and dead-serious physics we discussed about and for giving me tips and tricks to handle the great bosses of the Magnetiker group. Especially I want to thank her for the frequent visits of my office during the writing process, which ended up in highly valuable discussions about my deliberations for this work, drastically increasing the quality of this thesis. Moreover, I am very grateful for the pleasant atmosphere I felt during the whole year under her supervision.
- Dr. habil. Matthias Althammer for his large interest in my measurements and his frequent visits of my office, discussing my latest measurements, for his very intuitive and eager way of explaining complicated physics and his great readiness to help me with with all kinds of problems on physics.
- Dr. Sibylle Meyer for being my supervisor in the very beginning of my thesis, for introducing me to magnetotransport, measurement setups and showing me how to take care of the helium refilling of the cryostats.
- Dr. Stephan Gepraegs for helpful discussions about Gadolinium-Iron-Garnet and his mood-lifting character, that even remains when he's upset.
- Dr. habil. Hans-Gregor Huebl for introducing me to the possible Master topics at the WMI, spending much time for discussing my measurements and his motivating passion for physics.
- Dr. Mathias Weiler and Stefan Klingler for very helpful discussions about spin waves and improving my understanding of acoustic and optical magnon modes.
- Dr. Joseph Barker for his extremely helpful calculations of the YIG magnon spectrum and for critically discussing the model for the field dependence of the MMR in YIG|Pt.

- Hannes Maier-Flaig for inspiring ideas for future experiments, answering my frequent questions on the Gilbert damping and his helpful advice in the lab.
- All my Master colleagues, namely Hiroto Sakimura, Patrick Yard, Tuan Le Anh for creating a nice international atmosphere and having funny talks at lunch. Furthermore I'd like to thank my room-mates at the DPG conference: Hiroto Sakimura, Philip Louis and Daniel Schwienbacher for having a very fun time in Regensburg.
- M. Sc. Thomas Brenninger for his very kind character and for fixing the argon ion milling apparatus.
- Dr. Matthias Opel for all his help regarding computers and EDP-related stuff.
- The whole Magnetiker group for the nice atmosphere and their willingness to help me with whatever it was.
- Lena for being so unbelievably sympathetic throughout the stressful writing process of this thesis, baking self made cookies for me and being there even when I was hard to cope with.
- My friends, namely Daniel, Franz, Jakob, Jonas, Manuel and Simon, which haven't been helpful in a scientific way, but in a moral way, I guess, maybe.
- Finally, I want to thank my parents for giving me the opportunity to study here in Munich and for enabling me to live a fulfilled life.